Thesis

Fluctuation and dimensionality effects on superconductivity in the BCS–BEC crossover regime

Kyosuke Adachi

Department of Physics, Kyoto University

January, 2019

Abstract

The BCS-BEC crossover [1, 2, 3] is an exciting phenomenon in Fermionic many-body systems, which connects seemingly distinct two concepts: the condensation of weakly bound Fermion pairs described within the celebrated Bardeen-Cooper-Schrieffer (BCS) framework and the Bose-Einstein condensation (BEC) of tightly bound Fermion pairs. The BCS-BEC crossover has been investigated in ultracold atomic gases by virtue of the controllability of the attractive-interaction strength between atoms utilizing the Feshbach resonance [4]; on the other hand, the BCS framework has been applied to most superconductors since the attractive interaction between electrons is typically very weak.

Surprisingly, recent experiments [5, 6, 7] have suggested that FeSe and related materials may involve a strong attractive interaction between electrons, which can open up opportunities to explore physical properties, e.g., transport phenomena, magnetic-field effects, and crystal-lattice effects, specific to superconductors with strong attractive interaction. However, a theoretical understanding of such effects is still incomplete, and in this thesis we study magnetic-field and crystal-lattice-structure effects on superconductors with strong attractive interaction.

First, we investigate how thermodynamic quantities related to the superconducting fluctuation, which represents precursor phenomena of superconductivity, are influenced by a strong attractive interaction especially under magnetic field [8]. We find that the fluctuation-induced specific heat and diamagnetic susceptibility can be enhanced, and magnetization curves can show a characteristic behavior called crossing. These numerical results are qualitatively consistent with experimental results in FeSe.

Second, we explore features of the field-temperature (H-T) phase diagram of superconductors with strong attractive interaction [9]. We find that the vortex-lattice state, which involves a periodic array of quantized vortices and ubiquitously appears in type-II superconductors under magnetic field, can melt into the vortex-liquid state due to the enhanced superconducting fluctuation. Consequently, the vortex-liquid region, in addition to the preformed-pair region, can be enlarged in the H-T plane in systems with strong attractive interaction. We also point out the expected particle-density dependence of the H-T phase diagram.

Lastly, we study how dimensionality can manifest itself in superconductors with strong attractive interaction [10]. We find that the change in dimensionality from three-dimensional

to two-dimensional lattice structure can induce a crossover from the weak-coupling BCS side to the strong-coupling BEC side, or the BCS-BEC crossover, without tuning the interaction strength. We propose that inserting insulating layers or applying anisotropic pressure in layered superconductors can effectively change the dimensionality and thus can induce the BCS-BEC crossover.

Contents

Abstract **1**

List of publications **5**

1 Introduction: superconductivity in the BCS-BEC crossover regime **6**
1.1 BCS-BEC crossover 7
1.2 FeSe and related materials 15
1.3 Organization of this thesis 18

2 Effects of superconducting fluctuation on thermodynamic quantities **19**
2.1 Introduction to this chapter 19
2.2 Theoretical approach to superconducting fluctuation effects 20
2.3 Fluctuation-induced thermodynamic quantities 30
2.4 Discussion and summary 38

3 Features of field-temperature phase diagram **40**
3.1 Introduction to this chapter 40
3.2 Preliminary analysis of zero-field phase diagram 41
3.3 Theoretical approach to orbital magnetic-field effects 43
3.4 Field-temperature phase diagram 48
3.5 Discussion and summary 49
3.6 Derivations of some formulas 50

4 Effects of change in dimensionality **59**
4.1 Introduction to this chapter 59
4.2 Preliminary analysis of two-particle system 60
4.3 Dimensionality effects on phase diagram 62
4.4 Discussion and summary 66
4.5 Derivations of some formulas 67

5 Conclusion **71**

Bibliography **73**

Acknowledgment **80**

List of publications

Papers related to the thesis

1. Kyosuke Adachi and Ryusuke Ikeda,
   Enhanced superconducting fluctuation effects on thermodynamic properties in the BCS-BEC crossover regime,
   Phys. Rev. B **96**, 184507 (2017).

2. Kyosuke Adachi and Ryusuke Ikeda,
   Dimensionality-induced BCS-BEC crossover in layered superconductors,
   Phys. Rev. B **98**, 184502 (2018).

3. Kyosuke Adachi and Ryusuke Ikeda,
   Stabilization of vortex-liquid state by strong pairing interaction,
   arXiv:1811.07295 (submitted to Phys. Rev. B).

Published papers not included in the thesis

1. Kyosuke Adachi and Ryusuke Ikeda,
   Possible Field-Temperature Phase Diagrams of Two-Band Superconductors with Paramagnetic Pair-Breaking,
   J. Phys. Soc. Jpn. **84**, 064712 (2015).

2. Kyosuke Adachi and Ryusuke Ikeda,
   Fluctuation diamagnetism in two-band superconductors,
   Phys. Rev. B **93**, 134503 (2016).

Chapter 1

Introduction: superconductivity in the BCS-BEC crossover regime

Superconducting properties of most superconductors have been well described within the celebrated Bardeen-Cooper-Schrieffer (BCS) theory [11, 12]. This theory is based on a basic assumption that electrons interact with weak attractive interaction mediated by, e.g., lattice vibration.

In the field of ultracold atomic physics, it has been possible to artificially introduce a strong attractive interaction between laser-trapped Fermion gases with the use of the Feshbach resonance [4]. Accordingly, experimental and theoretical understanding of physical properties of Fermion gases with strong attractive interaction has been improved [13]. In particular, the so-called BCS-BEC crossover [1, 2, 3] (Sec. 1.1) is known to occur as the attractive interaction changes from weak to strong. For example, the vortex lattice of rotating superfluid Fermions has been observed in a broad range of interaction strength through the BCS-BEC crossover [14].

Regarding material realization of strong attractive interaction in superconductors, though it is still controversial whether a weak-coupling BCS picture is applicable to the high-temperature cuprate superconductors, observation of strong attractive interaction between electrons has been very rare. Surprisingly, recent experiments [5, 6] have suggested that there can be a strong attractive interaction between electrons in FeSe and related materials (Sec. 1.2). If this is the case, these superconductors can open up opportunities to explore physical properties, for example, transport phenomena, magnetic-field effects, and crystal-lattice effects, specific to superconductors involving strong attractive interaction. However, a theoretical understanding of such effects is still incomplete. Thus, we investigate the effects of external magnetic field and crystal lattice structure on superconductors with strong attractive interaction.

The BCS-BEC crossover in systems with an anisotropic, e.g., d-wave, pairing can be qualitatively different from that with the isotropic s-wave pairing. For example, the particle

density can be an important parameter in determining the macroscopic state in the case of the d-wave pairing [15], and thereby the BCS-BEC crossover may be induced by the change in the particle density [16]. Nevertheless, we concentrate on the simplest s-wave pairing in this thesis. As for FeSe, while two kinds of superconducting gaps have been observed, it is still controversial whether these gaps have nodes or not [5, 17, 18, 19, 20].

In the following, we explain basic concepts of the BCS-BEC crossover (Sec. 1.1) and experimental backgrounds of FeSe and related materials (Sec. 1.2). Throughout this thesis, we set $k_{\mathrm{B}} = \hbar = 1$ and adopt the international system of units.

1.1 BCS-BEC crossover

The BCS-BEC crossover [1, 2, 3] has been considered both theoretically and experimentally mainly in the field of ultracold atomic physics. In the following, we explain basic theoretical aspects of the BCS-BEC crossover.

For simplicity, let us consider a Fermion many-body system with attractive onsite (s-wave) interaction $-U < 0$ (see Ref. [21] for a review). The Hamiltonian is given as

$$H = \sum_{\boldsymbol{k},\sigma} \epsilon_{\boldsymbol{k}} c^{\dagger}_{\boldsymbol{k}\sigma} c_{\boldsymbol{k}\sigma} - \frac{U}{M} \sum_{\boldsymbol{k},\boldsymbol{k}',\boldsymbol{q}} c^{\dagger}_{\boldsymbol{q}/2+\boldsymbol{k}\uparrow} c^{\dagger}_{\boldsymbol{q}/2-\boldsymbol{k}\downarrow} c_{\boldsymbol{q}/2-\boldsymbol{k}'\downarrow} c_{\boldsymbol{q}/2+\boldsymbol{k}'\uparrow}. \tag{1.1.1}$$

Here, $c^{(\dagger)}_{\boldsymbol{k}\sigma}$ is the annihilation (creation) operator of an electron with wave number $\boldsymbol{k}$ and spin σ, and M is the total number of lattice sites. Specifically, we assume a three-dimensional simple cubic lattice so that $\epsilon_{\boldsymbol{k}} = -2t(\cos k_x + \cos k_y + \cos k_z)$ $(t > 0)$, but most of the discussions below do not depend on details of the lattice structure.

1.1.1 BCS-BEC crossover at zero temperature

Following the early work [22], we consider the ground state of the system described by Eq. (1.1.1). Our starting point is the BCS ground-state wave function:

$$|\psi_{\mathrm{BCS}}\rangle = \prod_{\boldsymbol{k}} \left(u_{\boldsymbol{k}} + v_{\boldsymbol{k}} \mathrm{e}^{\mathrm{i}\theta} c^{\dagger}_{\boldsymbol{k}\uparrow} c^{\dagger}_{-\boldsymbol{k}\downarrow} \right) |0\rangle \,. \tag{1.1.2}$$

Here, $|0\rangle$ is the vacuum state, and the variational parameters $u_{\boldsymbol{k}} \geq 0$ and $v_{\boldsymbol{k}} \geq 0$ satisfy ${u_{\boldsymbol{k}}}^2 + {v_{\boldsymbol{k}}}^2 = 1$ so that the normalization condition $\langle \psi_{\mathrm{BCS}} | \psi_{\mathrm{BCS}} \rangle = 1$ is satisfied. The phase θ represents the direction of the broken $U(1)$ symmetry, and we fix as

$$\theta = 0 \tag{1.1.3}$$

in the following.

We can show the quantum mechanical average of H with respect to $|\psi_{\rm BCS}\rangle$ is calculated (see, e.g., Ref. [12]) as

$$\langle\psi_{\rm BCS}|H|\psi_{\rm BCS}\rangle = 2\sum_{\boldsymbol{k}} \epsilon_{\boldsymbol{k}} {v_{\boldsymbol{k}}}^2 - \frac{U}{M}\left(\sum_{\boldsymbol{k}} u_{\boldsymbol{k}} v_{\boldsymbol{k}}\right)^2 - \frac{U}{M}\left(\sum_{\boldsymbol{k}} {v_{\boldsymbol{k}}}^2\right)^2. \tag{1.1.4}$$

On the other hand, the average of the total particle number $\widehat{N} = \sum_{\boldsymbol{k},\sigma} c^\dagger_{\boldsymbol{k}\sigma} c_{\boldsymbol{k}\sigma}$ is calculated as

$$\langle\psi_{\rm BCS}|\widehat{N}|\psi_{\rm BCS}\rangle = 2\sum_{\boldsymbol{k}} {v_{\boldsymbol{k}}}^2 \tag{1.1.5}$$

To determine the values of the variational parameters $u_{\boldsymbol{k}}$ and $v_{\boldsymbol{k}}$, we should minimize Eq. (1.1.1) with the average of the total particle number $\langle\psi_{\rm BCS}|\widehat{N}|\psi_{\rm BCS}\rangle$ fixed to a certain value N. Therefore, introducing a chemical potential μ, we should minimize $\langle\psi_{\rm BCS}|H|\psi_{\rm BCS}\rangle - \mu\langle\psi_{\rm BCS}|\widehat{N}|\psi_{\rm BCS}\rangle$ with respect to the variational parameters $\{v_{\boldsymbol{k}}\}$ (note that another parameter $u_{\boldsymbol{k}}$ can be written as $u_{\boldsymbol{k}} = \sqrt{1-{v_{\boldsymbol{k}}}^2}$) and also should solve $\langle\psi_{\rm BCS}|\widehat{N}|\psi_{\rm BCS}\rangle = N$ to determine the value of μ. To sum up, the following simultaneous equations should be solved for given N and U:

$$\frac{\partial}{\partial v_{\boldsymbol{k}}}\langle\psi_{\rm BCS}|(H-\mu\widehat{N})|\psi_{\rm BCS}\rangle = 0, \tag{1.1.6}$$

$$\langle\psi_{\rm BCS}|\widehat{N}|\psi_{\rm BCS}\rangle = N. \tag{1.1.7}$$

Transforming Eqs. (1.1.6) and (1.1.7), we finally obtain the following formulas for the variational paramters (see, e.g., Ref. [12]):

$$u_{\boldsymbol{k}} = \frac{1}{\sqrt{2}}\sqrt{1+\frac{\xi_{\boldsymbol{k}}}{E_{\boldsymbol{k}}}}, \tag{1.1.8}$$

$$v_{\boldsymbol{k}} = \frac{1}{\sqrt{2}}\sqrt{1-\frac{\xi_{\boldsymbol{k}}}{E_{\boldsymbol{k}}}}. \tag{1.1.9}$$

Here, $E_{\boldsymbol{k}}$ is the one-particle excitation energy in the superconducting state, or the excitation energy of one Bogoliubov quasi particle:

$$E_{\boldsymbol{k}} = \sqrt{{\xi_{\boldsymbol{k}}}^2 + \Delta^2}, \tag{1.1.10}$$

and $\Delta > 0$ (recall that the phase θ is fixed to 0 here) is the superconducting order parameter determined from the following equation:

$$\Delta = \frac{U}{M}\sum_{\boldsymbol{k}}\langle\psi_{\rm BCS}|c_{-\boldsymbol{k}\downarrow}c_{\boldsymbol{k}\uparrow}|\psi_{\rm BCS}\rangle = \frac{U}{M}\sum_{\boldsymbol{k}} u_{\boldsymbol{k}} v_{\boldsymbol{k}} = \frac{U}{M}\sum_{\boldsymbol{k}}\frac{\Delta}{2E_{\boldsymbol{k}}}. \tag{1.1.11}$$

The free-particle energy dispersion $\xi_{\boldsymbol{k}}$ is given as

$$\xi_{\boldsymbol{k}} = \epsilon_{\boldsymbol{k}} - \widetilde{\mu} = \epsilon_{\boldsymbol{k}} - \mu - \frac{UN}{2M}, \tag{1.1.12}$$

where $-UN/(2M)$ is the Hartree shift due to the attractive interaction, and $\widetilde{\mu} = \mu + UN/(2M)$ is the renormalized chemical potential [21, 23]. Equation (1.1.7) is reduced to

$$\sum_{\boldsymbol{k}} \left(1 - \frac{\xi_{\boldsymbol{k}}}{E_{\boldsymbol{k}}}\right) = N. \tag{1.1.13}$$

In the end, we should combine Eq. (1.1.11) with Eq. (1.1.13) to determine Δ and μ simultaneously. In the following, we show the behavior of Δ and μ in the weak-coupling ($U/W \ll 1$) and strong-coupling ($U/W \gg 1$) regime [W is the free-particle band width and $W = 12t$ in the system described by Eq. (1.1.1)].

In the weak-coupling regime ($U/W \ll 1$), based on Eq. (1.1.11) with an ansatz $\widetilde{\mu} \simeq E_{\mathrm{F}}$ (E_{F} is the Fermi energy of the corresponding free-particle system), smallness of U compared to W leads to the non-perturbative dependence of Δ on U:

$$\Delta \sim W \exp\left(-\frac{1}{N_{\mathrm{F}} U}\right), \tag{1.1.14}$$

where $N_{\mathrm{F}} \sim W^{-1}$ is the electronic density of states on the Fermi surface. On the other hand, from Eq. (1.1.13), we obtain

$$\widetilde{\mu} \simeq E_{\mathrm{F}}, \tag{1.1.15}$$

or with the use of $\widetilde{\mu} = \mu + UN/(2M)$,

$$\mu \simeq E_{\mathrm{F}} - \frac{UN}{2M} \tag{1.1.16}$$

which means, as expected above, that the chemical potential μ actually takes a value near E_{F} if the renormalization of the chemical potential from the Hartree shift is taken into account. The minimum energy E_{min} to break a Fermion pair (without changing the total particle number) is given by

$$E_{\mathrm{min}} = \min_{\boldsymbol{k}} 2\sqrt{{\xi_{\boldsymbol{k}}}^2 + \Delta^2} = 2\Delta. \tag{1.1.17}$$

These results [Eqs. (1.1.14) and (1.1.15)] are equivalent to those of the BCS theory [12]; thus, the weak-coupling regime ($U/W \ll 1$) is called the BCS regime [1]. In most superconductors, the attractive interaction between electrons is considered to be in the BCS regime, and thus the BCS theory is applicable without considering the equation to determine the chemical potential like Eq. (1.1.13).

In the strong-coupling regime ($U/W \gg 1$), Eqs. (1.1.11) and (1.1.13) lead to the following formulas [21, 23]:

$$\Delta \simeq \frac{U}{2}\sqrt{\frac{N}{M}\left(2 - \frac{N}{M}\right)}, \tag{1.1.18}$$

and

$$\widetilde{\mu} \simeq \frac{U}{2}\left(\frac{N}{M} - 1\right). \tag{1.1.19}$$

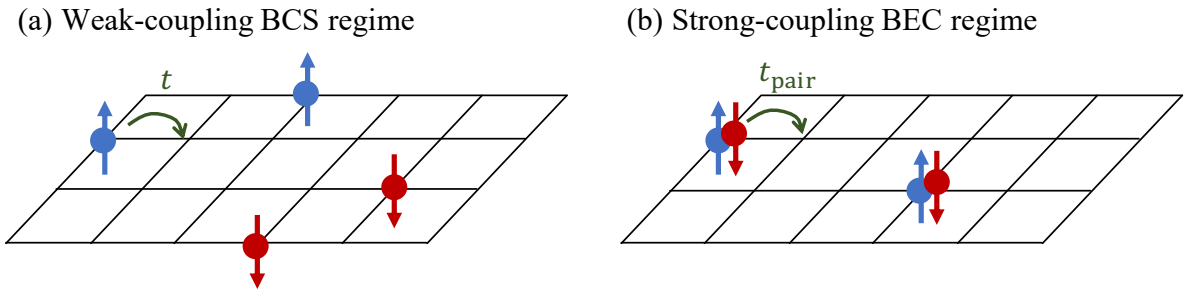

Figure 1.1: Schematic figure of typical normal states in the (a) BCS and (b) BEC regimes. (a) In the BCS regime, the normal state consists of unpaired Fermions with a hopping amplitude t. (b) In the BEC regime, the normal state (preformed-pair state) consists of paired Fermions with a pair hopping amplitude t_{pair}.

We note that we can easily derive these formulas if we first assume that $\Delta \gg W$ and $|\tilde{\mu}| \gg W$ as an ansatz. Recalling $\tilde{\mu} = \mu + UN/(2M)$, we can rewrite Eq. (1.1.19) as

$$\mu \simeq -\frac{U}{2}. \tag{1.1.20}$$

This suggests that we gain $-U$, which is the (minus) two-particle binding energy in the strong-coupling regime [21], if we put a Fermion pair in the considered system. Actually, the minimum energy E_{min} to break a Fermion pair (without changing the total particle number) is given by

$$E_{\mathrm{min}} = \min_{\boldsymbol{k}} 2\sqrt{{\xi_{\boldsymbol{k}}}^2 + \Delta^2} = 2\sqrt{\tilde{\mu}^2 + \Delta^2} = U. \tag{1.1.21}$$

In the strong-coupling regime, since particles basically exist as pairs with the binding energy U, we should just think of the ground-state Hilbert space as spanned by states where all the Fermions exist as pairs; therefore, by applying the second-order perturbation theory, we can obtain an effective nearest-neighbor hopping amplitude of pairs (Bosons) t_{pair} [see Fig. 1.1(b) for a schematic figure of typical normal states] as [21]

$$t_{\mathrm{pair}} = \frac{2t^2}{U}. \tag{1.1.22}$$

If the density is so low that we can neglect the interaction between pairs (Bosons), the system behaves as a free Boson system in a simple cubic lattice with the hopping amplitude t_{pair}, and thus the ground state is equivalent to the BEC state of pairs. Accordingly, the strong-coupling regime is called the BEC regime [1].

Interestingly, it is known that no phase transition occurs when the interaction strength is changed from the weak-coupling BCS regime to the strong-coupling BEC regime [21, 23]; therefore, the change from the BCS to BEC regime is called the BCS-BEC crossover. The

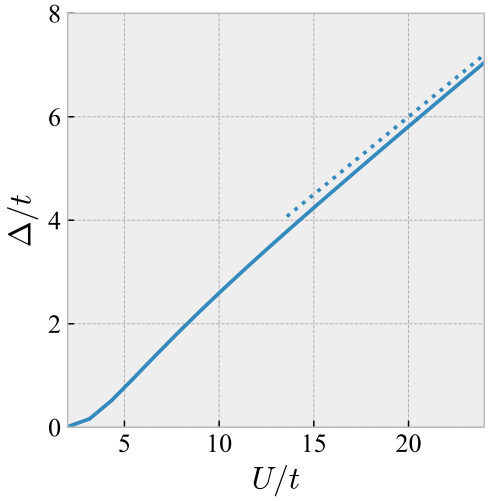

Figure 1.2: Order-parameter amplitude Δ as a function of the attractive interaction U with low density ($N/M = 0.2$). The asymptotic form in the BEC regime [Eq. (1.1.18)] is also shown (blue dotted line).

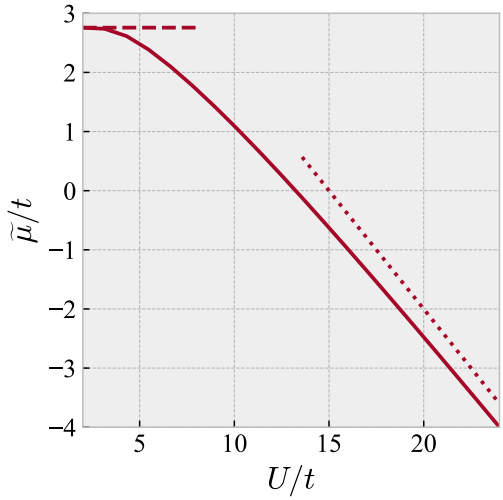

Figure 1.3: Renormalized chemical potential $\widetilde{\mu}$ as a function of the attractive interaction U (here $\widetilde{\mu}$ is measured from the free-particle band bottom) with low density ($N/M = 0.2$). The asymptotic forms in the BCS [Eq. (1.1.15), red dashed line] and BEC [Eq. (1.1.19), red dotted line] regimes are also shown.

numerically calculated U dependences of Δ and $\widetilde{\mu}$ (or μ) are shown in Figs. 1.2–1.5. In Figs. 1.2 and 1.3, we show the case with low density ($N/M = 0.2$). In Figs. 1.4 and 1.5, on the other hand, we show the case with high density near half filling ($N/M = 0.9$). We can make sure that no phase transition occurs through the drastic change in U. We note that the chemical potential is not so changed in the high-density case (Fig. 1.5) even if the interaction is strong. We also show the asymptotic behavior of Δ in the BEC regime and that of $\widetilde{\mu}$ in both the BCS and BEC regimes in these figures.

The above discussions are based on the BCS ground-state wave function [Eq. (1.1.2)], which is equivalent to the mean-field approximation [12]; thus, we neglect fluctuation effects. Theoretical calculations [24, 25] taking into account the quantum fluctuation effects within the Gaussian approximation around the mean-field solution has shown that fluctuations do not qualitatively change the U dependences of Δ and μ at zero temperature. On the other hand, as mentioned in the next subsection, fluctuation effects are important at finite temperature especially around the superconducting transition temperature T_{c}.

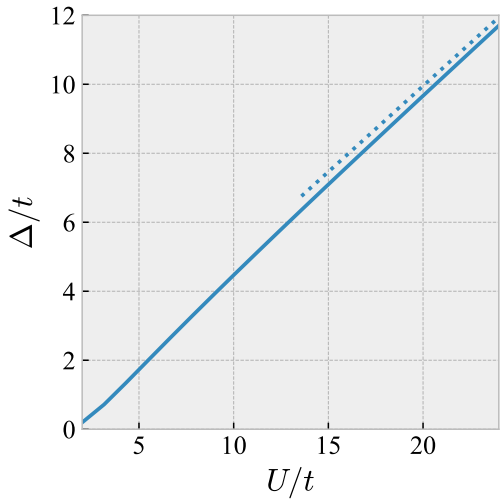

Figure 1.4: Order-parameter amplitude Δ as a function of the attractive interaction U with high density ($N/M = 0.9$). The asymptotic form is also shown in the same way as Fig. 1.2.

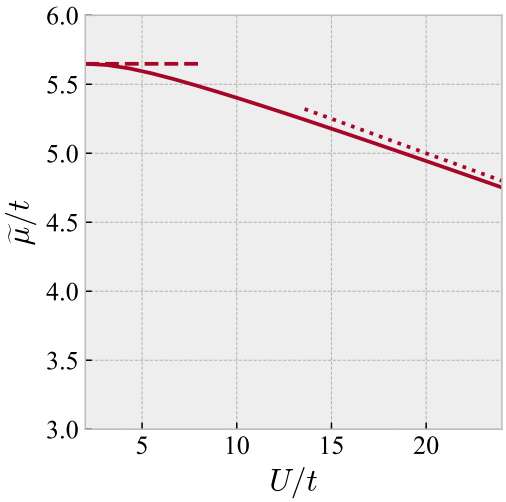

Figure 1.5: Renormalized chemical potential $\widetilde{\mu}$ as a function of the attractive interaction U (here $\widetilde{\mu}$ is measured from the free-particle band bottom) with high density ($N/M = 0.9$). The asymptotic forms are also shown in the same way as Fig. 1.3.

1.1.2 BCS-BEC crossover at finite temperature

In the following, let us consider physical properties of the sytstem described by Eq. (1.1.1) at finite temperatures [23]. Since we discuss similar problems especially in Chapters 3 and 4, we here concisely explain the way to theoretically obtain many-particle states at finite temperatures.

Cooling the system from high enough to zero temperature can cause a phase transition from the normal (metal) phase to the superconducting phase. We should notice that there are two kinds of phenomena which can occur when the temperature is decreased: the pair formation and the pair condensation. The latter is equivalent to the superconducting transition, and in general, these two phenomena can occur separately. The pair formation can be correctly described by the mean-field approximation [12]; on the other hand, the mean-field approximation, which neglects fluctuation effects, is in general not applicable to estimation of the pair condensation since the superconducting fluctuation affects the macroscopic pair condensation [23]. In this thesis, we write the pair-formation temperature as T^* and the pair-condensation temperature as T_c.

To estimate the pair-formation temperature T^*, neglecting fluctuation effects [26], we

obtain a free-particle number equation to determine the chemical potential μ:

$$N = 2\sum_{\boldsymbol{k}} \frac{1}{\mathrm{e}^{\xi_{\boldsymbol{k}}/T}+1}. \tag{1.1.23}$$

On the other hand, the equation to determine T^* for a given μ is the linearized gap equation (or the so-called Thouless criterion [27]):

$$\chi_{\boldsymbol{0}}^{(0)}(0) = \frac{1}{U}, \tag{1.1.24}$$

where

$$\chi_{\boldsymbol{q}}^{(0)}(\mathrm{i}\omega_m) = \frac{T}{M}\sum_{\boldsymbol{k},n} G_{\boldsymbol{k}+\boldsymbol{q}}^{(0)}(\mathrm{i}\varepsilon_n + \mathrm{i}\omega_m) G_{-\boldsymbol{k}}^{(0)}(-\mathrm{i}\varepsilon_n) \tag{1.1.25}$$

with the free-particle Green's function $G_{\boldsymbol{k}}^{(0)} = (\mathrm{i}\varepsilon_n - \xi_{\boldsymbol{k}})^{-1}$ and the Fermion (Boson) Matsubara frequency ε_n (ω_m). In the end, by solving Eqs. (1.1.23) and (1.1.24), we can estimate the pair-formation temperature T^*.

To calculate the pair-condensation temperature T_{c}, several approximations treating the fluctuation effects have been proposed [1]. Here we follow the method used in Ref. [23]. To consider the superconducting fluctuation, we take into account the ladder-like terms in the particle-particle channel as shown diagrammatically in Fig. 1.6. Collecting the same type of diagrams as shown in Fig. 1.6, we finally obtain the fluctuation thermodynamic potential Ω_{fluct} as follows:

$$\Omega_{\mathrm{fluct}} = T\sum_{\boldsymbol{q},m} \mathrm{e}^{+\mathrm{i}\omega_m 0} \ln\left[1 - U\chi_{\boldsymbol{q}}^{(0)}(\mathrm{i}\omega_m)\right]. \tag{1.1.26}$$

We note that Eq. (1.1.26) is nothing but the thermodynamic potential of free Bosons in the case where the Cooper-pair excitation (fluctuation) is identified with a Boson. Based on this fluctuation thermodynamic potential combined with the free-particle one Ω_0, we obtain as a number equation

$$N = \sum_{\boldsymbol{k}} \frac{1}{\mathrm{e}^{\xi_{\boldsymbol{k}}/T}+1} - \frac{\partial\Omega_{\mathrm{fluct}}}{\partial\mu}. \tag{1.1.27}$$

On the other hand, regarding the equation to determine the value of T_{c} for a given μ is the same as in the case of T^*; we use the linearized gap equation [Eq. (1.1.24)]. Therefore, we should solve Eqs. (1.1.27) and (1.1.24) to obtain the pair-condensation temperature T_{c}.

In the weak-coupling BCS regime ($U/W \ll 1$), the superconducting transition can be treated within the mean-field approximation since the fluctuation effects are weak and the second term in Eq. (1.1.27) can be neglected compared to the first term, so that the pair formation and the pair condensation (or superconducting transition) basically occur simultaneously [23], and thus

$$T^* \simeq T_{\mathrm{c}} \sim W\exp\left(-\frac{1}{N_{\mathrm{F}}U}\right). \tag{1.1.28}$$

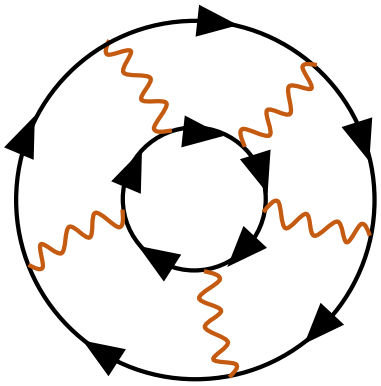

Figure 1.6: Diagrammatic representation of the contribution to the fluctuation thermodynamic potential $\Omega_{\rm fluct}$. The free-particle Green's function $G^{(0)}_{\boldsymbol{k}}(\mathrm{i}\varepsilon_n)$ (black oriented line) and the bare interaction $-U$ (brown wavy line) are shown.

This result is equivalent to that based on the usual BCS theory [12], in which the pair formation and condensation occur simultaneously.

In the strong-coupling BEC regime ($U/W \gg 1$), on the other hand, the fluctuation effects are vary strong and the second term in Eq. (1.1.27) actually becomes dominant. Neglecting the first term in Eq. (1.1.27), we can show that the pair-condensation temperature $T_{\rm c}$ satisfies the following relation:

$$T_{\rm c} \propto t^2/U. \tag{1.1.29}$$

Since in the BEC regime the pair hopping amplitude is given by $t_{\rm pair} = 2t^2/U$ [Eq.(1.1.22)] as discussed in Sec. 1.1.1 and the BEC transition temperature has the same energy scale as a typical kinetic energy $t_{\rm pair}$, Eq. (1.1.29) means that the pair condensation (or superconducting transition) can be described as the BEC transition of tightly bound pairs [21]. We note that the U dependence of $T_{\rm c}$ in the BEC regime in our lattice system is different from that in continuum systems such as ultracold atomic gases; in such continuum systems, $T_{\rm c}$ does not depend on U in the BEC regime because a typical kinetic energy of pairs $n^{2/3}/(4m)$ (m is the mass of a Fermion and n is the density of Bosons) do not depend on the value of U [3, 21]. Regarding the pair-formation temperature T^* in the BEC regime, we can show that T^* is proportional to the binding energy $E_{\rm b} \simeq U$ as expected. Thus, we obtain

$$T^* \propto U. \tag{1.1.30}$$

Comparing Eq. (1.1.29) with Eq. (1.1.30), we can see the separation between T^* and $T_{\rm c}$ become larger as the interaction strength becomes stronger. We note that also in gas systems, $T_{\rm c} \sim$ const. while $T^* \propto U$ so that the separation between them occurs. The pairs emerging between T^* and $T_{\rm c}$ are called the preformed pairs since they are not condensed but formed.

Between T^* and T_c, the pseudogap is theoretically expected to appear [1, 28] because it should cost finite energy to break a preformed pair into two independent Fermions.

Regarding the interaction-temperature (U-T) phase diagram beyond the BCS or BEC regime, we show some calculated results in the following chapters (see Figs. 2.3 and 3.1). At finite temperatures, in a similar way to the BCS-BEC crossover in the ground state (Sec. 1.1.1), it has been known that no phase transition occurs when the interaction is changed from the weak-coupling BCS regime to the strong-coupling BEC regime as long as the normal-superconducting transition does not occur. Therefore, the concept of the BCS-BEC crossover is naturally extended to finite temperatures.

Apart from the approach in Ref. [23] (see also Chapter 2), several approximations have been proposed to consider the fluctuation effects and calculate T_c in both lattice and continuum Fermion systems in the BCS-BEC crossover regime, including the (bare) T-matrix approximation [1, 28, 29, 30] (see Chapters 3 and 4), the self-consistent T-matrix approximation [1, 30, 31, 32], and variant T-matrix approximations [1, 29, 33, 34, 35, 36, 37]. Also, more quantitative quantum Monte Carlo calculations [38, 39, 40] have been performed. To know qualitative features of phase diagrams and thermodynamic properties, the approach in Ref. [23] or the simplest (bare) T-matrix approximation seems to be applicable through the BCS-BEC crossover [1, 3] (note that there are some exceptions [36]). In this thesis, therefore, the approach in Ref. [23] (Chapter 2) and the (bare) T-matrix approximation (Chapters 3 and 4) are applied to investigation of thermodynamic quantities and qualitative features of phase diagrams.

1.2 FeSe and related materials

In this section, we explain experimental backgrounds of iron selenide (FeSe), one of the iron-based superconductors. Though recent studies have proposed exotic properties of FeSe thin films such as high-temperature superconductivity [41, 42, 43, 44, 45, 46, 47, 48] and emergence of magnetic [49] or charge [50] orders, we here focus only on interesting bulk properties of FeSe.

1.2.1 Basic properties of FeSe

FeSe is one of the iron-based superconductors and was discovered in 2008 [51]. It has a layered structure consisting of Fe-Se layers. The lattice structure is tetragonal at a temperature higher than the structural transition temperature $T_{\rm str} \sim 90$K [51] and orthorhombic at a temperature lower than $T_{\rm str}$. Superconductivity appears when a temperature is lower than the superconducting transition temperature $T_c \sim 9$K [51]. Based on resistivity data [5, 52], the coherence lengths are estimated to be $\xi_{ab} \sim 5.7$nm in the ab plane and $\xi_c \sim 1.3$nm in the c axis. Comparing these coherence lengths with the a-axis length $a = 3.78$Å and c-axis length

$c = 5.52$Å [53], both $\xi_{ab} > a$ and $\xi_c > c$ are satisfied, so that superconductivity appearing in FeSe is expected to have anisotropic three-dimensional nature.

The electronic band structure near the Fermi surface has been observed in the Shubnikov–de Haas oscillation measurement [52], the quasi-particle interference based on spectroscopic-imaging scanning tunneling microscopy [5], and the angle-resolved photoemission spectroscopy (ARPES) [54, 55, 56, 57]. According to these results, the band structure near the Fermi surface consists of quasi-two-dimensional electron and hole bands. We stress that superconductivity in this material is (anisotropic) three dimensional in nature as mentioned above, while the electronic band structure is (quasi) two dimensional.

The origin of structural and superconducting transitions and the relation between them have been intensively discussed including other iron-based superconductors [58, 59, 60]. The structural transition is considered to be driven by the so-called electronic nematic order [61], in which the difference between the occupation number of the iron d_{xz} orbital and that of the iron d_{yz} orbital becomes non-vanishing ($n_{xz} \neq n_{yz}$), due to strong electron correlation. Since the electronic nematic order is reflected in the energy spectrum, the angle-dependent splitting of the excitation energy appears, e.g., in the ARPES measurments [54, 55, 56, 57]. Regarding the origin of the nematicity, the spin-nematic order [61] and the orbital order [62] have been proposed. Though the origin of superconductivity and resulting superconducting symmetry are still controversial, several novel mechanisms such as orbital-fluctuation mediated superconductivity [63] have been theoretically suggested.

1.2.2 Possible realization of BCS-BEC crossover regime in FeSe

Apart from the microscopic origin of nematicity or superconductivity, several interesting properties have been observed in FeSe. Three kinds of unique features of FeSe are mainly explained in the remaining part of this subsection: a large ratio of the superconducting transition temperature $T_{\rm c}$ to the Fermi energy $E_{\rm F}$, possible emergence of the pseudogap in the one-particle spectrum or the electronic density of states, and strong superconducting fluctuation effects especially under magnetic fields.

According to the quantum-oscillation measurement [52] and spectroscopic-imaging scanning tunneling microscopy [5], the ratio of the superconducting transition temperature $T_{\rm c}$ to the Fermi energy $E_{\rm F}$ measured from the band bottom is very large. Specifically [5],

$$\begin{cases} T_{\rm c}/E_{\rm F} \sim 0.3 & \text{(for electron band)} \\ T_{\rm c}/E_{\rm F} \sim 0.08 & \text{(for hole band)} \end{cases} . \tag{1.2.1}$$

Recalling that the ratio $T_{\rm c}/E_{\rm F}$ is much smaller than unity in the weak-coupling BCS regime (Sec. 1.1), we can guess that FeSe may involve strong attractive interaction and that FeSe may be a superconductor in the BCS-BEC crossover regime [5]. Also, the superconducting

gap Δ in each band has a large value in units of the Fermi energy [5]:

$$\begin{cases} \Delta/E_{\rm F} \sim 1 & \text{(for electron band)} \\ \Delta/E_{\rm F} \sim 0.3 & \text{(for hole band)} \end{cases}, \tag{1.2.2}$$

which is qualitatively consistent with the speculation that FeSe involves strong attractive interaction.

As mentioned in Sec. 1.1, emergence of the pseudogap in the one-particle spectrum is considered to be one of the characteristic features of a Fermion system in the BCS-BEC crossover regime. Actually, recent NMR measurements in FeSe have suggested the emergence of the pseudogap [6, 64]. Based on the suppression of the nuclear spin-lattice relaxation rate divided by the temperature $(T_1T)^{-1}$ below characteristic temperatures T^*, emergence of the pseudogap below T^* has been suggested in Refs. [6, 64]. According to Ref. [64], $T^* \sim 15{\rm K} \sim 1.7\,T_{\rm c}$. Moreover, it has also been observed that $T^*(H)$ decreases as a function of the magnetic-field strength H in a similar way to the superconducting transition temperature $T_{\rm c}(H)$ [64]; this observation strongly suggests that the origin of the pseudogap is related to superconducting phenomena and thus that the pseudogap is induced by preformed pairs created by a strong attractive interaction between electrons. We note that the pseudogap has not been observed in FeSe with other measurements for the one-particle spectrum such as the scanning tunneling spectroscopy.

Strong superconducting fluctuation effects have been observed in magnetic-torque and magnetization measurements [6]. First, according to the magnetic-torque measurements, the diamagnetic susceptibility $\chi_{\rm dia}(T)$ is enhanced. In the weak-coupling BCS regime with weak fluctuation effects, it is known that the Gaussian approximation [65] is applicable in a broad temperature range and that we obtain the following formula for anisotropic superconductors:

$$\chi_{\rm dia}^{\rm (Gauss)}(T) = -\frac{\pi\mu_0}{6{\phi_0}^2}\frac{{\xi_{ab}}^2 T_{\rm c}}{\xi_c\sqrt{T/T_{\rm c}-1}}. \tag{1.2.3}$$

Here, several symbols are used: the vacuum permeability μ_0, the flux quantum $\phi_0 = \pi/e$ with the elementary charge e, the coherence lengths ξ_{ab} in the ab plane and ξ_c in the c axis. In the above-mentioned magnetic-torque measurements, $\chi_{\rm dia}(T)$ has been estimated to be ten times larger or more than $\chi_{\rm dia}^{\rm (Gauss)}(T)$ [6]. Since the enhancement of fluctuation effects in the BCS-BEC crossover regime is naturally expected [66], such a large enhancement of $\chi_{\rm dia}(T)$ indirectly indicates that FeSe is in the BCS-BEC crossover regime. Second, the temperature range where the fluctuation diamagnetism is observed is much broader than in conventional materials; actually, in FeSe, the fluctuation diamagnetism has been observed for $T_{\rm c} < T < T_{\rm onset}$ with $T_{\rm onset} \sim 20{\rm K} \gtrsim 2T_{\rm c}$ [6]. This also suggests that superconducting fluctuation effects in FeSe are strong and that FeSe can be in the BCS-BEC crossover regime. Third, the magnetization curves show the so-called crossing behavior [6, 67], which has been also observed in quasi-two-dimensional cuprate superconductors [68]. Since this crossing

behavior has been considered to appear in quasi-two-dimensional superconductors with strong fluctuation effects [68, 69], it should be clarified how we can understand the crossing behavior appearing in FeSe, in which superconductivity has anisotropic three-dimensional nature as mentioned above. We note that the in-field specific heat in FeSe shows a broad change around $H_{c2}(T)$ [19], which is consistent with the strong fluctuation effects; on the other hand, the zero-field one shows a relatively sharp jump at T_c [17, 18, 19], which seemingly contradicts the strong fluctuation nature, so that the consistency should be resolved in the future.

Regarding other materials, doped FeSe such as $Fe(Se_{1-x}S_x)$ [70] and $Fe(Se_{1-x}Te_x)$ [7] have been considered to be candidates for superconductors in the BCS-BEC crossover regime. In particular, Ref. [7] proposes that the BCS-BEC crossover can be induced by doping Te in FeSe.

1.3 Organization of this thesis

In this thesis, we investigate physical properties of superconductivity in the BCS-BEC crossover regime, focusing on effects of fluctuation and dimensionality. In Chapter 2, fluctuation-induced thermodynamic properties such as the specific heat and magnetization are explored. Qualitative difference is elucidated between fluctuation effects on thermodynamics in the BCS regime and those in the BCS-BEC crossover regime. In Chapter 3, we investigate typical features of the field-temperature (H-T) phase diagram in the BCS-BEC crossover regime. Comparing the H-T phase diagram in the BCS-BEC crossover regime with that in the conventional BCS regime, we clarify what is specific to the BCS-BEC crossover regime. In Chapter 4, we study effects of the change in dimensionality on superconductivity with strong pairing interaction.

Chapter 2

Effects of superconducting fluctuation on thermodynamic quantities

2.1 Introduction to this chapter

As shown in Sec. 1.2.2, several unique electronic properties have been observed in FeSe, one of the iron-based superconductors. In particular, the Fermi energy of FeSe may be comparable in magnitude to the superconducting gap [5, 52] suggesting the intriguing possibility that electrons in FeSe effectively interact with a much stronger attractive interaction than those in conventional superconductors; in other words, electrons in FeSe can be in the BCS-BEC crossover regime [3]. In the following, we consider superconducting fluctuation (SCF) effects in FeSe, which is our main focus in this chapter.

As mentioned in Chapter 1.2.2, in FeSe, thermodynamic effects of SCF near the superconducting transition temperaure $T_{\rm c}$ are characteristic. The observed SCF-induced diamagnetic susceptibility in low magnetic fields is anomalously large compared to the theoretically predicted value within the Gaussian approximation [Eq. (1.2.3)]. Also the temperature-dependent magnetization curves in high magnetic fields show a crossing behavior [6]. This crossing behavior has been observed mainly in strongly two-dimensional (2D) systems such as the BSCCO compounds of the high-$T_{\rm c}$ cuprates [68] and has been theoretically supported in a 2D model [71]. In contrast, FeSe seems to be three dimensional (3D) judging from the fact that the size of the coherence length ξ_c ($\sim$ 1.3nm [52]) along the c-axis is longer than $s/\sqrt{2}$, where s ($\sim$ 0.55nm [5]) is the interlayer spacing or the c-axis length. Hence the crossing behavior of the magnetization curves observed in FeSe [6] is an unexpected event.

Typically, compared to the BCS regime, $T_{\rm c}$ and the coherence length are high and short in the BCS-BEC crossover regime, respectively [3]; thus the critical region, in which fluctuation interection is important, is enlarged [66]. Accordingly, it is natural that the SCF should be enhanced when the system enters the BCS-BEC crossover regime. However, it is non-trivial whether the SCF in the BCS-BEC crossover regime influences thermodynamics in the

same manner as that in the BCS regime. Further, it is an important subject to theoretically investigate whether the idea that FeSe is in the BCS-BEC crossover regime can explain the observed strange thermodynamic behaviors such as the enhanced SCF effect on the diamagnetic response.

On the basis of these backgrounds, we consider SCF effects on thermodynamics of electron systems in the BCS-BEC crossover regime under magnetic fields and elucidate several features which are substantially different from those in the BCS regime. In the context of the ultracold atomic gases, the fluctuation effects in the neutral superfluid systems in the BCS-BEC crossover regime have been studied so far [72]. To the best of our knowledge, however, the corresponding subject in superconductors under a magnetic field, and equivalently, the thermal fluctuation effect in the neutral Fermi superfluid under rotation, i.e., the situation where the vortices are induced by the field, has never been studied in the crossover regime.

This chapter is organized as follows. In Sec. 2.2, we explain our starting model Hamiltonian and our approach to estimate the SCF-induced specific heat and magnetization. In Sec. 2.3, we present the obtained results on thermodynamic quantities in addition to some preliminary results on the critical temperature and coherence length. In Sec. 2.4, we discuss relevance of our results to the anomalous SCF-induced phenomena observed in FeSe under magnetic fields and add some remarks. Finally in Sec. 2.4, we state our conclusion of this chapter.

2.2 Theoretical approach to superconducting fluctuation effects

2.2.1 Model

To consider the SCF-induced thermodynamic quantities such as the specific heat and the diamagnetic response, we start with a simple Hamiltonian of an isotropic 3D system with a separable attractive interaction:

$$\begin{aligned} H &= H_0 + H_{\rm int} \\ &= \sum_{\boldsymbol{k},\sigma} \frac{k^2}{2m} c^\dagger_{\boldsymbol{k}\sigma} c_{\boldsymbol{k}\sigma} - \frac{U}{V} \sum_{\boldsymbol{q},\boldsymbol{k},\boldsymbol{k}'} \varphi_k \varphi_{k'} c^\dagger_{\boldsymbol{q}/2+\boldsymbol{k}\uparrow} c^\dagger_{\boldsymbol{q}/2-\boldsymbol{k}\downarrow} c_{\boldsymbol{q}/2-\boldsymbol{k}'\downarrow} c_{\boldsymbol{q}/2+\boldsymbol{k}'\uparrow}. \end{aligned} \tag{2.2.1}$$

Here, m is the mass of particles, $U(>0)$ is the attractive interaction strength, V $(= L_x L_y L_z)$ is the total volume of the system, and $c^{(\dagger)}_{\boldsymbol{k}\sigma}$ is the annihilation (creation) operator of a particle with spin σ and momentum $\boldsymbol{k}$. The interaction form factor φ_k is introduced as ${\varphi_k}^2$ has the Lorentzian form [23]

$$\varphi_k = \frac{1}{\sqrt{1 + (k/k_0)^2}}, \tag{2.2.2}$$

where k_0 is an effective momentum cutoff, or ${k_0}^{-1}$ represents the width of the interaction in the real space.

We assume a system with the total number (density) of particles fixed to $N_{\rm tot}$ ($n_{\rm tot} = N_{\rm tot}/V$) and consider a grand-canonical ensemble specified by the temperature T ($= \beta^{-1}$) and the chemical potential μ. Effects of an applied magnetic field is taken into account afterwards (see Sec. 2.2.3). In a two-particle system described with Eq. (2.2.1), a two-particle bound state can appear [29] when U is strong enough to exceed a threshold value U_0 given as

$$U_0 = \frac{4\pi}{mk_0}. \tag{2.2.3}$$

Thus we expect that a many-body system described with Eq. (2.2.1) will be in the BCS-BEC crossover regime when U is close to U_0.

Though the model described with Eq. (2.2.1) is clearly too simple to describe the electron states in FeSe, we believe that we can sufficiently study with this model the generic nature of the SCF effects on thermodynamics in the BCS-BEC crossover regime.

2.2.2 Shift of chemical potential

In the BCS-BEC crossover regime, as explained in Sec. 1.1, a strong attractive interaction causes a decrease in the chemical potential from the Fermi energy defined as $(3\pi^2 n_{\rm tot})^{2/3}/(2m)$ ($= E_{\rm F}$). To determine the chemical potential, we calculate the thermodynamic potential in zero field following the standard approach developed by Nozières and Schmitt-Rink [23]. First, the thermodynamic potential Ω is calculated within the ladder approximation (see Fig. 1.6), which is equivalent to the Gaussian approximation in the functional-integral representation [26], as

$$\Omega = \Omega_0 + T\sum_{\boldsymbol{q},m} {\rm e}^{+{\rm i}\omega_m 0} \ln\left[1 - U\chi^{(0)}_{\boldsymbol{q}}({\rm i}\omega_m)\right], \tag{2.2.4}$$

where Ω_0 [$= -T \ln {\rm Tr}\, \exp(-\beta H_0 + \beta\mu N_{\rm tot})$] is the contribution from the kinetic energy of the electrons, ω_m ($= 2\pi m T$) ($m = 0, \pm 1, \pm 2, \cdots$) is the Bosonic Matsubara frequency. In addition, $\chi^{(0)}_{\boldsymbol{q}}({\rm i}\omega_m)$ is defined as

$$\begin{aligned}
\chi^{(0)}_{\boldsymbol{q}}({\rm i}\omega_m) &= \frac{T}{V}\sum_{\boldsymbol{k},n} {\varphi_k}^2 G^{(0)}_{\boldsymbol{q}/2+\boldsymbol{k}\uparrow}({\rm i}\varepsilon_n + {\rm i}\omega_m) G^{(0)}_{\boldsymbol{q}/2-\boldsymbol{k}\downarrow}(-{\rm i}\varepsilon_n) \\
&= \frac{1}{2V}\sum_{\boldsymbol{k}} {\varphi_k}^2 \frac{\tanh(\beta\xi_{\boldsymbol{q}/2+\boldsymbol{k}}/2) + \tanh(\beta\xi_{\boldsymbol{q}/2-\boldsymbol{k}}/2)}{\xi_{\boldsymbol{q}/2+\boldsymbol{k}} + \xi_{\boldsymbol{q}/2-\boldsymbol{k}} - {\rm i}\omega_m},
\end{aligned} \tag{2.2.5}$$

where $\xi_{\boldsymbol{k}} = \xi_k = k^2/(2m) - \mu$, and $G^{(0)}_{\boldsymbol{k}\sigma}({\rm i}\varepsilon_n)$ is the free-particle Green's function defined as

$$G^{(0)}_{\boldsymbol{k}\sigma}({\rm i}\varepsilon_n) = \frac{1}{\xi_{\boldsymbol{k}} - {\rm i}\varepsilon_n}. \tag{2.2.6}$$

Here $\varepsilon_n = 2\pi(n+1/2)T$ $(n = 0, \pm 1, \pm 2, \cdots)$ is the Fermionic Matsubara frequency. Next, by differentiating Ω with respect to μ, we get the total number density:

$$\begin{aligned} n_{\rm tot} &= -\frac{1}{V}\frac{\partial \Omega}{\partial \mu} \\ &= \frac{1}{V}\sum_{\boldsymbol{k},\sigma}\frac{1}{{\rm e}^{\beta\xi_{\boldsymbol{k}}}+1} + \frac{T}{V}\sum_{\boldsymbol{q},m}{\rm e}^{+{\rm i}\omega_m 0}\frac{U\partial_\mu \chi_{\boldsymbol{q}}^{(0)}({\rm i}\omega_m)}{1-U\chi_{\boldsymbol{q}}^{(0)}({\rm i}\omega_m)}. \end{aligned} \tag{2.2.7}$$

Further, in the Gaussian approximation, the superconducting critical temperature $T_{\rm c}$ is determined by

$$1 - U\chi_{\boldsymbol{0}}^{(0)}(0) = 0. \tag{2.2.8}$$

From Eqs. (2.2.7) and (2.2.8), we obtain both $T_{\rm c}$ and $\mu(T = T_{\rm c})$ for a fixed $n_{\rm tot}$.

2.2.3 GL action describing zero-field SCF

In the following, we derive the Ginzburg-Landau (GL) action to describe the SCF effects on thermodynamics near $T_{\rm c}$. First, we rewrite the grand-canonical partition function Z in the functional-integral form [26]:

$$Z = {\rm Tr}\,{\rm e}^{-\beta H+\beta\mu N_{\rm tot}} = \int\left(\prod_{\boldsymbol{k},\sigma,n}{\rm d}\overline{c}_{\boldsymbol{k}\sigma n}{\rm d}c_{\boldsymbol{k}\sigma n}\right){\rm e}^{-\mathcal{S}}, \tag{2.2.9}$$

where the action $\mathcal{S}$ is defined as

$$\begin{aligned} \mathcal{S} &= \mathcal{S}_0 + \mathcal{S}_{\rm int} \\ &= \beta\left[\sum_{\boldsymbol{k},\sigma,n}(-{\rm i}\varepsilon_n + \xi_{\boldsymbol{k}})\,\overline{c}_{\boldsymbol{k}\sigma n}c_{\boldsymbol{k}\sigma n} - \frac{U}{V}\sum_{\boldsymbol{q},m}\overline{P}_{\boldsymbol{q}m}P_{\boldsymbol{q}m}\right]. \end{aligned} \tag{2.2.10}$$

Here, the dimensionless Fermionic fields $\{c_{\boldsymbol{k}\sigma n}, \overline{c}_{\boldsymbol{k}\sigma n}\}$ are the Grassmann numbers, and

$$\begin{cases} P_{\boldsymbol{q}m} = \sum_{\boldsymbol{k},n}\varphi_k c_{\boldsymbol{q}/2-\boldsymbol{k}\downarrow -n-1}c_{\boldsymbol{q}/2+\boldsymbol{k}\uparrow n+m} \\ \overline{P}_{\boldsymbol{q}m} = \sum_{\boldsymbol{k},n}\varphi_k \overline{c}_{\boldsymbol{q}/2+\boldsymbol{k}\uparrow n+m}\overline{c}_{\boldsymbol{q}/2-\boldsymbol{k}\downarrow -n-1} \end{cases} \tag{2.2.11}$$

Next, we use the Hubbard-Stratonovich transformation [26] to discuss fluctuation effects of the superconducting order-parameter fields. By introducing the dimensionless Bosonic order-parameter fields $\{a_{\boldsymbol{q}m}, \overline{a}_{\boldsymbol{q}m}\}$ corresponding to the superconducting order-parameter fields, we rewrite the interaction part of the action $\mathcal{S}_{\rm int}$ as

$${\rm e}^{-\mathcal{S}_{\rm int}} = \int\left(\prod_{\boldsymbol{q},m}\frac{{\rm d}\overline{a}_{\boldsymbol{q}m}{\rm d}a_{\boldsymbol{q}m}}{\pi}\right){\rm e}^{-\sum_{\boldsymbol{q},m}\overline{a}_{\boldsymbol{q}m}a_{\boldsymbol{q}m}}{\rm e}^{\sqrt{\beta U/V}\sum_{\boldsymbol{q},m}(\overline{a}_{\boldsymbol{q}m}P_{\boldsymbol{q}m}+a_{\boldsymbol{q}m}\overline{P}_{\boldsymbol{q}m})}. \tag{2.2.12}$$

Then, by integrating with respect to $\{c_{\boldsymbol{k}\sigma n}, \overline{c}_{\boldsymbol{k}\sigma n}\}$, we obtain

$$Z = Z_0 Z_{\rm eff}, \tag{2.2.13}$$

where Z_0 $(= e^{-\beta\Omega_0})$ is the non-interacting part of Z, and

$$Z_{\rm eff} = \int \left(\prod_{\boldsymbol{q},m} \frac{{\rm d}\overline{a}_{\boldsymbol{q}m} {\rm d}a_{\boldsymbol{q}m}}{\pi} \right) {\rm e}^{-\mathcal{S}_{\rm eff}}. \tag{2.2.14}$$

Here, $\mathcal{S}_{\rm eff}$ is the effective action describing the SCF, formally expressed as

$${\rm e}^{-\mathcal{S}_{\rm eff}} = {\rm e}^{-\sum_{\boldsymbol{q},m} \overline{a}_{\boldsymbol{q}m} a_{\boldsymbol{q}m}} \langle {\rm e}^{\sqrt{\beta U/V} \sum_{\boldsymbol{q},m} (\overline{a}_{\boldsymbol{q}m} P_{\boldsymbol{q}m} + a_{\boldsymbol{q}m} \overline{P}_{\boldsymbol{q}m})} \rangle_0, \tag{2.2.15}$$

where $\langle \cdots \rangle_0$ denotes the grand-canonical average with respect to the non-interacting part $\mathcal{S}_0$.

We note that we can reproduce Eqs. (2.2.7) and (2.2.8) by expanding $\mathcal{S}_{\rm eff}$ up to the second order in $\{a_{\boldsymbol{q}m}, \overline{a}_{\boldsymbol{q}m}\}$, i.e., using the Gaussian approximation. However, since the critical region is strongly enhanced in the BCS-BEC crossover regime [66], we need to go beyond the Gaussian approximation, i.e., the mode coupling between the SCFs has to be incorporated to consider the critical behavior.

To treat the mode coupling between the SCFs, or the order-parameter fields , we expand $\mathcal{S}_{\rm eff}$ up to the fourth order in $\{a_{\boldsymbol{q}m}, \overline{a}_{\boldsymbol{q}m}\}$. In addition, we neglect the quantum fluctuation (i.e., $a_{\boldsymbol{q}m}$ and $\overline{a}_{\boldsymbol{q}m}$ with $m \neq 0$) and use the gradient expansion, which is valid at least when we describe the long-wavelength and low-energy SCF. This results in replacing $\mathcal{S}_{\rm eff}$ in Eq. (2.2.14) with the GL action $\mathcal{S}_{\rm GL}$:

$$\mathcal{S}_{\rm GL} = \int {\rm d}^3 \boldsymbol{r} \left\{ a \left[\epsilon |\psi|^2 + {\xi_0}^2 |(-{\rm i}\nabla)\psi|^2 \right] + \frac{b}{2} |\psi|^4 \right\}. \tag{2.2.16}$$

Here $\psi(\boldsymbol{r})$ $[= V^{-1/2} \sum_{\boldsymbol{q}} a_{\boldsymbol{q}0} \exp({\rm i}\boldsymbol{q}\cdot\boldsymbol{r})]$ is the classical order-parameter field in the coordinate representation, ϵ $[= (T - T_{\rm c})/T_{\rm c}]$ is the dimensionless temperature measured from the Gaussian critical temperature $T_{\rm c}$, and ξ_0 is the bare GL coherence length. In the following, since only the classical fluctuation described by $a_{\boldsymbol{q}0}$ is considered, we omit the suffix denoting the Matsubara index so that $a_{\boldsymbol{q}0}$ is simply expressed as $a_{\boldsymbol{q}}$. The coefficients in Eq. (2.2.16) are expressed as

$$a = \frac{U}{4T_{\rm c}V} \sum_{\boldsymbol{k}} {\varphi_k}^2 \left\{ Y_k - \frac{\partial\mu}{\partial T} \left[\frac{T_{\rm c}}{\xi_k} Y_k - 2 \left(\frac{T_{\rm c}}{\xi_k} \right)^2 X_k \right] \right\}, \tag{2.2.17}$$

$$b = \frac{U^2 T_{\rm c}}{V} \sum_{\boldsymbol{k}} {\varphi_k}^4 \left(\frac{X_k}{4{\xi_k}^3} - \frac{Y_k}{8T_{\rm c}{\xi_k}^2} \right), \tag{2.2.18}$$

$${\xi_0}^2 = \frac{U}{aV} \sum_{\boldsymbol{k}} {\varphi_k}^2 \frac{1}{16m{\xi_k}^2} \left(X_k - \frac{\xi_k}{2T_{\rm c}} Y_k + \frac{\xi_k k^2}{6m{T_{\rm c}}^2} X_k Y_k \right), \tag{2.2.19}$$

where $X_k = \tanh[\xi_k/(2T_{\rm c})]$ and $Y_k = {\rm sech}^2[\xi_k/(2T_{\rm c})]$. μ and $\partial\mu/\partial T$ appearing in Eqs. (2.2.17)-(2.2.19) are assumed to take their values at $T_{\rm c}$.

2.2.4 Zero-field SCF effect on specific heat

To calculate the SCF-induced specific heat in zero magnetic field, we have to incorporate the mode-coupling effect in some manner. To this end, we use the variational method [73] equivalent to the Hartree-Fock approximation, combined with the use of an effective high-energy cutoff of the SCF modes [74]. In the following, we explain the details of this treatment.

We divide the GL action ($\mathcal{S}_{\rm GL}$) into two parts as

$$\begin{aligned}\mathcal{S}_{\rm GL} &= \mathcal{S}^0_{\rm GL} + \mathcal{S}^1_{\rm GL} \\ &= \int {\rm d}^3\boldsymbol{r}\, a\left[\eta|\psi|^2 + {\xi_0}^2|(-{\rm i}\nabla)\psi|^2\right] + \int {\rm d}^3\boldsymbol{r}\,\left[a(\epsilon-\eta)|\psi|^2 + \frac{b}{2}|\psi|^4\right], \end{aligned} \tag{2.2.20}$$

where η is a variational parameter corresponding to the renormalized mass of the SCF. By tuning η to optimize a trial free-energy density given below, we expect that $\mathcal{S}^0_{\rm GL}$ will be dominant while $\mathcal{S}^1_{\rm GL}$ will be a small perturbation [75]. The free-energy density $f(\epsilon)$ can be estimated as

$$f = f_0 - \frac{T_{\rm c}}{V}\ln\langle {\rm e}^{-\mathcal{S}^1_{\rm GL}}\rangle^0_{\rm GL} \le f_0 + \frac{T_{\rm c}}{V}\langle \mathcal{S}^1_{\rm GL}\rangle^0_{\rm GL} \equiv f_{\rm tri}, \tag{2.2.21}$$

where $f_{\rm tri}(\epsilon;\eta)$ is a trial free-energy density, which should be optimized, i.e., minimized, with respect to η. Here $f_0(\eta)$ is the contribution from $\mathcal{S}^0_{\rm GL}$, and $\langle\cdots\rangle^0_{\rm GL}$ is the average with respect to $\mathcal{S}^0_{\rm GL}$.

As mentioned above, the GL action $\mathcal{S}_{\rm GL}$ is meaningful only for the low-energy SCF. Since $\mathcal{S}_{\rm GL}$ is isotropic in real space, it is natural that we should impose an isotropic cutoff in the momentum space. Accordingly, we simply introduce a high-energy (and short-wavelength) cutoff ${\xi_0}^2{q_{\rm c}}^2$. In other words, we restrict the SCF modes to those satisfying

$${\xi_0}^2 q^2 \le {\xi_0}^2{q_{\rm c}}^2 \equiv c^2, \tag{2.2.22}$$

where c is positive and $c = \mathcal{O}(1)$. Using this cutoff, we can obtain the explicit form of $f_0(\eta)$ as follows:

$$\begin{aligned} f_0(\eta) &= -\frac{T_{\rm c}}{V}\ln\int\left(\prod_{\boldsymbol{q}}\frac{{\rm dRe}a_{\boldsymbol{q}}\,{\rm dIm}a_{\boldsymbol{q}}}{\pi}\right){\rm e}^{-\mathcal{S}^0_{\rm GL}} \\ &= \frac{T_{\rm c}}{2\pi^2{\xi_0}^3}\left\{-\frac{2}{9}c^3 + \frac{2}{3}c\eta - \frac{2}{3}\eta^{3/2}\arctan\frac{c}{\sqrt{\eta}} + \frac{1}{3}c^3\ln\left[a\left(c^2+\eta\right)\right]\right\}. \end{aligned} \tag{2.2.23}$$

The optimizing equation $\partial f_{\rm tri}/\partial\eta = 0$ can be transformed into

$$\eta = \epsilon + \frac{2b}{a^2 T_{\rm c}}\frac{\partial f_0}{\partial\eta}. \tag{2.2.24}$$

Combining Eq. (2.2.23) and (2.2.24), we explicitly obtain the optimizing equation:

$$\eta = \epsilon + \frac{2}{\pi}\sqrt{Gi}\left(c - \sqrt{\eta}\arctan\frac{c}{\sqrt{\eta}}\right), \tag{2.2.25}$$

The Ginzburg number Gi in Eq. (2.2.25) represents the mode-coupling strength and is defined as

$$Gi = \left(\frac{b}{2\pi a^2 {\xi_0}^3} \right)^2 = \left(\frac{1}{2\pi \Delta c_V {\xi_0}^3} \right)^2, \tag{2.2.26}$$

where Δc_V is the mean-field jump of the specific heat at $T_{\rm c}$.

The trial free-energy density $f_{\rm tri}(\epsilon, \eta)$ can be rewritten as

$$f_{\rm tri}(\epsilon, \eta) = f_0 + (\epsilon - \eta) \frac{\partial f_0}{\partial \eta} + \frac{b}{T_{\rm c} a^2} \left(\frac{\partial f_0}{\partial \eta} \right)^2. \tag{2.2.27}$$

The optimized free-energy density $f_{\rm opt}(\epsilon)$ can be obtained from the combination of Eqs. (2.2.24) and (2.2.27). The entropy density $s(\epsilon)$ and specific heat $c_V(\epsilon)$ around $T_{\rm c}$ are respectively given as

$$s = -\frac{\partial f_{\rm opt}}{\partial T} = -\frac{1}{2\pi^2 {\xi_0}^3} \left(c - \sqrt{\eta^*} \arctan \frac{c}{\sqrt{\eta^*}} \right) \tag{2.2.28}$$

and

$$c_V = T_{\rm c} \frac{\partial s}{\partial T}, \tag{2.2.29}$$

where η^* is the solution of the optimizing equation [Eq. (2.2.25)]. We note that small temperature dependence irrelevant to ϵ is neglected.

2.2.5 Renormalization of critical temperature and coherence length at zero temperature

Now we examine how the critical temperature and the coherence length are renormalized via the mode coupling between the SCFs. The mode coupling decreases the critical temperature $T_{\rm c}$, which is defined within the Gaussian approximation, down to a renormalized critical temperature $T_{\rm cR}$. In the context of the ultra-cold atomic gases, $T_{\rm cR}$ has been theoretically estimated as a function of U using various methods. They include, e.g., the quantum Monte Carlo method [38, 39, 40] and the self-consistent T-matrix approximation [32]. In our formalism, $T_{\rm cR}$ is determined from Eq. (2.2.25) by setting the renormalized mass η to zero:

$$T_{\rm cR} = \left(1 - \frac{2c}{\pi} \sqrt{Gi} \right) T_{\rm c}. \tag{2.2.30}$$

When T is so close to $T_{\rm cR}$ that the condition $\eta \ll c$ is satisfied, Eq. (2.2.25) can be rewritten as

$$\eta = \frac{T - T_{\rm cR}}{T_{\rm c}} - \sqrt{Gi}\, \sqrt{\eta}. \tag{2.2.31}$$

Therefore, the renormalized mass η is asymptotically given as

$$\eta \simeq \begin{cases} \dfrac{T - T_{\rm cR}}{T_{\rm c}} & \left(Gi \ll \dfrac{T - T_{\rm cR}}{T_{\rm c}} \ll c \right) \\ \dfrac{1}{Gi} \left(\dfrac{T - T_{\rm cR}}{T_{\rm c}} \right)^2 & \left(\dfrac{T - T_{\rm cR}}{T_{\rm c}} \ll Gi \right). \end{cases} \tag{2.2.32}$$

Thus when $Gi \ll (T - T_{\rm cR})/T_{\rm c} \ll c$, the dominant part of the GL action $\mathcal{S}^0_{\rm GL}$ can be approximated as follows:

$$\begin{aligned}\mathcal{S}^0_{\rm GL} &\simeq \int {\rm d}^3\boldsymbol{r} \left(\frac{T_{\rm cR}}{T_{\rm c}}\right) a \left[\frac{T - T_{\rm cR}}{T_{\rm cR}}|\psi|^2 + \frac{T_{\rm c}}{T_{\rm cR}}{\xi_0}^2|(-{\rm i}\nabla)\psi|^2\right] \\ &= \int {\rm d}^3\boldsymbol{r}\, a_{\rm R}\left[\epsilon_{\rm R}|\psi|^2 + {\xi_{0\rm R}}^2|(-{\rm i}\nabla)\psi|^2\right], \end{aligned} \tag{2.2.33}$$

where the renormalized parameters are given as

$$a_{\rm R} = \left(\frac{T_{\rm cR}}{T_{\rm c}}\right) a, \tag{2.2.34}$$

$$\epsilon_{\rm R} = \frac{T - T_{\rm cR}}{T_{\rm cR}}, \tag{2.2.35}$$

$${\xi_{0\rm R}}^2 = \frac{T_{\rm c}}{T_{\rm cR}}{\xi_0}^2. \tag{2.2.36}$$

From Eq. (2.2.36), we find that the coherence length is renormalized along with the renormalization of the critical temperature. Thus, it is not the bare depairing field (the so-called upper critical field) $B_{\rm c2}(T)$ $[= \phi_0(T_{\rm c} - T)/(2\pi{\xi_0}^2 T_{\rm c})]$ but the corresponding renormalized one

$$B_{\rm c2R}(T) \equiv \frac{\phi_0(T_{\rm cR} - T)}{2\pi{\xi_{0\rm R}}^2 T_{\rm cR}} \tag{2.2.37}$$

that is estimated from conventional experiments, where ϕ_0 is the flux quantum. That is, since the coherence length determined experimentally will be not ξ_0 but $\xi_{0\rm R}$, one should pay attention to the difference between ξ_0 and $\xi_{0\rm R}$ especially when the mode coupling is important as in the BCS-BEC crossover regime. Similar renormalization of the coherence length due to the reduction of the critical temperature has also been stressed in the context of underdoped cuprates [76].

In studying a disordered superconductor with s-wave pairing, a reduction of $T_{\rm c}$ of the type shown in Eq. (2.2.30) may occur due to an interplay between the repulsive interaction and the disorder especially in low-dimensional materials [77, 78, 79]. In the 3D and clean superconductor FeSe of our interest, however, such an origin of $T_{\rm c}$ reduction is not expected to be effective.

According to Eq. (2.2.32), the temperature dependence of the correlation length $\xi_{\rm R}(T) = \xi_{0\rm R}/\sqrt{\eta(T)}$ defined above the superconducting transition is changed on approaching $T_{\rm cR}$, and we have $\xi_{\rm R}(T) \sim (T - T_{\rm cR})^{-1}$ in the vicinity of $T_{\rm cR}$. Consequently, within the present Hartree-Fock approach, the critical behaviors of physical quantities may be remarkably different from those in the Gaussian approximation where $\xi_{\rm R}(T) \sim (T - T_{\rm cR})^{-1/2}$. As an illustration, we focus here on the diamagnetic susceptibility $\chi_{\rm dia}$ and the specific heat c_V. Noting that the singular part of the free-energy density behaves like $-T_{\rm c}/[\xi_{\rm R}(T)]^3$ and that a change of the flux density carries the factor $[\xi_{\rm R}(T)]^2$ due to the gauge invariance while c_V is the second derivative of the free-energy density with respect to T, one finds that $\chi_{\rm dia} \propto (T - T_{\rm cR})^{-1}$ while c_V saturates a finite value in the vicinity of $T_{\rm cR}$.

2.2.6 SCF effect on specific heat and diamagnetism in magnetic fields

In non-zero magnetic fields, $-\mathrm{i}\nabla$ in the GL action [Eq. (2.2.16)] needs to be replaced with $-\mathrm{i}\nabla + 2\pi\boldsymbol{A}/\phi_0$. Here, $\boldsymbol{A}(\boldsymbol{r})$ [$= (0, Bx, 0)$] is the vector potential in the Landau gauge. As far as the paramagnetic pair-breaking effect is negligible, the resulting GL action will correctly describe the low-energy SCF around T_c in magnetic fields.

To estimate the SCF-induced diamagnetism and specific heat in magnetic fields, we use the variational method combined with the introduction of a certain cutoff as in the zero-field case, which is explained in the following.

We first divide the action $\mathcal{S}_\mathrm{GL}$ in magnetic fields into two parts:

$$\begin{aligned}\mathcal{S}_\mathrm{GL} &= \mathcal{S}^0_\mathrm{GL} + \mathcal{S}^1_\mathrm{GL} \\ &= \int \mathrm{d}^3\boldsymbol{r}\, a \left[\eta|\psi|^2 + {\xi_0}^2 \left|\left(-\mathrm{i}\nabla + \frac{2\pi}{\phi_0}\boldsymbol{A}\right)\psi\right|^2\right] \\ &\quad + \int \mathrm{d}^3\boldsymbol{r} \left[a\,(\epsilon - \eta)\,|\psi|^2 + \frac{b}{2}|\psi|^4\right]. \end{aligned} \tag{2.2.38}$$

Then, in quite the same way as in the zero-field case, the trial free-energy density f_tri is estimated with f_0. We stress that the equations determining the optimized free-energy density f_opt [Eqs. (2.2.21), (2.2.24), and (2.2.27)] are just the same as in the zero-field case (the explicit form of f_0 is explained in the next paragraph). However, the order-parameter field in magnetic fields needs to be expanded as

$$\psi(\boldsymbol{r}) = \sum_{N,q_y,q_z} b_{Nq_yq_z} f_{Nq_y}(x) \frac{\mathrm{e}^{\mathrm{i}q_y y}}{\sqrt{L_y}} \frac{\mathrm{e}^{\mathrm{i}q_z z}}{\sqrt{L_z}}, \tag{2.2.39}$$

where N is the Landau-level index, $f_{Nq_y}(x)$ is the Nth-Landau-level eigen function, and $b_{Nq_yq_z}$ is the expansion coefficient describing the SCF mode in magnetic fields. By using this representation, $\mathcal{S}^0_\mathrm{GL}$ is written as

$$\mathcal{S}^0_\mathrm{GL} = \sum_{N,q_y,q_z} a\left[\eta + 2h\left(N + \frac{1}{2}\right) + {\xi_0}^2 {q_z}^2\right] |b_{Nq_yq_z}|^2, \tag{2.2.40}$$

where h [$= 2\pi{\xi_0}^2 B/\phi_0 \equiv B/B_{\mathrm{c}2}(0)$] is a dimensionless magnetic field. Changing the integral variables from $\{a_{\boldsymbol{q}}, a^*_{\boldsymbol{q}}\}$ into $\{b_{Nq_yq_z}, b^*_{Nq_yq_z}\}$ [cf. Eq. (2.2.23)] leads to the following formula of f_0:

$$f_0 = -\frac{T_\mathrm{c}}{V} \ln \int \left(\prod_{N,q_y,q_z} \frac{\mathrm{dRe}b_{Nq_yq_z}\,\mathrm{dIm}b_{Nq_yq_z}}{\pi}\right) \mathrm{e}^{-\mathcal{S}^0_\mathrm{GL}}. \tag{2.2.41}$$

Since $\mathcal{S}_\mathrm{GL}$ cannot correctly describe the high-energy SCF, we should introduce a high-energy cutoff ${\xi_0}^2 {q_\mathrm{c}}^2$ in a similar way to Eq. (2.2.22). Here we restrict the SCF modes to those

satisfying

$$\begin{cases} 2h(N+1) + {\xi_0}^2 {q_z}^2 \leq {\xi_0}^2 {q_c}^2 \equiv c^2 \\ {\xi_0}^2 {q_z}^2 \leq {\xi_0}^2 {q_c}^2. \end{cases} \tag{2.2.42}$$

We note that the factor $N+1$ is different from $N+1/2$ appearing in Eq. (2.2.40). Combining Eqs. (2.2.40), (2.2.41), and (2.2.42) leads to the following explicit form of f_0:

$$f_0(h;\eta) = \frac{T_c}{2\pi^2 {\xi_0}^3} \left[\frac{c^3}{3} \ln(2ah) + h I_0(h;\eta) \right], \tag{2.2.43}$$

where

$$I_0(h;\eta) = \int_0^c \mathrm{d}x \left[\ln \Gamma \left(\frac{\eta + c^2}{2h} + \frac{1}{2} \right) - \ln \Gamma \left(\frac{\eta + x^2}{2h} + \frac{1}{2} \right) \right]. \tag{2.2.44}$$

Here $\Gamma(x)$ is the gamma function. With the use of Eqs. (2.2.24) and (2.2.43), the explicit form of the optimizing equation is given by

$$\eta = \epsilon + \frac{1}{\pi} \sqrt{Gi} I_1(h;\eta), \tag{2.2.45}$$

where

$$I_1(h;\eta) = \int_0^c \mathrm{d}x \left[\psi \left(\frac{\eta + c^2}{2h} + \frac{1}{2} \right) - \psi \left(\frac{\eta + x^2}{2h} + \frac{1}{2} \right) \right]. \tag{2.2.46}$$

Here $\psi(x) = \mathrm{d} \ln \Gamma(x)/\mathrm{d}x$ is the digamma function.

Now we explain why we choose the seemingly strange cutoff condition [Eq. (2.2.42)]. Considering the zero-field limit ($h \to 0$) in the finite-field expression of f_0 [Eq. (2.2.43)] and using the asymptotic form of the Gamma function, we can obtain the zero-field expression of f_0 [Eq. (2.2.23)]. As mentioned above, moreover, the equations determining the optimized free-energy density f_{opt} in the finite-field case are just the same as in the zero-field case and given by Eqs. (2.2.21), (2.2.24), and (2.2.27). In other words, *we can consistently reproduce the zero-field isotropic behavior if we adopt the cutoff condition given by Eq. (2.2.42).* This is the reason why we choose the cutoff condition given by Eq. (2.2.42).

The entropy density $s(\epsilon, h)$ is calculated as

$$s = -\frac{\partial f_{\mathrm{opt}}}{\partial T} = -\frac{1}{4\pi^2 {\xi_0}^3} I_1(h;\eta^*), \tag{2.2.47}$$

where η^* is the solution of the optimizing equation [Eq. (2.2.45)]. The specific heat $c_V(\epsilon, h)$ around T_c is calculated as

$$c_V = T_c \frac{\partial s}{\partial T} \tag{2.2.48}$$

The magnetization $M_{\mathrm{dia}}(\epsilon, h)$ is estimated as

$$M_{\mathrm{dia}} = -\frac{\partial f_{\mathrm{opt}}}{\partial B} = -\frac{T_c}{\pi \phi_0 \xi_0} \left[\frac{c^3}{3h} + I_0(h;\eta^*) - I_3(h;\eta^*) \right], \tag{2.2.49}$$

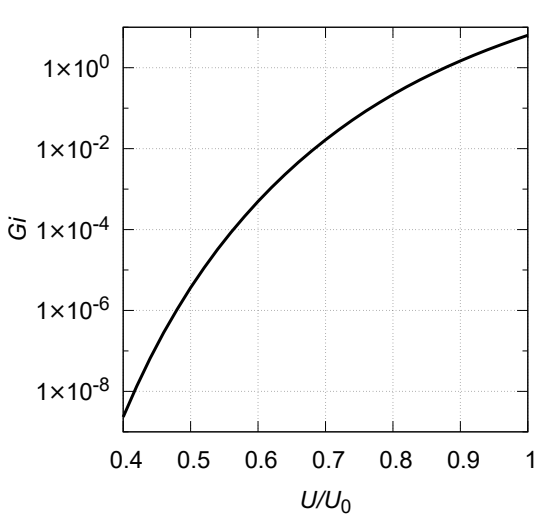

Figure 2.1: The Ginzburg number Gi as a function of the interaction strength U. The vertical scale is logarithmic.

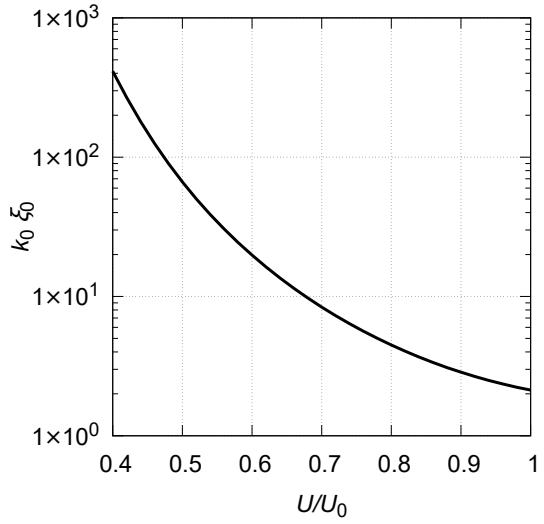

Figure 2.2: The bare coherence length ξ_0 as a function of the interaction strength U. The vertical scale is logarithmic.

where

$$I_3(h;\eta) = \int_0^c \mathrm{d}x \left[\frac{\eta + c^2}{2h} \psi\left(\frac{\eta + c^2}{2h} + \frac{1}{2} \right) - \frac{\eta + x^2}{2h} \psi\left(\frac{\eta + x^2}{2h} + \frac{1}{2} \right) \right].$$

The diamagnetic susceptibility $\chi_{\mathrm{dia}}(\epsilon, h)$ is simply defined as $\chi_{\mathrm{dia}} = \mu_0 M_{\mathrm{dia}}/B$, where μ_0 is the vacuum permeability.

Before finishing this section, we note some comments. If we consider the zero-field case ($h \to 0$) in addition to neglecting both of the mode-coupling effect ($\eta \to \epsilon$) and the cutoff effect ($c \to \infty$), c_V approaches the familiar result in the Gaussian approximation:

$$c_V \to \frac{1}{8\pi {\xi_0}^3} \frac{1}{\sqrt{\epsilon}}. \tag{2.2.50}$$

On the other hand, if we neglect both of the mode-coupling effect ($\eta \to \epsilon$) and the cutoff effect ($c \to \infty$) while keeping the magnetic field finite, we obtain

$$M_{\mathrm{dia}} \to -\frac{T_{\mathrm{c}}}{\pi \phi_0 \xi_0} \int_0^\infty \mathrm{d}x \Upsilon\left(\frac{\epsilon + x^2}{2h} + \frac{1}{2} \right), \tag{2.2.51}$$

where

$$\Upsilon(x) = -\ln \Gamma(x) + \left(x - \frac{1}{2} \right) \psi(x) - x + \frac{1}{2} \left[1 + \ln(2\pi) \right]. \tag{2.2.52}$$

This formula of magnetization is equivalent to the well-known Prange's result [80].

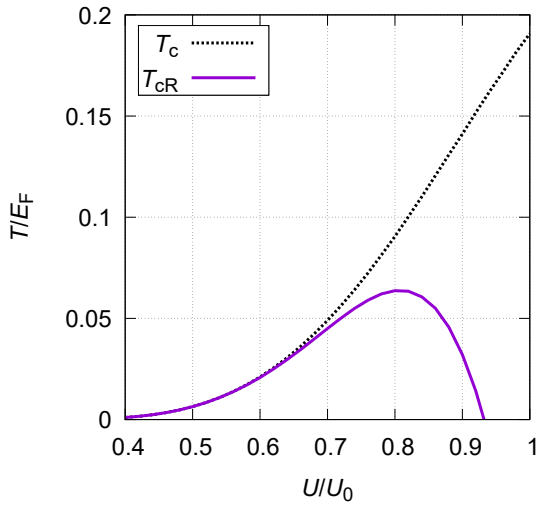

Figure 2.3: The bare critical temperature T_c (black dotted line) and the renormalized critical temperature T_{cR} (purple solid line) as a function of the interaction strength U. Our theoretical approach seems to be valid when $U/U_0 \lesssim 0.8$.

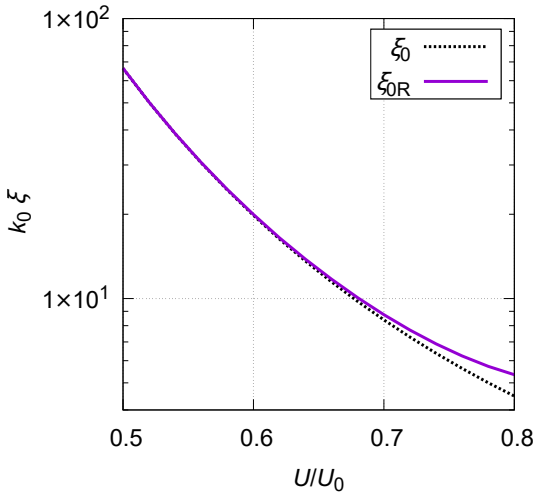

Figure 2.4: The bare coherence length ξ_0 (black dotted line) and the renormalized coherence length ξ_{0R} (purple solid line) as a function of the interaction strength U. The vertical scale is logarithmic.

2.3 Fluctuation-induced thermodynamic quantities

In the following, we show the obtained thermodynamic quantities estimated with the approach explained in Sec. 2.2. First, we fix some parameters to investigate the BCS-BEC crossover regime as well as the weak-coupling BCS regime. Next, the renormalizations of the critical temperature and the coherence length are shown to be quantitatively large in the BCS-BEC crossover regime. Then, we demonstrate that the obtained specific heat and diamagnetic susceptibility can exceed in magnitude their Gaussian-approximation values. Next, we explain that the so-called lowest-Landau-level scaling, observed in high-T_c cuprates [68], can break down in the BCS-BEC crossover regime due to an increase [81] of Gi, which measures the strength of the mode coupling. Finally, we illustrate that the crossing behavior of magnetization curves, often observed in 2D high-T_c cuprates, can still occur in the present 3D systems over a broad field range in the BCS-BEC crossover regime, even though the lowest-Landau-level scaling is not satisfied.

2.3.1 Parameters

As a preliminary, we note the values of some parameters used in our numerical calculations. First, by using the momentum cutoff [k_0 appearing in Eq. (2.2.2)], we fix the total number

density as $n_{\rm tot}{k_0}^{-3} \simeq 0.007$, which corresponds to a relatively dilute electron system. Next, the effective high-energy cutoff is fixed as $c = \xi_0 q_{\rm c} = 1$ [see Eq. (2.2.42)], where ξ_0 is the bare coherence length and $q_{\rm c}$ is the short-wavelength cutoff of the SCF mode. There is a tendency for the obtained results to be qualitatively insensitive to c as long as c is small.

As mentioned in Sec. 2.1, the critical region or the Ginzburg number Gi is expected be large in the BCS-BEC crossover regime. Hence, to fix a typical value of the attractive-interaction strength U in each of the BCS and BCS-BEC crossover regime, we check the U dependence of Gi and obtain the result[1] shown in Fig. 2.1, where U is measured in units of $U_0 = 4\pi/(mk_0)$, which is the threshold value necessary to form a two-particle bound state (see Sec. 2.2.1). Figure 2.1 shows that Gi rapidly increases as U becomes large. Reflecting the well-known expression of $T_{\rm c}$ valid in the BCS regime [12], $T_{\rm c} \propto \exp[-1/(N_{\rm F}U)]$ and $\Delta c_V \propto T_{\rm c}$, where $N_{\rm F}$ is the density of states at the Fermi surface; thus, ξ_0 ($\propto {T_{\rm c}}^{-1}$) sharply decreases as U increases at least in the BCS regime (Fig. 2.2). Since $Gi \propto (\Delta c_V {\xi_0}^3)^{-2} \propto {T_{\rm c}}^4$, the rapid increase of Gi is mainly due to the sharp decrease of ξ_0. From Fig. 2.1, we assume that $U/U_0 = 0.5$ ($Gi \sim 10^{-6}$) and $U/U_0 = 0.8$ ($Gi \sim 0.2$) correspond to the values for typical BCS and BCS-BEC crossover regimes, respectively.

2.3.2 Critical temperature and coherence length

The bare critical temperature $T_{\rm c}$ and the critical temperature $T_{\rm cR}$ renormalized by the mode coupling between SCF (see Sec. 2.2.5) are shown in Fig. 2.3. Here the temperatures are measured in units of the Fermi energy $E_{\rm F}$ [$= (3\pi^2 n_{\rm tot})^{2/3}/(2m)$]. We see from Fig. 2.3 that the renormalization (or lowering) of the critical temperature is enhanced in the BCS-BEC crossover regime. This is because of the strong mode coupling between SCFs, or the large value of Gi, as mentioned in Sec. 2.3.1. We also see that $T_{\rm cR}$ starts to decrease as a function of U when U/U_0 exceeds around 0.8. This may mean that our theoretical approach, the variational method on the GL action combined with the effective high-energy cutoff, is improper when $U/U_0 \gtrsim 0.8$. In other words, we believe that our approach should be applicable if $U/U_0 \lesssim 0.8$. Therefore, we restrict our analysis of the SCF effects to the interaction range satisfying $U/U_0 \leq 0.8$. We note that this interaction range includes the BCS ($U/U_0 = 0.5$) and BCS-BEC crossover ($U/U_0 = 0.8$) regimes defined in Sec. 2.3.1.

Figure 2.4 shows the renormalized coherence length $\xi_{0\rm R}$ and the bare one ξ_0 within the range of the interaction satisfying $U/U_0 \leq 0.8$. We see that the renormalized coherence length is elongated compared with the bare one especially in the BCS-BEC crossover regime.

[1] We neglect the term proportional to $\partial\mu/\partial T$ in Eq. (2.2.17) since this term is small compared to the other term at least in the interaction range $U/U_0 \lesssim 1$.

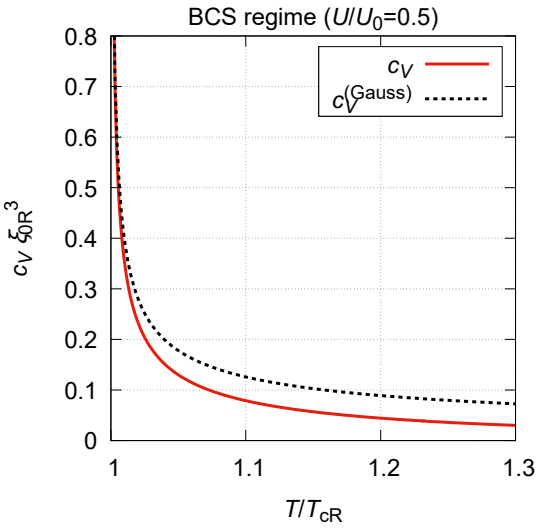

Figure 2.5: SCF-induced specific heat in the low-field limit as a function of temperature in the BCS regime. The numerical result (red solid line) is shown with the result in the Gaussian approximation (black dotted line).

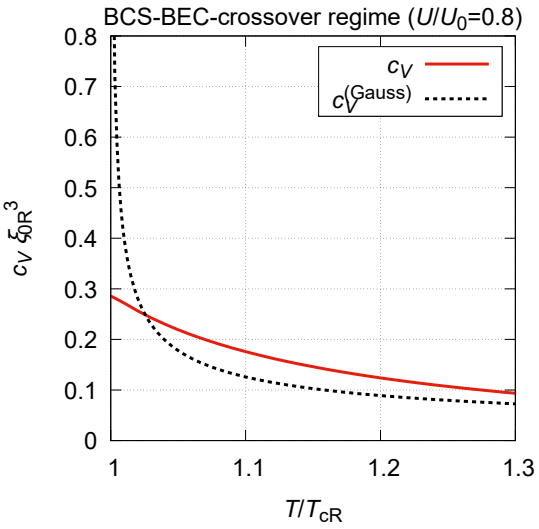

Figure 2.6: SCF-induced specific heat in the low-field limit as a function of temperature in the BCS-BEC crossover regime. The meaning of lines is the same as in Fig. 2.5. We note that, as explained at the end of subsection 2.2.5, the renormalized specific heat saturates a finite value within the present method (see the red solid curve).

2.3.3 Specific heat and diamagnetic susceptibility

Before discussing the calculated specific heat and diamagnetic susceptibility, we mention the well-known results in the Gaussian approximation in the low-field limit. We first consider the case where the mode coupling is so weak as in the BCS regime that $\xi_{0\mathrm{R}} \simeq \xi_0$ and $T_{\mathrm{cR}} \simeq T_{\mathrm{c}}$. At temperatures higher than the critical temperature where the mode coupling between SCF is negligible (i.e., outside the critical region), it is known [see Eq. (2.2.50)] that the SCF-induced specific heat $\tilde{c}_V^{(\mathrm{Gauss})}$ is represented as

$$\tilde{c}_V^{(\mathrm{Gauss})} = \frac{1}{8\pi}\frac{1}{{\xi_0}^3\sqrt{T/T_{\mathrm{c}}-1}}, \tag{2.3.1}$$

and that the SCF-induced diamagnetic susceptibility $\tilde{\chi}_{\mathrm{dia}}^{(\mathrm{Gauss})}$ is represented as [65]

$$\tilde{\chi}_{\mathrm{dia}}^{(\mathrm{Gauss})} = -\frac{\pi\mu_0}{6{\phi_0}^2}\frac{\xi_0 T_{\mathrm{c}}}{\sqrt{T/T_{\mathrm{c}}-1}}, \tag{2.3.2}$$

where μ_0 is the vacuum permeability. On the other hand, if the mode coupling is strong as in the BCS-BEC crossover regime, the experimentally determined coherence length and critical

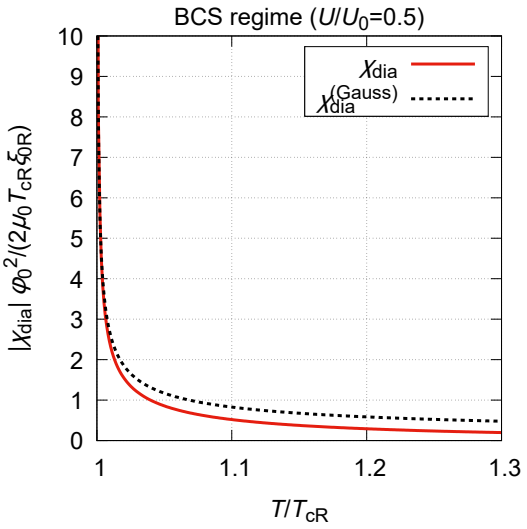

Figure 2.7: SCF-induced diamagnetic susceptibility in the low-field limit as a function of temperature in the BCS regime. The numerical result (red solid line) is shown with the result in the Gaussian approximation (black dotted line). We note that $\chi_{\rm dia}$ is measured in units of $[{\phi_0}^2/(2\mu_0 T_{\rm cR}\xi_{0\rm R})]^{-1}$.

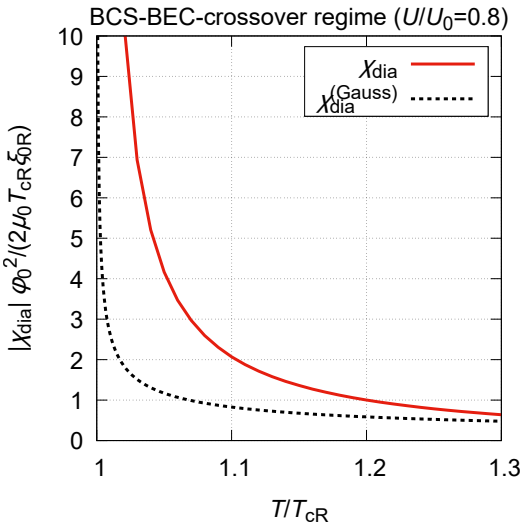

Figure 2.8: SCF-induced diamagnetic susceptibility in the low-field limit as a function of temperature in the BCS-BEC crossover regime. The meaning of lines is the same as in Fig. 2.7.

temperature will be the renormalized ones $\xi_{0\rm R}$ ($>\xi_0$) and $T_{\rm cR}$ ($<T_{\rm c}$), respectively. Thus, if we use these experimentally determined values, Eqs. (2.3.1) and (2.3.2) should be replaced respectively with

$$c_V^{(\rm Gauss)} = \frac{1}{8\pi}\frac{1}{{\xi_{0\rm R}}^3\sqrt{T/T_{\rm cR}-1}} \tag{2.3.3}$$

and

$$\chi_{\rm dia}^{(\rm Gauss)} = -\frac{\pi\mu_0}{6{\phi_0}^2}\frac{\xi_{0\rm R}T_{\rm cR}}{\sqrt{T/T_{\rm cR}-1}}. \tag{2.3.4}$$

Therefore, *even the expression of thermodynamic quantities in the Gaussian approximation can be greatly affected by the mode coupling in the BCS-BEC crossover regime.*

First, let us start with our numerical results of the specific heat in the low-field limit. Figures 2.5 and 2.6 respectively show the temperature dependence of the specific heat in the BCS and BCS-BEC crossover regimes. In each figure, the red solid line is our numerical result, while the black dotted line is the analytical result in the Gaussian approximation [Eq. (2.3.3)].

In the BCS regime (Fig. 2.5), the numerical result is in accord with that in the Gaussian approximation if T is sufficiently close to $T_{\rm cR}$ ($T/T_{\rm cR}-1\lesssim 0.01$), which is consistent with

the fact that mode coupling is so weak (*i.e.*, $Gi \sim 10^{-6} \ll 1$) that the critical behavior cannot appear except in a very narrow temperature range ($T/T_{\rm cR} - 1 \lesssim 10^{-6}$). When $T/T_{\rm cR} - 1 \gtrsim 0.01$, on the other hand, the numerical value is smaller than the Gaussian-approximation value. This is simply caused by the high-energy cutoff c [see Eqs. (2.2.22) and (2.2.42)], which is not used in the conventional Gaussian approximation and effectively suppresses the SCF-induced thermodynamic response.

In the BCS-BEC crossover regime (Fig. 2.6), the numerical result does not fit anymore that in the Gaussian approximation due to the strong mode coupling. In contrast to the BCS regime (Fig. 2.5), the numerical value is larger than the Gaussian-approximation value when the temperature is relatively far from $T_{\rm cR}$ ($T/T_{\rm cR} - 1 \gtrsim 0.03$). We note that saturation of the specific heat $c_V(T)$ at $T_{\rm cR}$ in Fig. 2.6 is an artifact of the Hartree-Fock approximation used here (see the last paragraph of Sec. 2.2.5).

Next, we show our numerical results of the diamagnetic susceptibility in the low-field limit. Figures 2.7 and 2.8 respectively show the temperature dependence of the diamagnetic susceptibility in the BCS and BCS-BEC crossover regimes. In each figure, the red solid line is the numerical result, while the black dotted line is the analytical result in the Gaussian approximation [Eq. (2.3.4)] in the same way as in Figs. 2.5 and 2.6.

In the BCS regime (Fig. 2.7), the Gaussian approximation is appropriate as the specific-heat result if $T/T_{\rm cR} - 1 \lesssim 0.01$ and the cutoff effect appears if $T/T_{\rm cR} - 1 \gtrsim 0.01$. We note that this kind of cutoff effect on diamagnetic susceptibility has been experimentally observed in conventional superconductors [82].

In the BCS-BEC crossover regime (Fig. 2.8), the numerical value is larger than the Gaussian-approximation value, which is caused by the strong mode coupling as in the case of specific heat. The obtained feature is qualitatively consistent with the data [6] in FeSe.

It should be noted that, in a disordered superconductor, an effective granularity is not negligible in the vicinity of the criticality of the zero-field transition [83]. Our main interest in the present work consists in the fluctuation effects in a non-zero magnetic field where a criticality is absent until reaching a vortex-glass transition at a much lower temperature.

2.3.4 Lowest-Landau-level scaling

In this subsection, we investigate whether the obtained temperature and field dependences of the specific heat and the magnetization follow the so-called lowest-Landau-level (LLL) scaling around $B_{\rm c2R}(T)$, or the renormalized $B_{\rm c2}(T)$ [see Eq. (2.2.37)]. Before moving on to the results, we review the properties of SCF in high magnetic fields, including the LLL scaling. In high magnetic fields, if the mode coupling between SCFs is moderately strong, the LLL ($N = 0$) modes of the order parameter field $\psi(\boldsymbol{r})$ in Eq. (2.2.39) have a dominant impact on thermodynamic and transport properties [71] compared to other higher-LL modes [$N \geq 1$ modes of $\psi(\boldsymbol{r})$]. Such restriction of SCF to the LLL modes leads to the effective

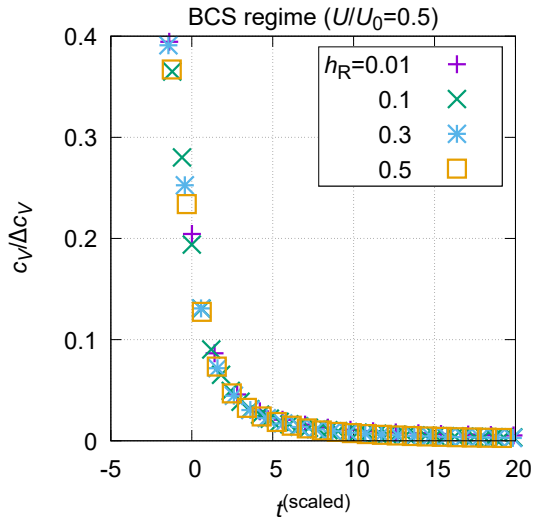

Figure 2.9: LLL-scaling plot of the SCF-induced specific heat in the BCS regime. $t^{(\mathrm{scaled})}$ is the scaled temperature and h_R is a magnetic field in units of $B_{\mathrm{c2R}}(0)$ [see Eq. (2.2.37)].

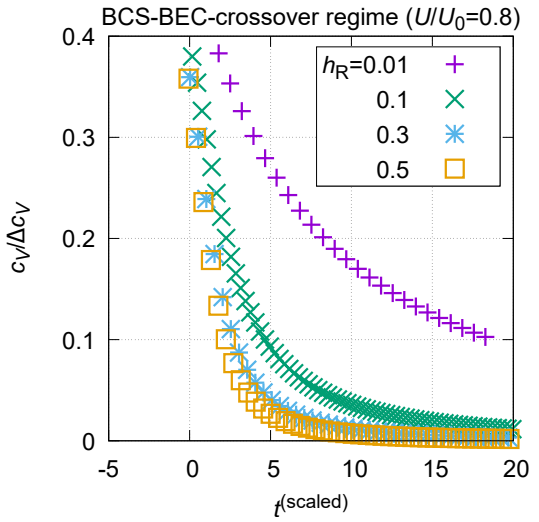

Figure 2.10: LLL-scaling plot of the SCF-induced specific heat in the BCS-BEC crossover regime. The symbols are used in the same way as in Fig. 2.9.

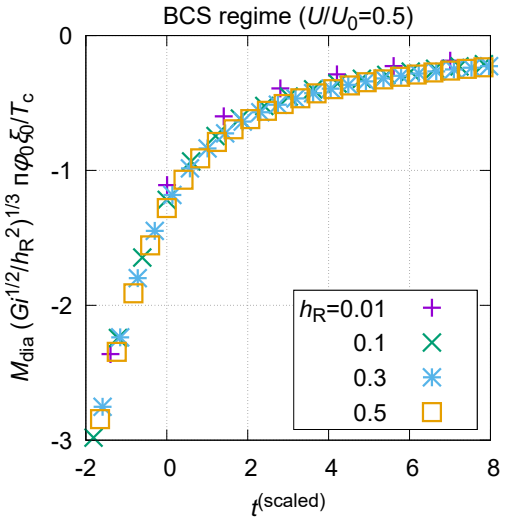

Figure 2.11: LLL-scaling plot of the SCF-induced magnetization in the BCS regime. $t^{(\mathrm{scaled})}$ is the scaled temperature and h_R is a magnetic field in units of $B_{\mathrm{c2R}}(0)$.

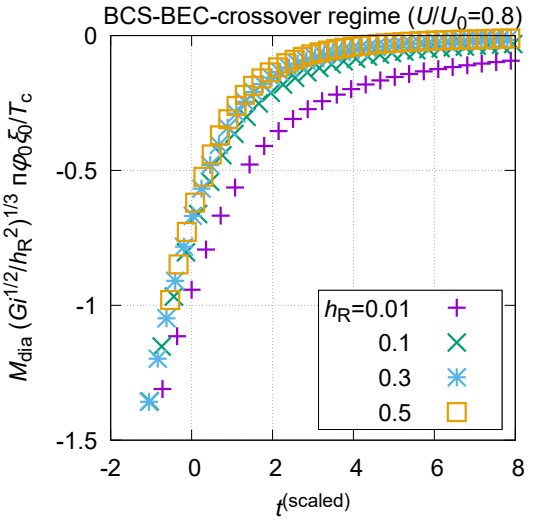

Figure 2.12: LLL-scaling plot of the SCF-induced magnetization in the BCS-BEC crossover regime. The symbols are used in the same way as in Fig. 2.11.

reduction of dimensionality (from 3D to 1D) [84], which changes the second-order B_{c2} transition in the mean-field approximation to a crossover and creates the first-order vortex-melting transition [85]. Moreover, the restriction to the LLL modes simplifies the dependences of the free energy on temperature and magnetic field [86], so that temperature and field dependences of thermodynamic quantities such as the specific heat and the magnetization are also simplified [87] as follows:

$$\frac{c_V}{\Delta c_V} = F_1(t^{(\mathrm{scaled})}), \tag{2.3.5}$$

$$M_{\mathrm{dia}} \times \left(\frac{\sqrt{Gi}}{{h_{\mathrm{R}}}^2} \right)^{1/3} = F_2(t^{(\mathrm{scaled})}). \tag{2.3.6}$$

Here, Δc_V is the mean-field specific-heat jump [see Eq. (2.2.26)], $F_1(x)$ and $F_2(x)$ are certain scaling functions, the dimensionless temperature $t^{(\mathrm{scaled})}$ is given as

$$t^{(\mathrm{scaled})} = \frac{\epsilon_{\mathrm{R}} + h_{\mathrm{R}}}{(\sqrt{Gi}\, h_{\mathrm{R}})^{2/3}}, \tag{2.3.7}$$

ϵ_{R} $(= T/T_{\mathrm{cR}} - 1)$ is the dimensionless temperature, and h_{R} $[= 2\pi {\xi_{0\mathrm{R}}}^2 B/\phi_0 \equiv B/B_{\mathrm{c2R}}(0)]$ is the dimensionless magnetic field, where $B_{\mathrm{c2R}}(T)$ is the renormalized counterpart of $B_{c2}(T)$ [see Eq. (2.2.37)]. The relations such as Eqs. (2.3.5) and (2.3.6), which are based on the restriction of SCF to the LLL modes, are called the LLL scaling. Using the LLL-scaling plot, we can check whether the LLL modes are dominant or not.

Figures 2.9 and 2.10 show the LLL-scaling plots of the specific heat in the BCS and BCS-BEC crossover regimes, respectively. From Fig. 2.9, we see that the LLL scaling is satisfied, which means that the LLL modes are dominant in the BCS regime. On the other hand, Fig. 2.10 shows that the LLL scaling breaks down, which means that the higher-LL modes are important as well as the LLL modes in the BCS-BEC crossover regime. This can be understood as an effect of the strong mode coupling, which makes the contribution of the LLL modes less dominant. In fact, the renormalized fluctuation theory for the weak-coupling BCS regime has indicated that the higher-LL modes are not negligible in describing the SCF in lower fields satisfying [81]

$$B < B_{\mathrm{c2R}}(0)\, Gi. \tag{2.3.8}$$

This expression implies that, as the mode coupling increases, the LLL scaling is expected to break down.

Figures 2.11 and 2.12 show the LLL-scaling plots of the magnetization in the BCS and BCS-BEC crossover regimes, respectively. The LLL scaling is satisfied in the BCS regime, while it breaks down in the BCS-BEC crossover regime consistently with the result of the specific heat (Figs. 2.9 and 2.10).

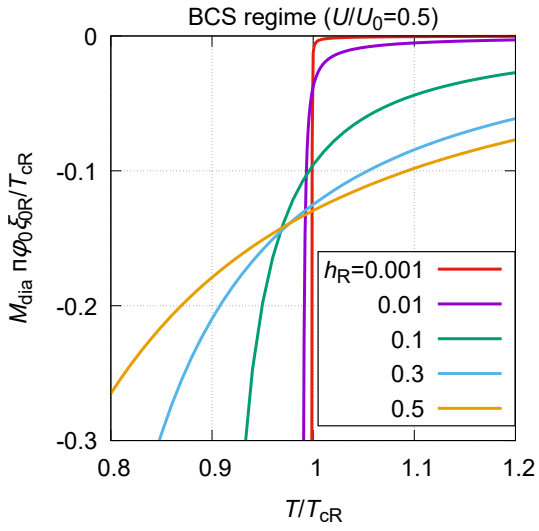

Figure 2.13: SCF-induced magnetization as a function of temperature in the BCS regime. $h_{\rm R}$ is a magnetic field in units of $B_{\rm c2R}(0)$. We note that $M_{\rm dia}$ is measured in units of $(\pi\phi_0\xi_{0\rm R}/T_{\rm cR})^{-1}$.

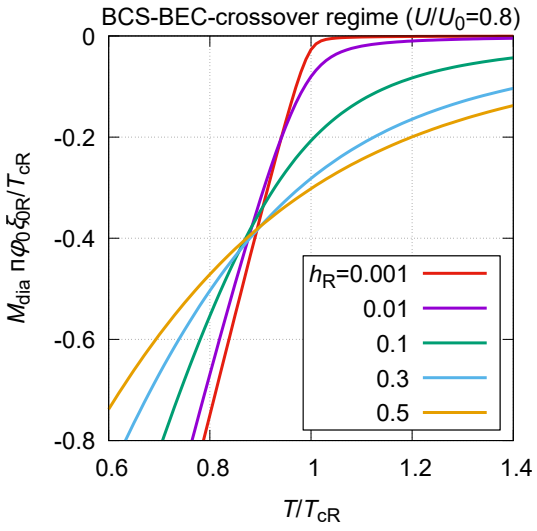

Figure 2.14: SCF-induced magnetization as a function of temperature in the BCS-BEC crossover regime. The symbols are used in the same way as in Fig. 2.13. We see from Figs. 2.3 and 2.4 that the unit of $M_{\rm dia}$, $(\pi\phi_0\xi_{0\rm R}/T_{\rm cR})^{-1}$, is about 100 times larger than that in the BCS regime (Fig. 2.13).

2.3.5 Crossing of magnetization curves

In this subsection, the crossing behavior of the magnetization curves, which has been experimentally observed in FeSe [6], is investigated in both the BCS and BCS-BEC crossover regimes. Figures 2.13 and 2.14 show the obtained SCF-induced magnetization curves in the BCS and BCS-BEC crossover regimes, respectively. We note that the LLL-scaling plots shown in Figs. 2.11 and 2.12 can be obtained respectively from Figs. 2.13 and 2.14 by using $t^{(\rm scaled)}$ instead of T as the horizontal axis and $M_{\rm dia}\times(\sqrt{Gi}/{h_{\rm R}}^2)^{1/3}$ instead of $M_{\rm dia}$ as the vertical axis. The curves in Fig. 2.13 show a crossing behavior in the field range $0.1 \lesssim h_{\rm R} \lesssim 0.5$. On the other hand, the curves in Fig. 2.14 show a crossing in $0.01 \lesssim h_{\rm R} \lesssim 0.5$. Therefore, in the BCS-BEC crossover regime, the field range where the crossing behavior appears is broad compared to that in the BCS regime.

These results of the LLL-scaling plot and the crossing behavior are summarized as follows: in an isotropic 3D system in the BCS regime, mainly the LLL modes ($N = 0$) of SCF create the crossing behavior only in a high field range ($0.1 \lesssim h_{\rm R} \lesssim 0.5$). On the other hand, in the BCS-BEC crossover regime with stronger SCF, the higher-LL modes ($N \geq 1$) of SCF in addition to the LLL modes create the crossing behavior in a broader field range ($0.01 \lesssim h_{\rm R} \lesssim 0.5$).

2.4 Discussion and summary

We discuss relevance of our results to the anomalous SCF-induced diamagnetic response observed in FeSe. First, our numerical result in the BCS-BEC crossover regime (Fig. 2.8) is qualitatively consistent with the large diamagnetic susceptibility observed in FeSe [6]. Second, the experimentally observed crossing behavior of magnetization curves [6] may also be explained based on our result in the BCS-BEC crossover regime (Fig. 2.14). Although we have tried to quantitatively fit our numerical results to the experimental data, no quantitative agreement has been obtained. This may be due to our neglect of the detailed band structure of FeSe in the present theory, which starts from an isotropic 3D continuum model. Regarding the zero-field temperature dependence of the specific heat, while our numerical results show the broad behavior in the BCS-BEC crossover regime (Fig. 2.6), experiments on FeSe show a relatively sharp jump at $T_{\rm c}$ [17, 18, 19] as mentioned in Sec. 1.2.2. It will be one of the origins of this inconsistency that an artifact of the Hartree-Fock approximation applied in this chapter is strongly reflected in the specific-heat behavior at the transition temperature $T_{\rm cR}$ (see the last paragraph of Sec. 2.2.5 and the fourth paragraph of Sec. 2.3.3). To treat the critical phenomena occurring around $T_{\rm cR}$ beyond the Hartree-Fock approximation, we may need a more sophisticated formulation, e.g., the renormalization group method, to consider the higher-order interactions between fluctuations. Another possible origin of the inconsistency is the fact that our starting model is too simple, and thus we should go beyond our simple continuum model and take into account the detailed band structure as explained in the following.

FeSe is considered to be a two-band system consisting of hole and electron bands, and these two bands are asymmetric. That is, roughly speaking, the hole and electron bands can be in the BCS and BCS-BEC crossover regimes, respectively [5]. In our previous work [73], we have studied the SCF-induced diamagnetic response in a symmetric two-band system in the BCS regime and shown that the diamagnetic susceptibility can become larger due to high-energy modes of SCF than that in a single-band system. This can naturally lead to an expectation that the diamagnetic susceptibility in a symmetric two-band system where both bands are in the BCS-BEC crossover regime is also enhanced compared with that in a single-band system in the BCS-BEC crossover regime as explored in this chapter. However, we cannot directly apply the scheme used in the previous study to a more general asymmetric two-band system such as FeSe since the gradient expansion in the GL action might not be justified [88] due to the difference in the coherence length between the two bands. Therefore, in considering a general two-band system to describe FeSe in detail, it would be better to treat the full momentum dependence of the SCF contribution by using a more microscopic method such as the self-consistent T-matrix approximation [30]. As for the specific-heat jump observed in FeSe, the sharp jump can be created dominantly by the weak-coupling band in the BCS regime, which may be investigated also in the self-consistent T-matrix

approximation.

According to very recent experiments [70], in the superconducting state of FeSe, one of the two superconducting gaps due to the two-band structure can vanish when the external magnetic field is sufficiently high ($\mu_0 H \gtrsim 0.5$T); therefore, FeSe can effectively behave as a single-band system when the field is high enough to satisfy $\mu_0 H \gtrsim 0.5$T, while the two-band nature can appear under low fields satisfying $\mu_0 H \lesssim 0.5$T. This speculation is seemingly consistent with the fact that our numerical results based on a single-band model are qualitatively consistent with the high-field diamagnetic response observed in FeSe [6], while they are inconsistent with the zero-field specific-heat jump observed in FeSe [17, 18, 19].

Before ending this chapter, we add some remarks. We have shown in our previous [73] and the present works that, as observed in the anisotropic 3D system FeSe with $\xi_{0,c} > s/\sqrt{2}$ (s is the interlayer spacing), appearance of the crossing behavior of the magnetization curves $M_{\rm dia}(T)$ over some field range is not limited to 2D-like systems such as a lot of high-$T_{\rm c}$ cuprates. Therefore, contrary to an argument given elsewhere [89], this crossing behavior has nothing to do with the dimensional crossover present in quasi-2D systems with $\xi_{0,c} < s/\sqrt{2}$.

In this chapter, we have studied SCF effects on thermodynamic properties in the BCS-BEC crossover regime by using a simple 3D electron model. As a consequence, we conclude that the following three features can emerge due to the strong mode coupling between SCF, which is characteristic of electron systems in the BCS-BEC crossover regime. First, the SCF-induced specific heat and diamagnetic susceptibility can seemingly exceed the corresponding values in the Gaussian approximation (Figs. 2.6 and 2.8). Second, the LLL scaling can break down (Figs. 2.10 and 2.12), which means that the higher-LL modes ($N \geq 1$) of SCF are important in addition to the LLL modes ($N = 0$). Third, the crossing behavior of magnetization curves can appear in a broad range of magnetic fields (Fig. 2.14), which is caused by both the LLL and higher-LL modes.

Chapter 3

Features of field-temperature phase diagram

3.1 Introduction to this chapter

As mentioned in Sec. 1.2, recent experiments have suggested that a strong attractive interaction can exist in FeSe and related superconductors [5, 7], which can pave the way for material realization of the BCS-BEC crossover. In contrast to the electrically neutral ultracold atoms, electrons in a superconductor are charged and thus naturally coupled with the gauge field of an external magnetic field. Therefore, FeSe and related materials can provide an opportunity to experimentally study unexplored effects of the magnetic gauge coupling on superconductors with strong attractive interaction. In fact, superconducting fluctuation effects on diamagnetic response observed in FeSe are unusually enhanced compared with those in conventional superconductors [6], which may be understood as caused by the strong attractive interaction [8] as explained in detail in Chapter 2. Recent NMR measurements have proposed that a pseudogap caused by the preformed-pair formation can exist [64]. According to this NMR measurement, the onset temperature of the pseudogap depends on the magnetic-field strength [64], which suggests that the pseudogap in FeSe should be related to superconductivity. Though properties of a single vortex [90, 91] and zero-temperature vortex formation in trapped Fermion gases [92] in the BCS-BEC crossover regime have been investigated, a theoretical understanding of the field-temperature (H-T) phase diagram with strong attractive interaction is still incomplete.

The H-T phase diagram of a superconductor with strong fluctuation has been thoroughly investigated in relation to high $T_{\rm c}$ cuprates [81, 93, 94] which are believed to belong to superconductors with high particle density. There, it has been clarified by developing the superconducting fluctuation theory [93, 95] that the so-called upper critical field $H_{\rm c2}(T)$ in the three-dimensional (3D) type-II superconductor is not a phase transition line but a crossover one separating the vortex-liquid region from the normal phase affected by a weak fluctuation

effect, and that, in clean 3D materials, the genuine superconducting ordering occurs as a weak first-order transition corresponding to the vortex-lattice melting [96]. The vortex-lattice melting curve $H_{\rm melt}(T)$ can alternatively be determined by examining the elastic energy of the mean-field vortex-lattice state and invoking the Lindemann criterion [94]. In the so-called lowest-Landau-level (LLL) approach to the GL theory, it is believed that $H_{\rm melt}(T)$ should be found as a consequence of the superconducting fluctuation. In fact, the fluctuation effect shows the scaling behavior of the form $T - T_{\rm c}(H) \sim (TH)^{2/3}$ [95], while the field dependence of the melting temperature also obeys this scaling behavior [97].

In this chapter, we theoretically investigate qualitative features of the H-T phase diagram of superconductors with strong attractive interaction. To obtain a qualitative picture, we start with a simple attractive Hubbard model. Using the T-matrix approximation combined with analysis of the Ginzburg-Landau action, we estimate three types of characteristic magnetic fields: the pair-formation field H^*, the vortex-liquid-formation field $H_{\rm c2}$, and the vortex-lattice-formation field $H_{\rm melt}$. The region between $H_{\rm c2}$ and $H_{\rm melt}$, as well as that between H^* and $H_{\rm melt}$, is found to become broader as the attractive interaction gets stronger. Based on this result, we conclude that a strong attractive interaction can stabilize both the vortex-liquid and the preformed-pair regions.

3.2 Preliminary analysis of zero-field phase diagram

To consider qualitative magnetic-field effects on electron systems with strong attractive interaction, we begin with a simple attractive Hubbard model on a simple cubic lattice:

$$H = -t \sum_{\langle i,j\rangle,\sigma} \left(c_{i\sigma}^\dagger c_{j\sigma} + c_{j\sigma}^\dagger c_{i\sigma} \right) - U \sum_i c_{i\uparrow}^\dagger c_{i\downarrow}^\dagger c_{i\downarrow} c_{i\uparrow}. \tag{3.2.1}$$

Here, $c_{i\sigma}^{(\dagger)}$ is the annihilation (creation) operator of an electron with spin σ at site i, and $\langle i,j\rangle$ means a nearest-neighbor pair of sites. There are two parameters in our model: the nearest-neighbor hopping amplitude $t(>0)$ and the onsite attractive interaction $U(>0)$. For simplicity, the magnetic-field term is introduced at the stage of analyzing our Ginzburg-Landau functional (see Secs. 3.3 and 3.6.2). Basically, this simplification, equivalent to the electronic semi-classical approximation, corresponds to neglecting the Landau quantization of electron kinetic energy. In the following, the lattice constant is set to unity.

3.2.1 Zero-field pair-formation and pair-condensation temperatures

As a preliminary step to explore magnetic-field effects, we estimate the zero-field pair-formation and pair-condensation temperatures. Though the results presented in this section is well-known [21], we show them for completeness. As shown in the following, the pair-formation temperature T^* is calculated within the mean-field approximation [26, 98],

and the pair-condensation temperature $T_{\rm c}$ is calculated within the T-matrix approximation [1, 28, 29, 30]. As explained in Sec. 1.1, the T-matrix approximation can take into account the shift of chemical potential due to superconducting fluctuation, which is important when the attractive interaction is strong, and in addtion the particle density is not so high [23].

To calculate T^*, we apply to Eq. (3.2.1) the mean-field approximation, or equivalently, combine the following two equations with each other: the condition for divergence of the uniform superconducting susceptibility [see Eq. (3.2.4) for its definition]

$$\chi_{\boldsymbol{0}}^{(\mathrm{SC})} = \infty, \tag{3.2.2}$$

and the particle-number conservation for non-interacting particles

$$n = \frac{2}{M} \sum_{\boldsymbol{k}} \frac{1}{\exp[(\epsilon_{\boldsymbol{k}} - \mu)/T] + 1}. \tag{3.2.3}$$

Here, we define several symbols: particle density (per site) n, chemical potential μ, temperature T, the total number of lattice sites $M = M_x M_y M_z$, the lattice momentum with the periodic boundary condition $k_\alpha = 2\pi n_\alpha / M_\alpha$ ($-M_\alpha/2 \le n_\alpha < M_\alpha/2$ with $n_\alpha \in \mathbb{Z}$), and the energy dispersion of non-interacting particles $\epsilon_{\boldsymbol{k}} = -2t(\cos k_x + \cos k_y + \cos k_z)$. The superconducting susceptibility with pair (or center-of-mass) momentum $\boldsymbol{q}$ is defined as

$$\chi_{\boldsymbol{q}}^{(\mathrm{SC})} = \frac{\chi_{\boldsymbol{q}}^{(0)}(0)}{1 - U\chi_{\boldsymbol{q}}^{(0)}(0)}, \tag{3.2.4}$$

where

$$\chi_{\boldsymbol{q}}^{(0)}(\mathrm{i}\omega_m) = \frac{T}{M} \sum_{\boldsymbol{k},n} G_{\boldsymbol{k}+\boldsymbol{q}}^{(0)}(\mathrm{i}\varepsilon_n + \mathrm{i}\omega_m) G_{-\boldsymbol{k}}^{(0)}(-\mathrm{i}\varepsilon_n). \tag{3.2.5}$$

Here, $\varepsilon_n = 2\pi(n + 1/2)T$ ($\omega_m = 2\pi m T$) is the Fermion (Boson) Matsubara frequency, and $G_{\boldsymbol{k}}^{(0)}(\mathrm{i}\varepsilon_n) = (\mathrm{i}\varepsilon_n - \epsilon_{\boldsymbol{k}} + \mu)^{-1}$ is the non-interacting Green's function.

As for $T_{\rm c}$, we apply the T-matrix approximation. This approximation combines the divergence of the susceptibility $\chi_{\boldsymbol{0}}^{(\mathrm{SC})} = \infty$, which is the same condition as defining T^*, with the particle-number conservation

$$n = \frac{2T}{M} \sum_{\boldsymbol{k},n} G_{\boldsymbol{k}}(\mathrm{i}\varepsilon_n) \mathrm{e}^{+\mathrm{i}\varepsilon_n 0}, \tag{3.2.6}$$

in which superconducting fluctuation effects are taken into account. Here, $G_{\boldsymbol{k}}(\mathrm{i}\varepsilon_n)$ is the interacting-particle Green's function, which is defined as

$$G_{\boldsymbol{k}}(\mathrm{i}\varepsilon_n)^{-1} = G_{\boldsymbol{k}}^{(0)}(\mathrm{i}\varepsilon_n)^{-1} - \Sigma_{\boldsymbol{k}}(\mathrm{i}\varepsilon_n), \tag{3.2.7}$$

and $\Sigma_{\boldsymbol{k}}(\mathrm{i}\varepsilon_n)$ is the self energy defined within the T-matrix approximation as

$$\Sigma_{\boldsymbol{k}}(\mathrm{i}\varepsilon_n) = -\frac{T}{M}\sum_{\boldsymbol{q},m} G^{(0)}_{\boldsymbol{q}-\boldsymbol{k}}(\mathrm{i}\omega_m - \mathrm{i}\varepsilon_n)\frac{U^2\chi^{(0)}_{\boldsymbol{q}}(\mathrm{i}\omega_m)}{1-U\chi^{(0)}_{\boldsymbol{q}}(\mathrm{i}\omega_m)}\mathrm{e}^{+\mathrm{i}(\omega_m-\varepsilon_n)0}. \tag{3.2.8}$$

Here, the temperature-independent Hartree shift

$$\Sigma^{(\mathrm{H})} = -U\frac{T}{M}\sum_{\boldsymbol{k},n} G_{\boldsymbol{k}}(\mathrm{i}\varepsilon_n)\mathrm{e}^{+\mathrm{i}\varepsilon_n 0} = -\frac{Un}{2}, \tag{3.2.9}$$

is already taken into account by properly choosing the origin of energy; therefore we do not explicitly consider $\Sigma^{(\mathrm{H})}$ [10, 30]. Regarding the diagrammatic representation of the T-matrix approximation, see Fig. 4.5.

To explain physical meanings of the definitions of T^* and T_c, it is convenient to consider the strong-coupling BEC limit (see also Sec. 1.1). In this strong-coupling limit ($U/t \to \infty$), we can show that $T^* \propto |\mu| \propto U \propto E_\mathrm{b}$, where E_b is the two-particle binding energy [10]; therefore, T^* can be interpreted as the pair-formation (or pair-breaking) temperature. As for T_c, in the same limit, we obtain an asymptotic formula $T_c \propto t^2/U$, which represents the BEC transition temperature of non-interacting Bosons (or preformed-pairs) with a nearest-neighbor hopping amplitude $t_\mathrm{B} \propto t^2/U$ [21]; accordingly, T_c can be understood as the pair-condensation temperature.

Figure 3.1 shows an interaction strength v.s. temperature phase diagram obtained from the equations listed above with the particle density fixed to $n = 0.2$. As seen from Fig. 3.1, the preformed-pair region becomes broader as the interaction gets stronger. In Fig. 3.1, we also show with a gray dotted line the threshold value $U = U_0 \simeq 8.14t$ for the formation of a two-particle bound state [10, 29, 35]. Note that the BCS-BEC crossover occurs close to U_0.

As shown in Fig. 3.2, the chemical potential μ is remarkably reduced when the attractive interaction U approaches U_0. When U is larger than U_0, μ tends to become lower than the band bottom.

In the following, we focus on systems where $U < U_0$ is satisfied so that the decrease in μ is not so large. More specifically, we consider two systems with different values of U: $U/t = 2.57$ and $U/t = 5.14$ (see the green and yellow dotted lines in Figs. 3.1 and 3.2).

3.3 Theoretical approach to orbital magnetic-field effects

To understand qualitative features of the H-T phase diagram, we estimate three kinds of magnetic field values: the pair-formation field H^*, the vortex-liquid-formation field $H_{\mathrm{c}2}$, and the vortex-lattice-formation field H_melt. In the following, the direction of magnetic field is fixed in parallel to the z axis, and we assume strongly type-II systems and neglect the

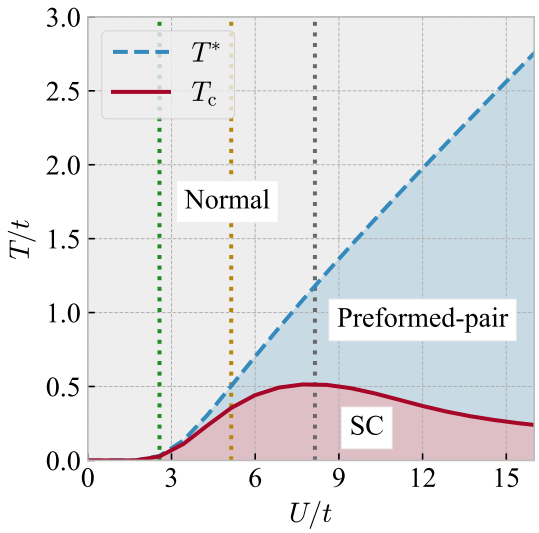

Figure 3.1: Interaction strength v.s. temperature phase diagram for the particle density $n = 0.2$ in zero field. The pair-formation temperature T^* (blue dashed line) roughly separates the normal-state region (gray area) from the preformed-pair region (blue area). The pair-condensation, or superconducting transition, temperature T_c (red solid line) separates the preformed-pair region from the superconducting (SC) region (red area). The threshold interaction value $U = U_0 \simeq 8.14t$ for the formation of a two-particle bound state (gray dotted line) and the values of interaction used in the analysis in Sec. 3.4, $U = 2.57t$ (green dotted line) and $5.14t$ (yellow dotted line), are also shown.

difference between the applied magnetic field and the magnetic field in the system ($\boldsymbol{B} = \mu_0 \boldsymbol{H}$). As mentioned in Sec. 3.2, we neglect the Landau quantization of the electron kinetic energy.

The pair-formation field H^* is calculated in a similar way to the calculation of T^*. To introduce the effect of magnetic field H, we only have to replace the condition for divergence of the uniform superconducting susceptibility [Eq. (3.2.2)] with that for divergence of a finite-momentum superconducting susceptibility [99]

$$\chi^{(\mathrm{SC})}_{\boldsymbol{q}_H} = \infty, \tag{3.3.1}$$

where ${q_H}^2 = \sqrt{2\pi\mu_0 H/\phi_0}$ and $\chi^{(\mathrm{SC})}_{\boldsymbol{q}}$ is given in Eq. (3.2.4). Here μ_0 is the vacuum permeability, and $\phi_0 = \pi\hbar/e$ is the flux quantum. $\chi^{(\mathrm{SC})}_{\boldsymbol{q}_H}$ approximately describes the susceptibility for states with the lowest-Landau-level index and uniform in the z direction. As for a free-particle number equation to determine the chemical potential, we adopt Eq. (3.2.3) since we neglect the Landau quantization of the electron kinetic energy. Therefore, we combine Eq. (3.3.1) with Eq. (3.2.3) to estimate H^*. The curve $(T, H^*(T))$ merges into $(T^*, 0)$ in the

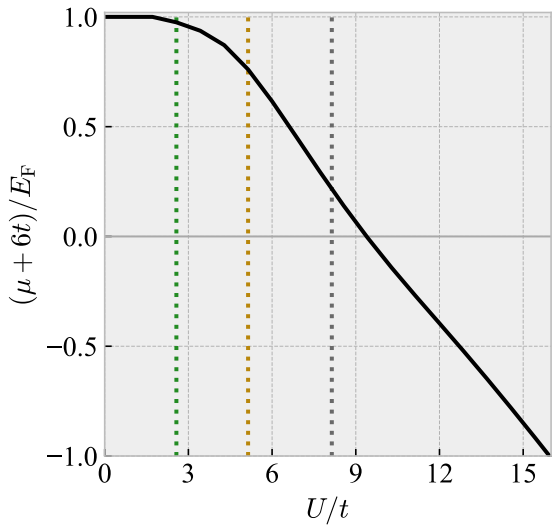

Figure 3.2: Chemical potential μ at the pair-condensation temperature $T_{\rm c}$ for the particle density $n = 0.2$. The vertical axis is measured from the bottom of the non-interacting energy band $-6t$ in units of the Fermi energy $E_{\rm F}$. In the same way as Fig. 3.1, the threshold value of interaction $U = U_0 \simeq 8.14t$ for the formation of a two-particle bound state (gray dotted line) and the values of interaction used in the analysis in Sec. 3.4, $U = 2.57t$ (green dotted line) and $5.14t$ (yellow dotted line), are also shown.

low-field limit; thus H^* can be regarded as a natural extension of T^* to the finite-field region.

The vortex-liquid formation field $H_{\rm c2}$ is estimated in a similar way to the calculation of $T_{\rm c}$. Since we focus on systems with $U < U_0$ (see the green and yellow dotted lines in Fig. 3.2), where the decrease in μ is not so large and the T dependence of μ is not so important, we simply approximate

$$\mu(T, H) \sim \mu(T_{\rm c}, 0), \tag{3.3.2}$$

where $\mu(T_{\rm c}, 0)$ is obtained within the T-matrix approximation (see Sec. 3.2.1 and Fig. 3.2). This approximation is correct at least in the weak-coupling limit, and we believe that this approximation is a first step to consider magnetic-field effects in the case with strong attractive interaction. After we replace $\mu(T, H)$ with $\mu(T_{\rm c}, 0)$, we solve Eq. (3.3.1) to estimate $H_{\rm c2}$. Similar to the case of H^*, the curve $(T, H_{\rm c2}(T))$ merges into $(T_{\rm c}, 0)$ in the low-field limit; thus $H_{\rm c2}$ can be understood as an extension of $T_{\rm c}$ to the finite-field region.

Regarding the vortex-lattice-formation field $H_{\rm melt}$, we apply an analysis based on the Ginzburg-Landau analysis [100, 101] in the lowest-Landau-level approximation [97, 102], which is valid closer to the $H_{\rm c2}$ line [69, 97, 103]. First, as explained in Sec. 3.6.1, we derive

the zero-field Ginzburg-Landau functional $\mathcal{F}_{\rm GL}$:

$$\mathcal{F}_{\rm GL} = \sum_{\boldsymbol{q}} T\left(1 - U\chi^{(0)}_{\boldsymbol{q}}(0)\right)|a_{\boldsymbol{q}}|^2 + \frac{\beta}{2}\sum_i |a_i|^4. \tag{3.3.3}$$

Here, $a_i = M^{-1/2}\sum_{\boldsymbol{q}} \exp(\mathrm{i}\boldsymbol{q}\cdot\boldsymbol{r}_i)a_{\boldsymbol{q}}$, and the coefficient β is given as

$$\beta = \frac{T^3U^2}{M}\sum_{\boldsymbol{k},n}\left|G^{(0)}_{\boldsymbol{k}}(\mathrm{i}\varepsilon_n)\right|^4. \tag{3.3.4}$$

As shown in Sec. 3.6.2, by applying the lowest-Landau-level approximation to Eq. (3.3.3) with replacement of the momentum in the x-y plane by $\boldsymbol{q}_H$ consistently with Eq. (3.3.1) and using the gradient expansion in the z direction, we obtain

$$\mathcal{F}_{\rm GL} \sim \int \mathrm{d}^3\boldsymbol{r}\left[\left(\alpha_{\boldsymbol{q}_H}|\psi(\boldsymbol{r})|^2 + \gamma|\partial_z\psi(\boldsymbol{r})|^2\right) + \frac{\beta}{2}|\psi(\boldsymbol{r})|^4\right], \tag{3.3.5}$$

where the order-parameter field $\psi(\boldsymbol{r})$ involves only the lowest-Landau-level modes in the x-y plane. The coefficients are given as follows:

$$\alpha_{\boldsymbol{q}_H} = T\left[1 - U\chi^{(0)}_{\boldsymbol{q}_H}(0)\right], \tag{3.3.6}$$

and

$$\gamma = -\frac{T^2Ut}{M}\sum_{\boldsymbol{k},n}\left[G^{(0)}_{\boldsymbol{k}}(\mathrm{i}\varepsilon_n)\right]^2 G^{(0)}_{-\boldsymbol{k}}(-\mathrm{i}\varepsilon_n)\left[\cos k_z + 4tG^{(0)}_{\boldsymbol{k}}(\mathrm{i}\varepsilon_n)\sin^2 k_z\right]^2. \tag{3.3.7}$$

As shown in Sec. 3.6.3, based on Eq. (3.3.5), the vortex-lattice-formation field $H_{\rm melt}$ is approximately calculated by solving the following equation:

$$\frac{T}{4\pi\sqrt{\rho_{\rm s}c_{66}}} = \frac{c^2}{h}. \tag{3.3.8}$$

Here, $h = 2\pi\mu_0 H/\phi_0$ is a dimensionless magnetic field (note that the lattice constant is set to unity), and $c = \mathcal{O}(10^{-1})$ is a phenomenological parameter [97]. Also, c_{66} and $\rho_{\rm s}$ represent the shear modulus of the vortex lattice and the superfluid density defined along the magnetic field, respectively (see Sec. 3.6.3):

$$c_{66} = \frac{2\gamma_{\rm A}|\alpha_{\boldsymbol{q}_H}|^2}{{\beta_{\rm A}}^2\beta}, \tag{3.3.9}$$

and

$$\rho_{\rm s} = \frac{2|\alpha_{\boldsymbol{q}_H}|\gamma}{\beta_{\rm A}\beta} \tag{3.3.10}$$

with numerical factors related to the triangular vortex-lattice structure: $\beta_{\rm A} \simeq 1.16$ and $\gamma_{\rm A} \simeq 0.119$. To obtain $H_{\rm melt}$, we solve Eq. (3.3.8) in combination with the approximated chemical potential [Eq. (3.3.2)].

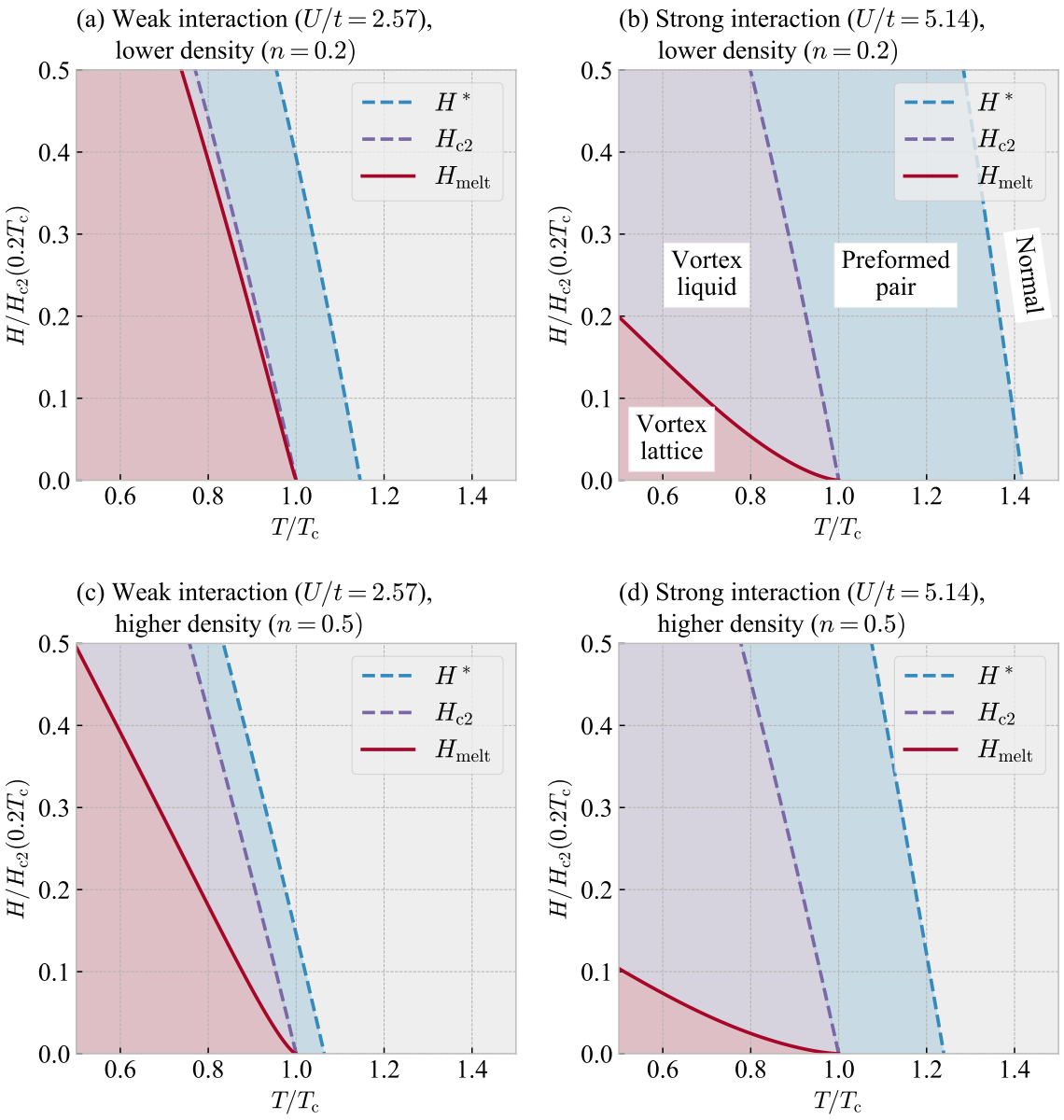

Figure 3.3: Field-temperature (H-T) phase diagrams. Figures (a) and (b) respectively show the weak-interaction ($U/t = 2.57$) and strong-interaction ($U/t = 5.14$) cases with lower density ($n = 0.2$). Figures (c) and (d) respectively show the weak-interaction ($U/t = 2.57$) and strong-interaction ($U/t = 5.14$) cases with higher density ($n = 0.5$). In each figure, the pair-formation field H^* (blue dashed line) separates the normal-state region (gray area) from the preformed-pair region (blue area), the vortex-liquid-formation field H_{c2} (purple dashed line) separates the preformed-pair region from the vortex-liquid region (purple area), and the vortex-lattice-formation field H_{melt} (red solid line) separates the vortex-liquid region from the vortex-lattice region (red area). In all data, the phenomenological parameter to describe H_{melt} is fixed as $c = 0.5$ (see the main text).

3.4 Field-temperature phase diagram

Based on numerically calculated H^*, H_{c2}, and H_{melt}, we obtain typical H-T phase diagrams (Fig. 3.3). Since our purpose is to investigate qualitative features of the H-T phase diagram, we fix the phenomenological parameter to estimate H_{melt} as $c = 0.5$ throughout our calculation. A slight change in c does not affect the qualitative features. Figures 3.3(a) and (b) respectively show the weak-interaction ($U/t = 2.57$) and strong-interaction ($U/t = 5.14$) cases with lower density ($n = 0.2$). Comparing Figs. 3.3(a) and (b), we can see that the vortex-liquid region between H_{c2} and H_{melt}, as well as the preformed-pair region between H_{c2} and H^*, becomes broader as the interaction becomes stronger; therefore, a strong attractive interaction stabilizes both the vortex-liquid and the preformed-pair regions.

Let us consider physical reasons why both the vortex-liquid and preformed-pair states are stabilized by a strong attractive interaction. First, the stabilization of the preformed-pair state can be understood in the same way as the zero-field case: a strong attractive interaction makes it easy to create non-condensed pairs, or preformed pairs [3]. Second, the stabilization of the vortex-liquid region can be understood based on the superconducting fluctuation strength: as the attractive interaction gets stronger toward the BCS-BEC crossover regime, the fluctuation becomes more significant [8, 66], and thus the vortex-liquid region becomes wider.

Figures 3.3(c) and (d) show the obtained phase diagrams with higher density ($n = 0.5$). Similar to the case with lower density ($n = 0.2$), we can see that both the vortex-liquid and the preformed-pair regions are stabilized when the interaction is strong. Moreover, comparing the higher density case [Figs. 3.3(a) and (b)] with the lower density case [Figs. 3.3(c) and (d)], we can see that the vortex-liquid region is broader while the preformed-pair region is narrower when the density is higher. From this result, we conclude that the particle density, in addition to interaction strength, is an important factor in determining the resultant H-T phase diagram.

Here, we point out that keeping only the LLL modes among various order parameter's spatial variations is an approach from the weak fluctuation in the following sense: it is clear that, in the weak-field limit, the LLL mode vanishes so that the fluctuation-induced downward shift of T_c in zero field, $\Delta T_c(0)$, cannot be described within the present approach. To describe $\Delta T_c(0)$, it is necessary to incorporate the higher-Landau-level (HLL) modes in our calculation. In fact, the HLL modes incorporating the vortex-loop fluctuations [81, 104] should lead to not only $\Delta T_c(0)$ and a shift of the $H_{c2}(T)$ line in low fields accompanying it but also a downward shift of $H_{melt}(T)$ and a change of its temperature dependence in low enough fields. Although such effects have been omitted in the present LLL approach, this simplification is not essential to our purpose here of understanding a qualitative picture of the H-T phase diagram in superconductors with a strong pairing interaction.

3.5 Discussion and summary

In this chapter, to obtain typical H-T phase diagrams in electron systems with strong attractive interaction, we estimate the pair-formation field H^*, the vortex-liquid-formation field H_{c2}, and the vortex-lattice-formation field H_{melt}. Based on numerical calculations, we find that a strong attractive interaction can stabilize both the vortex-liquid and the preformed-pair regions. In addition, we point out that the particle density also influences the resultant phase diagram.

In the preformed-pair and vortex-liquid regions stabilized by strong attractive interaction, thermodynamic and transport properties are expected to be characteristic. In particular, the Hall conductivity in the vortex-liquid region can be enhanced by superconducting fluctuation effects [105, 106] since the dynamics of the superconducting order parameter can involve a larger propagating part when the interaction is stronger [26].

In the end of this section, we discuss the H-T phase diagram in FeSe suggested by several experiments [5, 6, 64]. We do not comment on the high-field low-temperature phase ("B-phase") proposed in Ref. [5] since in our calculation we do not take into account the Zeeman coupling of magnetic field, which might be important in the high-field low-temperature region. Let us consider other aspects of FeSe. First, a large pseudogap region above H_{c2} in the H-T plane is suggested in Ref. [64]. If we assume that the pseudogap is caused by the preformed pair [1, 28], we can interpret the observed pseudogap region as the preformed-pair region stabilized by a strong attractive interaction as in Fig. 3.3(b). Second, a crossing of magnetization curves [68, 71] is observed in Ref. [6]. As explained in Chapter 2, this crossing can be understood as caused by a strong attractive interaction [8] in the vortex-liquid region. This vortex-liquid region can be understood as stabilized also by the strong attractive interaction. Third, the Hall, Seebeck, and Nernst coefficients have shown their maximum or minimum near a temperature $T \sim 2T_c$ with weak dependence on H [6]. Though a strong attractive interaction might be related to this behavior, the detailed electronic structure [5, 52, 107] should be taken into account to discuss such transport phenomena since FeSe is an almost compensated semimetal [5] and compensation of electron and hole carriers can make the sign of transport coefficients, such as the Hall coefficient, subtle.

In addition, we discuss the resistive vanishing in FeSe in finite fields. As stressed in the present work as well as Ref [10], a broad preformed-pair region is expected, as in Fig. 3.3(b), to lie above the nominal $H_{c2}(T)$ curve in FeSe. If so, the fact [5, 6] that the vortex-liquid region is relatively narrow in the experimental phase diagram of FeSe needs to be clarified. This discrepancy may be due to the fact that the resistivity vanishes at a much higher temperature than $H_{melt}(T)$ defined in clean limit. This possibility occurs when the resistivity vanishes through a vortex-glass transition due to the vortex pinnings to columnar defects or correlated defects [108, 109]. Another possibility is that the vortex-liquid region has estimated to be much narrower from the resistivity data than the actual one. This may occur when the

quantum fluctuation neglected in the present study is not negligible [110]. If this scenario is true, the resistivity is insensitive to the position of the actual H_{c2} and, upon cooling, begins to vanish close to a vortex-glass transition, which lies near $H_{\rm melt}$ and much below the actual H_{c2}.

As another possible scenario to explain why the vortex-liquid region is estimated to be relatively narrow in FeSe, let us consider the two-band structure characteristic of FeSe [5, 52, 107]. If a strong attractive interaction is present in one of these bands while a weak attractive interaction exists in another band, the vortices due to the former band can be pinned by the vortex lattice generated by the latter band. If this is true, the vortex-liquid region can become relatively narrow compared to the case considered in the present work where only a single band with strong attractive interaction exists. This possibility will be examined in details elsewhere.

3.6 Derivations of some formulas

3.6.1 Derivation of Ginzuburg-Landau functional

Here we derive the zero-field Ginzburg-Landau functional given by Eq. (3.3.3). By using the functional integral representation [26, 66, 72], we can formally rewrite the grand-canonical partition function Z as

$$Z = \int \left[\prod_{\boldsymbol{k},\sigma,n} \mathrm{d}c^*_{\boldsymbol{k}\sigma}(\varepsilon_n) \mathrm{d}c_{\boldsymbol{k}\sigma}(\varepsilon_n) \right] \mathrm{e}^{-(S_0+S_{\rm int})}, \tag{3.6.1}$$

where

$$S_0 = \frac{1}{T} \sum_{\boldsymbol{k},\sigma,n} \left[-G^{(0)}_{\boldsymbol{k}}(\mathrm{i}\varepsilon_n)^{-1} \right] c^*_{\boldsymbol{k}\sigma}(\varepsilon_n) c_{\boldsymbol{k}\sigma}(\varepsilon_n), \tag{3.6.2}$$

$$S_{\rm int} = -\frac{U}{TM} \sum_{\boldsymbol{q},m} \phi^*_{\boldsymbol{q}}(\omega_m) \phi_{\boldsymbol{q}}(\omega_m), \tag{3.6.3}$$

and

$$\phi_{\boldsymbol{q}}(\omega_m) = \sum_{\boldsymbol{k},n} c_{-\boldsymbol{k}\downarrow}(-\varepsilon_n) c_{\boldsymbol{k}+\boldsymbol{q}\uparrow}(\varepsilon_n + \omega_m). \tag{3.6.4}$$

Here, $c_{\boldsymbol{k}\sigma}(\varepsilon_n)$ and $c^*_{\boldsymbol{k}\sigma}(\varepsilon_n)$ are the Grassmann numbers, and $G^{(0)}_{\boldsymbol{k}}(\mathrm{i}\varepsilon_n) = (\mathrm{i}\varepsilon_n - \epsilon_{\boldsymbol{k}} + \mu)^{-1}$ is the non-interacting Green's function.

Introducing the order-parameter field $a_{\boldsymbol{q}}(\omega_m)$ and $a^*_{\boldsymbol{q}}(\omega_m)$ with the Hubbard-Stratonovich transformation, we can obtain the following expression:

$$\mathrm{e}^{-S_{\rm int}} = \int \left[\prod_{\boldsymbol{q},m} \frac{\mathrm{d}a^*_{\boldsymbol{q}}(\omega_m) \mathrm{d}a_{\boldsymbol{q}}(\omega_m)}{\pi} \right] \mathrm{e}^{-\sum_{\boldsymbol{q},m} |a_{\boldsymbol{q}}(\omega_m)|^2} \mathrm{e}^{\sqrt{U/(TM)} \sum_{\boldsymbol{q},m} [a^*_{\boldsymbol{q}}(\omega_m) \phi_{\boldsymbol{q}}(\omega_m) + \mathrm{c.c.}]}. \tag{3.6.5}$$

Using this expression, we can transform the partition function as

$$\begin{aligned}\frac{Z}{Z_0} =& \langle \mathrm{e}^{-S_{\mathrm{int}}} \rangle_0 \\ =& \int \left[\prod_{\boldsymbol{q},m} \frac{\mathrm{d}a^*_{\boldsymbol{q}}(\omega_m)\mathrm{d}a_{\boldsymbol{q}}(\omega_m)}{\pi} \right] \mathrm{e}^{-\sum_{\boldsymbol{q},m}|a_{\boldsymbol{q}}(\omega_m)|^2} \left\langle \mathrm{e}^{\sqrt{U/(TM)}\sum_{\boldsymbol{q},m}[a^*_{\boldsymbol{q}}(\omega_m)\phi_{\boldsymbol{q}}(\omega_m)+\mathrm{c.c.}]} \right\rangle_0 . \end{aligned} \tag{3.6.6}$$

Here, $Z_0 = \int [\prod_{\boldsymbol{k},\sigma,n} \mathrm{d}c^*_{\boldsymbol{k}\sigma}(\varepsilon_n)\mathrm{d}c_{\boldsymbol{k}\sigma}(\varepsilon_n)]\mathrm{e}^{-S_0}$ is the non-interacting partition function, and $\langle \cdots \rangle_0$ represents the grand-canonical ensemble average with respect to the non-interacting part S_0. Expanding the last term in Eq. (3.6.6) with respect to the order-parameter field $a_{\boldsymbol{q}}(\omega_m)$ and $a^*_{\boldsymbol{q}}(\omega_m)$ up to the fourth order and neglecting Bosonic quantum fluctuation, we can finally obtain the following form:

$$\frac{Z}{Z_0} \sim \int \left[\prod_{\boldsymbol{q}} \frac{\mathrm{d}a^*_{\boldsymbol{q}}\mathrm{d}a_{\boldsymbol{q}}}{\pi} \right] \mathrm{e}^{-\mathcal{F}_{\mathrm{GL}}/\mathrm{T}}, \tag{3.6.7}$$

where we write $a_{\boldsymbol{q}} = a_{\boldsymbol{q}}(0)$ for simplicity. Here, $\mathcal{F}_{\mathrm{GL}}$ is the Ginzburg-Landau functional, the explicit form of which is given as

$$\mathcal{F}_{\mathrm{GL}} = \sum_{\boldsymbol{q}} T \left[1 - U\chi^{(0)}_{\boldsymbol{q}}(0) \right] |a_{\boldsymbol{q}}|^2 + \frac{\beta}{2} \sum_i |a_i|^4, \tag{3.6.8}$$

where $a_i = M^{-1/2} \sum_{\boldsymbol{q}} \exp(\mathrm{i}\boldsymbol{q} \cdot \boldsymbol{r}_i) a_{\boldsymbol{q}}$ is the real-space order-parameter field,

$$\chi^{(0)}_{\boldsymbol{q}}(\mathrm{i}\omega_m) = \frac{T}{M} \sum_{\boldsymbol{k},n} G^{(0)}_{\boldsymbol{k}+\boldsymbol{q}}(\mathrm{i}\varepsilon_n + \mathrm{i}\omega_m) G^{(0)}_{-\boldsymbol{k}}(-\mathrm{i}\varepsilon_n), \tag{3.6.9}$$

and

$$\beta = \frac{T^3 U^2}{M} \sum_{\boldsymbol{k},n} \left| G^{(0)}_{\boldsymbol{k}}(\mathrm{i}\varepsilon_n) \right|^4 . \tag{3.6.10}$$

3.6.2 Lowest-Landau-level approximation of Ginzburg-Landau action

In the following, we explain how we obtain the approximated expression of the Ginzburg-Landau functional [Eq. (3.3.5)]. Neglecting the Landau quantization of electrons, the external magnetic field affects the energy eigenstate of the order-parameter field a_i. At large length scales, the lattice structure is not important so that we can focus on the long-wavelength parts of a_i and can replace a_i defined on lattice with $\psi(\boldsymbol{r})$ defined in continuum space (note that the lattice constant is set to unity). Then, to perform our calculation in a finite magnetic field parallel to the z axis, we can rewrite Eq. (3.3.3) as

$$\mathcal{F}_{\mathrm{GL}} \simeq \int \mathrm{d}^3\boldsymbol{r} \left(\psi^* \alpha_{\boldsymbol{Q}} \psi + \gamma |\partial_z \psi|^2 + \frac{\beta}{2} |\psi|^4 \right), \tag{3.6.11}$$

where

$$\alpha_{\boldsymbol{Q}} = T\left[1 - U\chi^{(0)}_{\boldsymbol{Q}}(0)\right] \tag{3.6.12}$$

with $\boldsymbol{Q} = -\mathrm{i}\nabla_\perp + 2\pi\boldsymbol{A}/\phi_0$ is the gauge-invariant gradient in the directions perpendicular to the field, and

$$\gamma = -\frac{T^2Ut}{M}\sum_{\boldsymbol{k},n}\left[G^{(0)}_{\boldsymbol{k}}(\mathrm{i}\varepsilon_n)\right]^2 G^{(0)}_{-\boldsymbol{k}}(-\mathrm{i}\varepsilon_n)\left[\cos k_z + 4tG^{(0)}_{\boldsymbol{k}}(\mathrm{i}\varepsilon_n)\sin^2 k_z\right]^2. \tag{3.6.13}$$

Here we introduce magnetic-field effects through a minimal coupling of the vector potential $\boldsymbol{A}(\boldsymbol{r})$ to the order-parameter field $\psi(\boldsymbol{r})$.

To diagonalize the second-order terms of Eq. (3.6.11), we expand the order-parameter field as

$$\psi(\boldsymbol{r}) = \sum_{N,n_\mathrm{d},q_z} b_{Nn_\mathrm{d}q_z} f_{Nn_\mathrm{d}}(x,y)\frac{\mathrm{e}^{\mathrm{i}q_z z}}{\sqrt{L_z}}, \tag{3.6.14}$$

where N is the Landau-level index, n_d is the degeneracy index for each Landau level with $(\mu_0 H L_x L_y/\phi_0)$-fold degeneracy, q_z is the z-directional momentum, and $f_{Nn_\mathrm{d}}(x,y)$ is the Nth Landau-level eigenfunction [note that the lattice constant is unity so that $L_i = M_i$ $(i = x,y,z)$]. Though, in general, it is not clear whether the second-order terms of Eq. (3.6.11) are diagonalized with the bases appearing in Eq. (3.6.14), at least the lowest-order Q^2 terms are exactly diagonalized with these bases. Respecting this fact and substituting Eq. (3.6.14) into Eq. (3.6.11), we obtain the diagonalized second-order terms:

$$\mathcal{F}_\mathrm{GL} \simeq \sum_{N,n_\mathrm{d},q_z}\left(\alpha_{\sqrt{2N+1}\boldsymbol{q}_H} + \gamma {q_z}^2\right)|b_{Nn_\mathrm{d}q_z}|^2 + \int \mathrm{d}^3\boldsymbol{r}\frac{\beta}{2}|\psi|^4, \tag{3.6.15}$$

where ${q_H}^2 = l^{-1} = \sqrt{2\pi\mu_0 H/\phi_0}$. Therefore, through the Landau quantization of the order-parameter field, we basically replace squared gauge-invariant gradient Q^2 defined in the x-y plane with discrete levels $(2N+1)/l^2$.

As far as we focus our attention on the region relatively near $H_{\mathrm{c}2}(T)$, we just take into account the contribution from the lowest Landau-level mode [69, 81, 97, 103]; then we can obtain from Eq. (3.6.15) the following expression:

$$\mathcal{F}_\mathrm{GL} \simeq \sum_{n_\mathrm{d},q_z}\left(\alpha_{\boldsymbol{q}_H} + \gamma {q_z}^2\right)|b_{0n_\mathrm{d}q_z}|^2 + \int \mathrm{d}^3\boldsymbol{r}\frac{\beta}{2}|\psi|^4. \tag{3.6.16}$$

Conversely using the expansion of the order-parameter field [Eq. (3.6.14)] as well as considering only $N = 0$ mode, we finally obtain

$$\mathcal{F}_\mathrm{GL} \simeq \int \mathrm{d}^3\boldsymbol{r}\left[\left(\alpha_{\boldsymbol{q}_H}|\psi|^2 + \gamma|\partial_z\psi|^2\right) + \frac{\beta}{2}|\psi|^4\right], \tag{3.6.17}$$

where $\psi(\boldsymbol{r})$ only involves the lowest Landau-level mode $(N = 0)$.

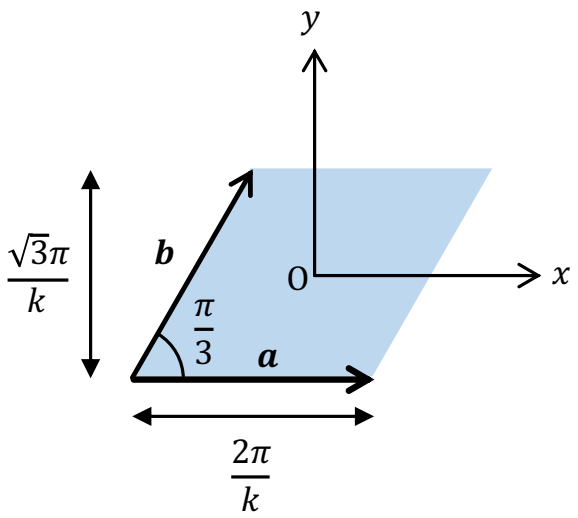

Figure 3.4: Schematic figure of a unit cell of the triangular vortex lattice (blue area). Primitive lattice vectors ($\boldsymbol{a}$ and $\boldsymbol{b}$) as well as the size of the unit cell are shown. Note that one quantum flux penetrates one unit cell [$(\sqrt{3}\pi/k)\cdot(2\pi/k) = 2\pi l^2 = \phi_0/(\mu_0 H)$].

3.6.3 Derivation of vortex-lattice-formation field

In the following, we explain how we estimate the vortex-lattice-formation field $H_{\rm melt}$ and obtain Eq. (3.3.8) starting with Eq. (3.3.5). Since the mean-field solution minimizing Eq. (3.3.5) is given by the triangular vortex-lattice state, we consider the Gaussian fluctuation around the triangular vortex-lattice state [100, 101] within the lowest-Landau-level approximation [97, 102] and then apply the Lindemann criterion to estimate $H_{\rm melt}$ [97], at which the first-order melting transition to the vortex-liquid state occurs. Since our formulation is basically based on Refs. [97, 102], we here just present an overview. In the following, we assume the Landau gauge $\boldsymbol{A}(\boldsymbol{r}) = -\mu_0 H y\widehat{x}$. In this subsection, $\boldsymbol{r}$ denotes a coordinate vector $x\widehat{x} + y\widehat{y}$ in the x-y plane.

As a complete orthonormal set of bases diagonalizing the second-order terms of Eq. (3.3.5), we consider a set of triangular vortex-lattice states with z-directional modulation:

$$\left\{\varphi(\boldsymbol{r}|\boldsymbol{r}_0)\frac{e^{iq_z z}}{\sqrt{L_z}}\right\}_{\boldsymbol{r}_0,q_z}, \tag{3.6.18}$$

where $\{\varphi(\boldsymbol{r}|\boldsymbol{r}_0)\}$ represents a two-dimensional triangular vortex lattice with a unit cell shown in Fig. 3.4, and the position of the vortices is related to $\boldsymbol{r}_0$:

$$\boldsymbol{r}_0 = x_0\widehat{x} + y_0\widehat{y} = \left(\frac{2\pi l^2}{L_y}n_x + \frac{2\pi l^2}{\sqrt{3}L_x}n_y\right)\widehat{x} + \frac{2\pi l^2}{L_x}n_y\widehat{y}. \tag{3.6.19}$$

Here $l = \sqrt{\phi_0/(2\pi\mu_0 H)}$ is the magnetic length. The degeneracy indices of the lowest Landau level, n_x and n_y, satisfy

$$n_x \in \left[-\frac{L_y}{2kl^2},\ \frac{L_y}{2kl^2}\right),\quad n_y \in \left[-\frac{\sqrt{3}L_x}{4kl^2},\ \frac{\sqrt{3}L_x}{4kl^2}\right) \tag{3.6.20}$$

with $k = \sqrt{\sqrt{3}\pi}/l$. We note that the degeneracy of the lowest Landau level can be calculated as $[L_y/(kl^2)] \cdot [\sqrt{3}L_y/(2kl^2)] = L_x L_y/(2\pi l^2) = \mu_0 H L_x L_y/\phi_0$. The domain of $\boldsymbol{r}_0$ is equivalent to the unit cell shown in Fig. 3.4. As shown in the following, functions $\{\varphi(\boldsymbol{r}|\boldsymbol{r}_0)\}_{\boldsymbol{r}_0}$ with $\boldsymbol{r}_0$ out of the unit cell are linearly dependent on those with $\boldsymbol{r}_0$ within the unit cell.

The specific form of the eigenfunctions $\{\varphi(\boldsymbol{r}|\boldsymbol{r}_0)\}$ is given as

$$\varphi(\boldsymbol{r}|\boldsymbol{r}_0) = \mathrm{e}^{-\mathrm{i}y_0 x/l^2}\varphi(\boldsymbol{r}+\boldsymbol{r}_0|\boldsymbol{0}), \tag{3.6.21}$$

and

$$\varphi(\boldsymbol{r}|\boldsymbol{0}) = \frac{3^{1/8}}{\sqrt{L_x L_y}} \sum_{n=-\infty}^{\infty} \mathrm{e}^{\mathrm{i}knx - \mathrm{i}\pi n^2/2 - (y-kl^2 n)^2/(2l^2)}. \tag{3.6.22}$$

Defining primitive lattice vectors $\boldsymbol{a} = (2\pi/k)\widehat{x}$ and $\boldsymbol{b} = (\pi/k)\widehat{x} + (\sqrt{3}\pi/k)\widehat{y}$ as shown in Fig. 3.4, we obtain from Eq. (3.6.22) the following (quasi)periodicity of $\varphi(\boldsymbol{r}|\boldsymbol{0})$:

$$\begin{cases} \varphi(\boldsymbol{r}+\boldsymbol{a}|\boldsymbol{0}) = \varphi(\boldsymbol{r}|\boldsymbol{0}) \\ \varphi(\boldsymbol{r}+\boldsymbol{b}|\boldsymbol{0}) = \mathrm{i}\mathrm{e}^{\mathrm{i}kx}\varphi(\boldsymbol{r}|\boldsymbol{0}), \end{cases} \tag{3.6.23}$$

As for a general lattice vector $\boldsymbol{R} = m_a\boldsymbol{a} + m_b\boldsymbol{b}$, we can show from Eq. (3.6.23) the following quasiperiodicity:

$$\varphi(\boldsymbol{r}+\boldsymbol{R}|\boldsymbol{0}) = \mathrm{e}^{\mathrm{i}(\pi {m_b}^2/2 + m_b kx)}\varphi(\boldsymbol{r}|\boldsymbol{0}). \tag{3.6.24}$$

Combining Eqs. (3.6.21) and (3.6.24), we can obtain

$$\varphi(\boldsymbol{r}|\boldsymbol{r}_0+\boldsymbol{R}) = \mathrm{e}^{\mathrm{i}(\pi {m_b}^2/2 + m_b kx_0)}\varphi(\boldsymbol{r}|\boldsymbol{r}_0), \tag{3.6.25}$$

which shows that $\varphi(\boldsymbol{r}|\boldsymbol{r}_0)$ and $\varphi(\boldsymbol{r}|\boldsymbol{r}_0+\boldsymbol{R})$ are not independent; therefore, we only have to consider a set $\{\varphi(\boldsymbol{r}|\boldsymbol{r}_0)\}_{\boldsymbol{r}_0}$ where $\boldsymbol{r}_0$ is in a unit cell of the vortex lattice. Moreover, Eqs. (3.6.22) and (3.6.21) lead to the following orthonormal relation:

$$\int_S \mathrm{d}^2\boldsymbol{r}\,\varphi^*(\boldsymbol{r}|\boldsymbol{r}_0)\varphi(\boldsymbol{r}|\boldsymbol{r}_0') = \delta_{\boldsymbol{r}_0,\boldsymbol{r}_0'}, \tag{3.6.26}$$

where S means the entire x-y plane.

From Eqs. (3.6.21) and (3.6.24), we can show another relation:

$$\varphi(\boldsymbol{r}+\boldsymbol{R}|\boldsymbol{r}_0) = \mathrm{e}^{\mathrm{i}[\pi {m_b}^2/2 + m_b kx - (\boldsymbol{r}_0\times\widehat{z})\cdot\boldsymbol{R}/l^2]}\varphi(\boldsymbol{r}|\boldsymbol{r}_0). \tag{3.6.27}$$

Defining a momentum vector corresponding to $\boldsymbol{r}_0$ as

$$\boldsymbol{k}_0 = -\frac{\boldsymbol{r}_0 \times \widehat{z}}{l^2} \ \left(\Leftrightarrow \ \boldsymbol{r}_0 = l^2 \boldsymbol{k}_0 \times \widehat{z}\right), \tag{3.6.28}$$

we can rewrite Eq. (3.6.27) as

$$\varphi(\boldsymbol{r} + \boldsymbol{R}|\boldsymbol{r}_0) = \mathrm{e}^{\mathrm{i}(\pi {m_b}^2/2 + m_b k x + \boldsymbol{k}_0 \cdot \boldsymbol{R})} \varphi(\boldsymbol{r}|\boldsymbol{r}_0). \tag{3.6.29}$$

Combination of Eqs. (3.6.24) with (3.6.27) leads to

$$\varphi^*(\boldsymbol{r} + \boldsymbol{R}|\boldsymbol{0}) \varphi(\boldsymbol{r} + \boldsymbol{R}|\boldsymbol{r}_0) = \mathrm{e}^{\mathrm{i}\boldsymbol{k}_0 \cdot \boldsymbol{R}} \varphi^*(\boldsymbol{r}|\boldsymbol{0}) \varphi(\boldsymbol{r}|\boldsymbol{r}_0), \tag{3.6.30}$$

which means that $\varphi^*(\boldsymbol{r}|\boldsymbol{0})\varphi(\boldsymbol{r}|\boldsymbol{r}_0)$ is a Bloch function with a lattice momentum vector $\boldsymbol{k}_0$; therefore, we can expand this function as [100, 101]

$$\varphi^*(\boldsymbol{r}|\boldsymbol{0}) \varphi(\boldsymbol{r}|\boldsymbol{r}_0) = \frac{1}{L_x L_y} \sum_{\boldsymbol{K}} \mathrm{e}^{\mathrm{i}(\boldsymbol{k}_0 + \boldsymbol{K}) \cdot \boldsymbol{r}} F_{\boldsymbol{K}}(\boldsymbol{k}_0), \tag{3.6.31}$$

where $\boldsymbol{K}$ is a reciprocal lattice vector, which can be written with a certain lattice vector $\boldsymbol{R} = m_a \boldsymbol{a} + m_b \boldsymbol{b}$, as

$$\boldsymbol{K} = -\frac{\boldsymbol{R} \times \widehat{z}}{l^2}. \tag{3.6.32}$$

Applying the Fourier transformation to Eq. (3.6.31), we obtain

$$F_{\boldsymbol{K}}(\boldsymbol{k}_0) = \int_S \mathrm{d}^2 \boldsymbol{r} \, \mathrm{e}^{-\mathrm{i}(\boldsymbol{k}_0 + \boldsymbol{K}) \cdot \boldsymbol{r}} \varphi^*(\boldsymbol{r}|\boldsymbol{0}) \varphi(\boldsymbol{r}|\boldsymbol{r}_0). \tag{3.6.33}$$

Using the definition of $\varphi(\boldsymbol{r}|\boldsymbol{r}_0)$ [Eqs. (3.6.21) and (3.6.22)] in Eq. (3.6.33), we can derive the specific form of $F_{\boldsymbol{K}}(\boldsymbol{k}_0)$,

$$F_{\boldsymbol{K}}(\boldsymbol{k}_0) = \exp\left\{ l^2 \left[-\frac{(\boldsymbol{K} + \boldsymbol{k}_0)^2}{4} - \frac{\mathrm{i}}{2} \left(\frac{{K_x}^2}{\sqrt{3}} + K_x K_y + k_{0,x} k_{0,y} - (\boldsymbol{K} \times \boldsymbol{k}_0)_z \right) \right] \right\} \tag{3.6.34}$$

Let us divide the order-parameter field $\psi(\boldsymbol{r}, z)$ (note that in this subsection $\boldsymbol{r}$ represents a coordinate vector in the x-y plane) into the mean-field vortex-lattice state $\varphi(\boldsymbol{r}|\boldsymbol{0})/\sqrt{L_z}$ and the fluctuation around it:

$$\psi(\boldsymbol{r}, z) = \overline{a} \varphi(\boldsymbol{r}|\boldsymbol{0}) \frac{1}{\sqrt{L_z}} + \sum_{\boldsymbol{k}_0, q_z} a_{\boldsymbol{k}_0 q_z} \varphi(\boldsymbol{r}|\boldsymbol{r}_0) \frac{\mathrm{e}^{\mathrm{i} q_z z}}{\sqrt{L_z}}. \tag{3.6.35}$$

Here we choose the vortex-lattice state with $\boldsymbol{r}_0 = \boldsymbol{0}$ as a spontaneously translational-symmetry broken state. Also, $\overline{a}$ and $a_{\boldsymbol{k}_0 q_z}$ represent the mean-field and fluctuation amplitudes, respectively.

The mean-field amplitude $\overline{a}$ is determined by minimizing the Ginzburg-Landau functional $\mathcal{F}_{\rm GL}$ [Eq. (3.3.5)], leading to the following expression:

$$\overline{a} = \sqrt{L_x L_y L_z \frac{|\alpha_{\boldsymbol{q}_H}|}{\beta_{\rm A}\beta}}, \tag{3.6.36}$$

where we assume that $\alpha_{\boldsymbol{q}_H} < 0$, or $H < H_{c2}(T)$, so that the mean-field approximation leads to the vortex-lattice solution. Here we choose the vortex-lattice state with $\arg(\overline{a}) = 0$ as a spontaneously $U(1)$-symmetry broken state. Here $\beta_{\rm A}$ is the Abrikosov factor, which characterizes the triangular lattice structure: $\beta_{\rm A} = \langle|\varphi(\boldsymbol{r}|\boldsymbol{0})|^4\rangle_S / [\langle|\varphi(\boldsymbol{r}|\boldsymbol{0})|^2\rangle_S]^2$, with a spatial average in the x-y plane $\langle\cdots\rangle_S = (L_x L_y)^{-1}\int_S \mathrm{d}^2\boldsymbol{r}(\cdots)$.

Using the expanded form of the order-parameter field [Eq. (3.6.35)] in the Ginzburg-Landau functional [Eq. (3.3.5)] and diagonalizing the Gaussian-fluctuation (second-order with respect to $\{a_{\boldsymbol{r}_0 q_z}\}$) terms, we obtain

$$\mathcal{F}_{\rm GL} = \mathcal{F}_{\rm GL}^{\rm MF} + \mathcal{F}_{\rm GL}^{\rm Gauss} + \mathcal{F}_{\rm GL}^{\rm nonGauss}, \tag{3.6.37}$$

where

$$\mathcal{F}_{\rm GL}^{\rm MF} = -L_x L_y L_z \frac{|\alpha_{\boldsymbol{q}_H}|^2}{2\beta_{\rm A}\beta}, \tag{3.6.38}$$

$$\mathcal{F}_{\rm GL}^{\rm Gauss} = \sum_{\boldsymbol{k}_0, q_z > 0, m=\pm} \left(E_{\boldsymbol{k}_0}^{(m)} + \gamma {q_z}^2\right) \left|a_{\boldsymbol{k}_0 q_z}^{(m)}\right|^2, \tag{3.6.39}$$

and $\mathcal{F}_{\rm GL}^{\rm nonGauss}$ involves other terms corresponding to non-Gaussian fluctuation. In the following, we neglect the non-Gaussian fluctuation $\mathcal{F}_{\rm GL}^{\rm nonGauss}$ and concentrate on the Gaussian fluctuation $\mathcal{F}_{\rm GL}^{\rm Gauss}$. The fluctuation amplitude $a_{\boldsymbol{k}_0 q_z}^{(m)}$ is defined as

$$a_{\boldsymbol{k}_0 q_z}^{(\pm)} = \frac{1}{\sqrt{2}}\left(a_{\boldsymbol{k}_0 q_z} \pm a_{-\boldsymbol{k}_0, -q_z}\right), \tag{3.6.40}$$

and the fluctuation energy of each mode $E_{\boldsymbol{r}_0}^{(m)}$ is obtained as

$$E_{\boldsymbol{k}_0}^{(\pm)} = \frac{|\alpha_{\boldsymbol{q}_H}|}{\beta_{\rm A}} \left[2\sum_{\boldsymbol{K}} |F_{\boldsymbol{K}}(\boldsymbol{k}_0)|^2 - \sum_{\boldsymbol{K}} |F_{\boldsymbol{K}}(\boldsymbol{0})|^2 \pm \left|\sum_{\boldsymbol{K}} F_{\boldsymbol{K}}(\boldsymbol{k}_0)^2\right|\right], \tag{3.6.41}$$

where $F_{\boldsymbol{K}}(\boldsymbol{k}_0)$ is given in Eq. (3.6.34). We can show that $F_{\boldsymbol{K}}(\boldsymbol{0}) \in \mathbb{R}$, so that $E_{\boldsymbol{0}}^{(-)} = 0$, which shows that the fluctuation mode represented as $a_{\boldsymbol{k}_0 q_z}^{(-)}$ is massless (corresponding to the incompressible shear mode of the vortex lattice [97, 100]). Since the massless mode is expected to be dominant in considering the melting transition [97], we take into account the contribution of the massless mode $a_{\boldsymbol{k}_0 q_z}^{(-)}$ and neglect that of the massive mode $a_{\boldsymbol{k}_0 q_z}^{(+)}$. Moreover, to consider the long-wavelength and low-energy contribution of the massless mode, we expand the fluctuation energy $E_{\boldsymbol{k}_0}^{(-)}$ with respect to $\boldsymbol{k}_0$:

$$E_{\boldsymbol{k}_0}^{(-)} = \frac{\gamma_{\rm A}|\alpha_{\boldsymbol{q}_H}|}{\beta_{\rm A}} l^4 {k_0}^4 + \mathcal{O}({k_0}^6). \tag{3.6.42}$$

Here $\gamma_{\rm A}$ is a numerical factor related to the triangular-lattice structure:

$$\gamma_{\rm A} = \sum_{\boldsymbol{K}} \mathrm{e}^{-l^2K^2/2} \left\{ \frac{1}{12} \left[\frac{3}{8} l^4 K^4 - 3l^2K^2 + 3 \right] - \frac{1}{8} \right\} \simeq 0.119. \tag{3.6.43}$$

To derive Eq. (3.6.42), we use the following properties with an arbitrary function $f(K) = f(|\boldsymbol{K}|)$ due to a six-fold rotational symmetry of the reciprocal lattice space:

$$\begin{cases} \sum_{\boldsymbol{K}} (\boldsymbol{K} \cdot \boldsymbol{k}_0)^2 f(K) = \sum_{\boldsymbol{K}} \frac{1}{2} K^2 {k_0}^2 \\ \sum_{\boldsymbol{K}} (\boldsymbol{K} \cdot \boldsymbol{k}_0)^4 f(K) = \sum_{\boldsymbol{K}} \frac{3}{8} K^4 {k_0}^4. \end{cases} \tag{3.6.44}$$

In the following, therefore, we focus on the following functional:

$$\mathcal{F}_{\rm GL}^{\rm Gauss(-)} = \sum_{\boldsymbol{k}_0, q_z > 0} \left(\frac{\gamma_{\rm A} |\alpha_{\boldsymbol{q}_H}|}{\beta_{\rm A}} l^4 {k_0}^4 + \gamma {q_z}^2 \right) \left| a^{(-)}_{\boldsymbol{k}_0 q_z} \right|^2. \tag{3.6.45}$$

It has been proved [100, 101] that this form of the dispersion relation of the massless mode of the vortex lattice in type-II limit remains valid when the higher Landau-level modes ($N \geq 1$) are included.

Since the relative fluctuation $2^{-1/2} a^{(-)}_{\boldsymbol{k}_0 q_z} / |\overline{a}|$ can be regarded as an angular change of the vortex lattice $\theta_{\boldsymbol{k}_0 q_z}$ [97], we can rewrite $\mathcal{F}_{\rm GL}^{\rm Gauss(-)}$ [Eq. (3.6.45)] as

$$\begin{aligned} \mathcal{F}_{\rm GL}^{\rm Gauss(-)} &= L_x L_y L_z \sum_{\boldsymbol{k}_0, q_z > 0} \left(c_{66} l^4 {k_0}^4 + \rho_{\rm s} {q_z}^2 \right) |\theta_{\boldsymbol{k}_0 q_z}|^2 \\ &= \frac{1}{2} \int_S \mathrm{d}^2 \boldsymbol{r} \int_0^{L_z} \mathrm{d}z \, \left[c_{66} l^4 (\nabla_\perp {}^2 \theta)^2 + \rho_{\rm s} (\partial_z \theta)^2 \right]. \end{aligned} \tag{3.6.46}$$

Here, $\theta(\boldsymbol{r}, z) = \sum_{\boldsymbol{k}_0, q_z} \mathrm{e}^{\mathrm{i}(\boldsymbol{k}_0 \cdot \boldsymbol{r} + q_z z)} \theta_{\boldsymbol{k}_0 q_z}$ is a real-space phase field related to the vortex-lattice displacement field $\boldsymbol{u}(\boldsymbol{r}, z)$ [97] as

$$\begin{cases} u_x = l^2 \partial_y \theta \\ u_y = -l^2 \partial_x \theta. \end{cases} \tag{3.6.47}$$

This relation indicates that the vortex-lattice deformation corresponding to the massless mode $a^{(-)}_{\boldsymbol{k}_0 q_z}$ represents an incompressible shear mode: $\nabla_\perp \cdot \boldsymbol{u}(\boldsymbol{r}, z) = 0$ [97]. Also, c_{66} and $\rho_{\rm s}$ represent the shear modulus of the vortex lattice and the superfluid density defined as the response quantity in the z direction, respectively:

$$c_{66} = \frac{2\gamma_{\rm A} |\alpha_{\boldsymbol{q}_H}|^2}{{\beta_{\rm A}}^2 \beta}, \tag{3.6.48}$$

and

$$\rho_{\rm s} = \frac{2 |\alpha_{\boldsymbol{q}_H}| \gamma}{\beta_{\rm A} \beta}. \tag{3.6.49}$$

The mean square displacement of the vortex lattice $d^2 = \langle |\boldsymbol{u}(\boldsymbol{r})|^2 \rangle$ is calculated as

$$d^2 = \langle |\boldsymbol{u}|^2 \rangle = l^4 \left\langle (\nabla_\perp \theta)^2 \right\rangle = 2l^4 \sum_{\boldsymbol{k}_0, q_z > 0} {k_0}^2 \langle |\theta_{\boldsymbol{k}_0 q_z}|^2 \rangle. \tag{3.6.50}$$

Here, $\langle \cdots \rangle$ means the ensemble average with respect to the low-energy Ginzburg-Landau functional $\mathcal{F}_{\mathrm{GL}}^{\mathrm{Gauss}(-)}$ [Eq. (3.6.46)], and thus we can obtain the following formula:

$$d^2 = \frac{l^4}{L_x L_y L_z} \sum_{\boldsymbol{k}_0, q_z} \frac{T {k_0}^2}{c_{66} l^4 {k_0}^4 + \rho_{\mathrm{s}} {q_z}^2}. \tag{3.6.51}$$

Since the summation about q_z is convergent, we take ${L_z}^{-1} \sum_{q_z} (\cdots) \to (2\pi)^{-1} \int_{-\infty}^{\infty} \mathrm{d}q_z (\cdots)$. On the other hand, since the summation about $\boldsymbol{k}_0$ is not convergent if $k_0 \to \infty$, we simply replace the summation with an integration over an area corresponding to the first Brillouin zone: $(L_x L_y)^{-1} \sum_{\boldsymbol{k}_0} (\cdots) \to (2\pi)^{-1} \int_0^{\sqrt{2}/l} \mathrm{d}k_0 \, k_0 (\cdots)$. These replacements lead to the following simple expression:

$$d^2 = \frac{T}{4\pi \sqrt{\rho_{\mathrm{s}} c_{66}}}. \tag{3.6.52}$$

Using the Lindemann criterion [97], we can expect that the vortex lattice can melt into the vortex liquid when a condition $d = c \times l$ is satisfied [note that the magnetic length l corresponds to the unit-cell size (see Fig. 3.4)], where $c = \mathcal{O}(0.1)$ is a phenomenological parameter. Introducing a dimensionless magnetic field $h = 2\pi\mu_0 H/\phi_0 = l^{-2}$ (note that the lattice constant is set to unity), we obtain the equation [Eq. (3.3.8)] describing the melting-transition field, or the vortex-lattice-formation field, H_{melt}:

$$\frac{T}{4\pi \sqrt{\rho_{\mathrm{s}} c_{66}}} = \frac{c^2}{h}. \tag{3.6.53}$$

Chapter 4

Effects of change in dimensionality

4.1 Introduction to this chapter

As explained in Sec. 1.1, in many-Fermion systems with strong attractive interaction, it is expected that the BCS-BEC crossover can be experimentally induced by tuning the interaction strength. Actually, the Feshbach resonance has made it possible to realize the BCS-BEC crossover in ultracold Fermi gases [13]. On the other hand, material realization of the BCS-BEC crossover will open up another opportunity to study unexplored physical properties in systems with strong attractive interaction: for example, transport properties and orbital magnetic-field effects (see Chapters 2 and 3), which are generally difficult to explore in trapped and neutral ultracold Fermi gases. In contrast to the ultracold Fermi gases, however, it is difficult to control the strength of the attractive interaction in superconductors. Therefore, another idea is required to induce the BCS-BEC crossover in such a superconductor with strong attractive interaction as FeSe (see Sec. 1.2.2).

In this chapter, we propose an idea that the BCS-BEC crossover may be caused by changing the dimensionality, for example, by inserting additional insulating layers or applying pressure uniaxially. Using a simple model of a layered superconductor with strong attractive interaction, we calculate the pair-condensation temperature $T_{\rm c}$ and the pair-formation temperature T^* based on the T-matrix approximation [1, 28, 29, 30]. We find that $T_{\rm c}$ and T^* become more distant from each other as the dimensionality gets lower. In addition, on the basis of the same approximation, we show that the pseudogap appears in the electronic density of states when the interlayer hopping is small enough. These behaviors can be understood as the BCS-BEC crossover induced by the change in dimensionality.

4.2 Preliminary analysis of two-particle system

We consider an attractive Hubbard model to describe many electrons moving on a simple tetragonal lattice:

$$H = -t_{\parallel} \sum_{\langle i,j\rangle_{\parallel},\sigma} \left(c_{i\sigma}^{\dagger} c_{j\sigma} + c_{j\sigma}^{\dagger} c_{i\sigma} \right) - t_{\perp} \sum_{\langle i,j\rangle_{\perp},\sigma} \left(c_{i\sigma}^{\dagger} c_{j\sigma} + c_{j\sigma}^{\dagger} c_{i\sigma} \right) - U \sum_{i} c_{i\uparrow}^{\dagger} c_{i\downarrow}^{\dagger} c_{i\downarrow} c_{i\uparrow}, \qquad (4.2.1)$$

where $\langle i,j\rangle_{\parallel(\perp)}$ means intralayer (interlayer) nearest-neighbor bonds in the a-b plane (along the c axis), and correspondingly, $t_{\parallel}(>0)$ and $t_{\perp}(>0)$ are the intralayer- and the interlayer-hopping amplitudes, respectively. $U(>0)$ is the strength of the attractive interaction, and $c_{i\sigma}^{(\dagger)}$ represents the annihilation (creation) operator of an electron with spin σ at the site i.

There are two kinds of independent dimensionless parameters in our Hamiltonian. One is the anisotropy ratio $r = t_{\perp}/t_{\parallel}$ (≤ 1), which controls the dimensionality. In the limit of $r \to 1$ ($r \to 0$), the system is purely three (two) dimensional. The other is the dimensionless attractive-interaction strength $u = U/t_{\parallel}$.

In the two-dimensional limit ($r \to 0$), the pair condensation at a finite temperature is expected to be replaced by the Berezinskii-Kosterlitz-Thouless (BKT) transition [98, 111, 112, 113, 114, 115, 116]. In this chapter, we focus on a finite-r regime ($r \gtrsim 0.05$) and do not discuss the BKT transition.

Though quasi-two-dimensional models [98] and anisotropic lattice models [34, 35, 117] similar to Eq. (4.2.1) have been considered so far, the significant roles of the change in dimensionality has not been clarified. In addition, we stress that effects of the dimensionality change due to variation in the anisotropy ratio r are different from finite-size effects caused by confinement in the xy plane, which have been recently discussed in the context of ultracold Fermi gases [118, 119].

4.2.1 Formation of two-particle bound state

Let us consider a two-particle system described by Eq. (4.2.1). If the attractive interaction is controlled in a many-particle system, the BCS-BEC crossover will take place when the interaction becomes strong enough to form a two-particle bound state [3]. Thus, by solving the Schrödinger equation of the corresponding two-particle system and calculating the threshold interaction strength for the bound-state formation, we can roughly estimate the characteristic interaction strength, at which the BCS-BEC crossover occurs in the many-particle system [note that the threshold interaction strength is given in Eq. (2.2.3) as $U_0 = 4\pi/(mk_0)$ in Chapter 2 and given as $U_0 \simeq 8.14t$ in Chapter 3].

As shown in Sec. 4.5.1, a bound state exists in the two-particle system described by Eq. (4.2.1) when the equation for the binding energy $E_{\rm b}$,

$$\frac{U}{M} \sum_{\boldsymbol{k}} \frac{1}{2\epsilon_{\boldsymbol{k}} + W + E_{\rm b}} = 1, \qquad (4.2.2)$$

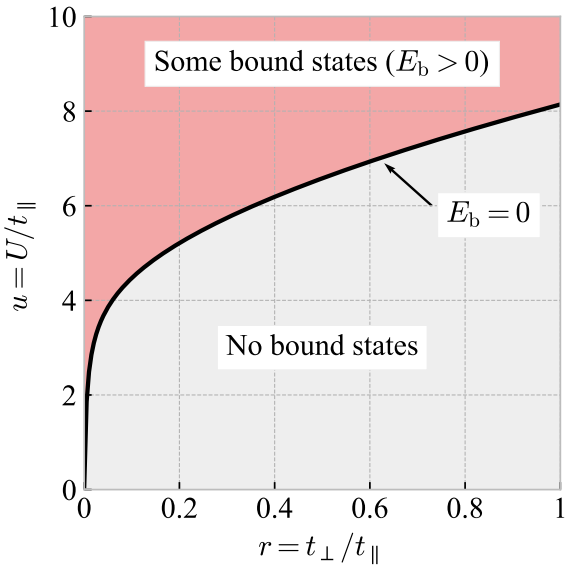

Figure 4.1: The region where the two-particle bound state exists ($E_\mathrm{b} > 0$) in the r-u plane (red area). The boundary satisfying $E_\mathrm{b} = 0$ (black line) and the region where no bound states exist (gray area) are also shown.

has a positive solution $E_\mathrm{b} > 0$. Here, we use the symbols $M = M_x M_y M_z$ as the number of lattice sites, $k_\alpha = 2\pi n_\alpha / M_\alpha$ ($\alpha = x, y, z$) as the lattice momentum under the periodic boundary condition, $\epsilon_{\boldsymbol{k}} = -2t_\parallel(\cos k_x + \cos k_y) - 2t_\perp \cos k_z$ as the free-particle energy dispersion, and $W = 8t_\parallel + 4t_\perp$ as the free-particle band width. The binding energy E_b is measured from the bottom of the free-particle energy band.

In Fig. 4.1, we show in the r-u plane the red region where the two-particle bound state exists ($E_\mathrm{b} > 0$). The black line represents the boundary where the bound-state energy vanishes ($E_\mathrm{b} = 0$). If u is changed under a fixed r, we obtain from Fig. 4.1 a certain value $u = u_0$, at which a bound state starts to appear (e.g., $u_0 = 6.58$ for $r = 0.5$). In the corresponding many-particle system, the BCS-BEC crossover is expected to occur when the interaction u is tuned through u_0. On the other hand, if r is changed under a fixed u, we find a certain value $r = r_0$, at which a bound state starts to appear (e.g., $r_0 = 0.356$ for $u = 6$). In the corresponding many-particle system, in the same way as the u-tuned case, we expect the BCS-BEC crossover to occur when the anisotropy ratio r is changed, or the dimensionality is tuned, through r_0. This is our basic idea. In the following, we show that this scenario can be actually realized on the basis of the separation between the pair-formation temperature T^* and the pair-condensation temperature T_c as well as the emergence of the pseudogap in the electronic density of states.

4.3 Dimensionality effects on phase diagram

4.3.1 Separation between pair-formation and pair-condensation temperatures

To show that the BCS-BEC crossover can occur through the change in dimensionality, we present the calculated results of the two characteristic temperatures, the pair-formation temperature T^* and the pair-condensation temperature $T_{\rm c}$.

The pair formation is not a transition but a crossover phenomenon, and here we estimate T^* based on the divergence of the uniform superconducting susceptibility $\chi_{\rm SC}$ within the mean-field approximation [26, 98]. Introducing the free-particle Green's function $G^{(0)}_{\boldsymbol{k}}(\mathrm{i}\varepsilon_n) = (\mathrm{i}\varepsilon_n - \epsilon_{\boldsymbol{k}} + \mu)^{-1}$, the uniform superconducting susceptibility is written as $\chi_{\rm SC} = \chi^{(0)}_{\boldsymbol{0}}(0)[1 - U\chi^{(0)}_{\boldsymbol{0}}(0)]^{-1}$, where

$$\chi^{(0)}_{\boldsymbol{q}}(\mathrm{i}\omega_m) = \frac{T}{M}\sum_{\boldsymbol{k},n} G^{(0)}_{\boldsymbol{k}+\boldsymbol{q}}(\mathrm{i}\varepsilon_n + \mathrm{i}\omega_m)G^{(0)}_{-\boldsymbol{k}}(-\mathrm{i}\varepsilon_n). \tag{4.3.1}$$

Here, we use the symbols T as the temperature and $\varepsilon_n = 2\pi(n+1/2)T$ ($\omega_m = 2\pi mT$) as the Fermion (Boson) Matsubara frequency. We estimate T^* by combining $U\chi^{(0)}_{\boldsymbol{0}}(0) = 1$ and the mean-field-level equation for the particle density n, $n = (2/M)\sum_{\boldsymbol{k}}\{\exp[(\epsilon_{\boldsymbol{k}} - \mu)/T] + 1\}^{-1}$. In the strong-coupling BEC limit ($u \to \infty$), we can easily show from the definitions that $T^* \propto |\mu| \propto U \propto E_{\rm b}$. Therefore, we can interpret T^* as a temperature where the pair formation (or pair breaking) occurs even when the attractive interaction is strong.

The pair-condensation, or the superconducting-transition, temperature $T_{\rm c}$ is calculated within the T-matrix approximation [1, 28, 29, 30]. This approximation is qualitatively correct as long as the density n is not so close to unity, and the chemical-potential shift is important. If n is close to unity, and the filling is about one-half, the chemical-potential shift is not so important, and the interaction between the superconducting fluctuations is crucial. In this case, the self energy should be estimated within a more sophisticated method, e.g., the self-consistent T-matrix approximation [1, 30, 31]. In the following, therefore, we consider a relatively low-density system with $n = 0.2$. Though the T-matrix approximation is already explained in detail in Chapter 3, we mention it again here for completeness of this chapter.

Within the T-matrix approximation, as we explain in Sec. 4.5.2, the pair-condensation temperature $T_{\rm c}$ is calculated by solving both the equation $U\chi^{(0)}_{\boldsymbol{0}}(0) = 1$ and the equation for the particle density n,

$$n = \frac{2T}{M}\sum_{\boldsymbol{k},n} G_{\boldsymbol{k}}(\mathrm{i}\varepsilon_n)\mathrm{e}^{+\mathrm{i}\varepsilon_n 0}. \tag{4.3.2}$$

Here, the interacting-particle Green's function $G_{\boldsymbol{k}}(\mathrm{i}\varepsilon_n)$ is given as

$$G_{\boldsymbol{k}}(\mathrm{i}\varepsilon_n)^{-1} = G^{(0)}_{\boldsymbol{k}}(\mathrm{i}\varepsilon_n)^{-1} - \Sigma_{\boldsymbol{k}}(\mathrm{i}\varepsilon_n), \tag{4.3.3}$$

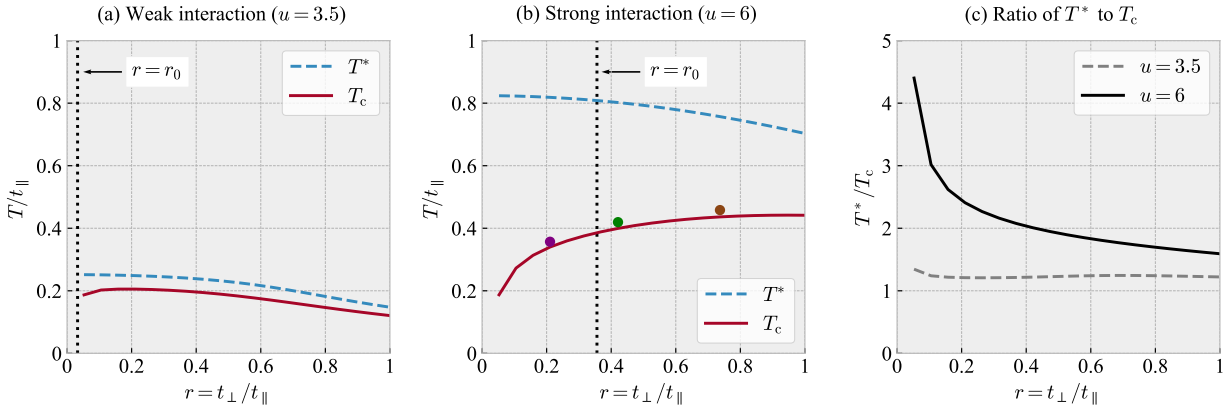

Figure 4.2: The pair-formation temperature T^* (blue dashed line) and the pair-condensation temperature T_c (red solid line) for systems with (a) weak interaction ($u = 3.5$) and (b) strong interaction ($u = 6$). At $r = r_0$ (black dotted line), the bound state starts to appear or vanish in the corresponding two-particle system. The colored points in (b) show $1.05T_c$ for each value of r, where the density of states are evaluated as shown in Fig. 4.4 below. In (c), the ratio of the pair-formation temperature T^* to the pair-condensation temperature T_c is shown.

and the self energy $\Sigma_{\boldsymbol{k}}(\mathrm{i}\varepsilon_n)$ satisfies the following equation:

$$\Sigma_{\boldsymbol{k}}(\mathrm{i}\varepsilon_n) = -\frac{T}{M}\sum_{\boldsymbol{q},m} G^{(0)}_{\boldsymbol{q}-\boldsymbol{k}}(\mathrm{i}\omega_m - \mathrm{i}\varepsilon_n)\frac{U^2\chi^{(0)}_{\boldsymbol{q}}(\mathrm{i}\omega_m)}{1 - U\chi^{(0)}_{\boldsymbol{q}}(\mathrm{i}\omega_m)}\mathrm{e}^{+\mathrm{i}(\omega_m-\varepsilon_n)0}. \tag{4.3.4}$$

To consider the physical meaning of T_c estimated in the above formulas, let us consider the strong-coupling BEC limit ($u \to \infty$) with $t_\parallel = t_\perp = t$. In this limit, we can obtain $T_c \propto t^2/U$, which corresponds to the BEC transition temperature of a non-interacting Bose system with a nearest-neighbor hopping $t_B \propto t^2/U$ [21] (see also Sec. 1.1). Therefore, T_c can be interpreted as the pair-condensation temperature even when the attractive interaction is strong.

The numerically calculated results of T^* and T_c are summarized in Figs. 4.2(a) and (b), which correspond to a system with weak interaction ($u = 3.5$) and a system with strong interaction ($u = 6$), respectively. The black dotted line shows the value of r_0, where the corresponding two-particle system begins to have a bound state.

In the case of $u = 3.5$ shown in Fig. 4.2(a), where $r_0 \sim 0$, the separation between T^* and T_c is small and does not change so much in a broad range of r. In fact, Fig. 4.2(c) shows that the ratio of T^* to T_c changes little for $u = 3.5$. This means that the pair formation and the pair condensation occur essentially at the same temperature as long as $r \gtrsim r_0$, and thus the BCS picture is applicable.

In the case of $u = 6$ shown in Fig. 4.2(b), the separation between T^* and T_c becomes more remarkable as r gets smaller through r_0. Actually, Fig. 4.2(c) shows that for $u = 6$

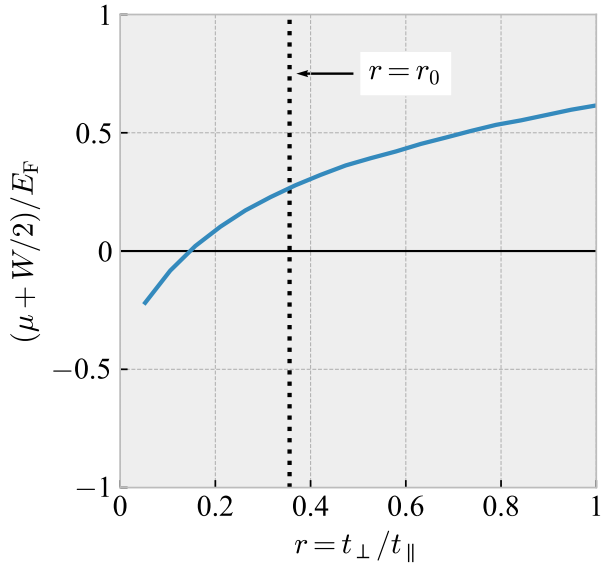

Figure 4.3: The r dependence of the chemical potential μ at the pair-condensation temperature T_{c} in the system with strong attractive interaction ($u = 6$). W and E_{F} represent the band width and the free-particle Fermi energy measured from the band bottom, respectively. The black dotted line shows $r = r_0$ as in Fig. 4.2(b).

the ratio of T^* to T_{c} increases as r decreases through r_0. The separation between T^* and T_{c} indicates that the BCS-BEC crossover takes place along with the change in r, or the change in dimensionality.

We also present the r dependence of the chemical potential μ at T_{c} for $u = 6$. As shown in Fig. 4.3, μ becomes lower than the bottom of the free-particle energy band ($\mu < -W/2$) when r is small enough. Since it is known that the chemical potential becomes lower than the band bottom through the BCS-BEC crossover [23], our result reinforces the scenario of the dimensionality-induced BCS-BEC crossover in the system with strong interaction.

4.3.2 Pseudogap in electronic density of states

To elucidate the effect of the dimensionality-induced BCS-BEC crossover on the one-particle excitation, we numerically calculate the electronic density of states $D(E)$ per spin per site. The calculation is based on the relation

$$D(E) = -\frac{1}{\pi} \lim_{\gamma \to +0} \mathrm{Im} G_{\boldsymbol{k}}(E + \mathrm{i}\gamma), \tag{4.3.5}$$

where $G_{\boldsymbol{k}}(\mathrm{i}\varepsilon_n)$ is given in Eq. (4.3.3). The Padé approximation is used for the analytic continuation from $G_{\boldsymbol{k}}(\mathrm{i}\varepsilon_n)$ to $G_{\boldsymbol{k}}(E + \mathrm{i}\gamma)$, and a finite energy width $\gamma = 0.1W$ is introduced

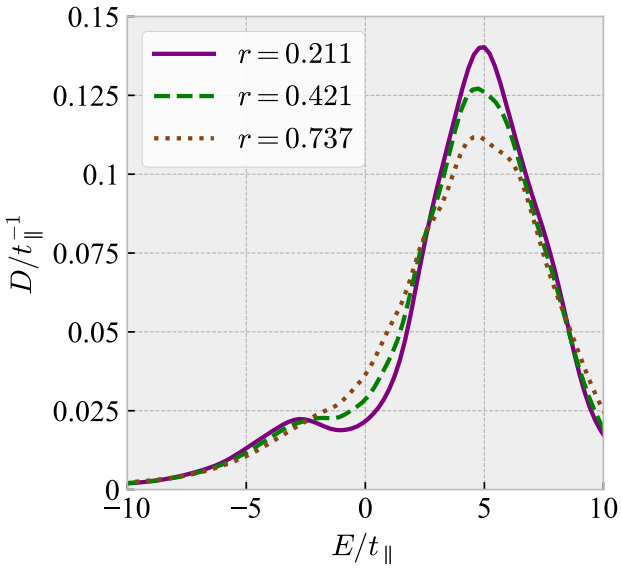

Figure 4.4: The electronic density of states for the systems with strong attractive interaction ($u = 6$) and around the pair-condensation temperature ($T = 1.05T_{\mathrm{c}}$). Each colored line corresponds to the colored point shown in Fig. 4.2(b): $r = 0.211$ (purple solid line), $r = 0.421$ (green dashed line), and $r = 0.737$ (brown dotted line).

in the numerical calculation.

Figure 4.4 shows the obtained density of states $D(E)$ for the systems with $u = 6$. As shown with the colored points in Fig. 4.2(b), we fix the temperature to $1.05T_{\mathrm{c}}$ and change the anisotropy ratio r . Figure 4.4 shows that the low-energy density of states becomes more depleted as r gets smaller. The depletion of the density of states can be understood as the emergence of the pseudogap caused by the preformed-pair formation [28]. Therefore, the behavior of the density of states is consistent with our picture of the dimensionality-induced BCS-BEC crossover. We note that the enhancement of the peak of $D(E)$ around $E/t_{\parallel} = 5$ in Fig. 4.4 basically originates from r dependence of the non-interacting density of states in our model with $U = 0$ and thus is not always expected when the dimensionality-induced BCS-BEC crossover occurs.

According to studies on ultracold Fermi gases, theoretically as well as experimentally it is still controversial how a pseudogap is reflected in observables such as specific heat and magnetic susceptibility [120, 121].

4.4 Discussion and summary

We present the idea of the dimensionality-induced BCS-BEC crossover on the basis of a simple many-particle system described by Eq. (4.2.1). We find that the separation between T^* and T_c, as well as the depletion of the low-energy density of states, becomes prominent when the anisotropy ratio r decreases through r_0. Here, r_0 is defined as a value of r, at which a bound state starts to appear in the corresponding two-particle system described by the same model [Eq. (4.2.1)].

In more general classes of layered two-particle systems with s-wave attractive interaction, it is known that a two-particle bound state always exists in the two-dimensional limit, or the strong-anisotropy limit, regardless of the interaction strength [122]. Therefore, in such two-particle systems, the bound state is expected to appear when the anisotropy becomes sufficiently strong (as $r < r_0$ in our model). Accordingly, the idea of the dimensionality-induced BCS-BEC crossover can be naturally extended to the corresponding more general classes of layered many-particle system.

Regarding layered superconductors with strong attractive interaction such as FeSe, tuning the anisotropy may trigger the BCS-BEC crossover as discussed in this chapter. As possible ways to control the anisotropy, we propose inserting additional insulating layers or applying uniaxial pressure/strain.

Before ending this section, we add some comments on recent experiments on FeSe-related materials. The dependence of T_c on the c-axis length c has been experimentally studied in metal-doped FeSe [e.g., $(NH_3)_yNa_xFeSe$ or (ethylenediamine)$_y$Li$_x$FeSe] and similarly metal-doped Fe($Se_{0.5}Te_{0.5}$) [123, 124]. Here, c can naturally have a negative correlation with the c-axis hopping amplitude ($t_\perp$ in our model). The T_c data show a sharp peak as a function of c [123, 124]. Our simple Hamiltonian [Eq. (4.2.1)] cannot describe such sharp increase and decrease in T_c as a function of c, and the origin of the sharp increase in T_c may be an increase in attractive interaction strength due to enhanced Fermi-surface nesting caused by decrease in dimensionality as speculated in Refs. [123, 124]. If this speculation is correct, it will be expected in these systems that as c increases (or the dimensionality decreases), a crossover from the BCS side to the BEC side can occur owing both to the decrease in dimensionality itself ($r = t_\perp/t_\parallel$ in our model) and accompanying increase in attractive interaction strength (U in our model).

4.5 Derivations of some formulas

4.5.1 Equation for binding energy

Let us consider the two-particle system described by the following Hamiltonian [Eq. (1) in the main text]:

$$H = -t_{\parallel} \sum_{\langle i,j\rangle_{\parallel},\sigma} \left(c^{\dagger}_{i\sigma} c_{j\sigma} + c^{\dagger}_{j\sigma} c_{i\sigma} \right) - t_{\perp} \sum_{\langle i,j\rangle_{\perp},\sigma} \left(c^{\dagger}_{i\sigma} c_{j\sigma} + c^{\dagger}_{j\sigma} c_{i\sigma} \right) - U \sum_{i} c^{\dagger}_{i\uparrow} c^{\dagger}_{i\downarrow} c_{i\downarrow} c_{i\uparrow}. \tag{4.5.1}$$

As explained in the main text, $\langle i,j\rangle_{\parallel(\perp)}$ means intralayer (interlayer) nearest-neighbor bonds in the a-b plane (along the c axis). In the same way, $t_{\parallel}(>0)$ and $t_{\perp}(>0)$ are the intralayer- and the interlayer-hopping amplitudes, respectively. $U(>0)$ is the strength of the attractive interaction, and $c^{(\dagger)}_{i\sigma}$ represents the annihilation (creation) operator of an electron with spin σ at the site i.

To find the equation for the binding energy of a two-particle bound state, we start with the general two-particle state as a candidate for the eigenstate of Eq. (4.5.1):

$$|\psi\rangle = \sum_{\boldsymbol{k},\boldsymbol{k}'} \sum_{\sigma,\sigma'} f_{\boldsymbol{k}\sigma,\boldsymbol{k}'\sigma'} \, |\boldsymbol{k}\sigma, \boldsymbol{k}'\sigma'\rangle = \sum_{\boldsymbol{k},\boldsymbol{k}'} \sum_{\sigma,\sigma'} f_{\boldsymbol{k}\sigma,\boldsymbol{k}'\sigma'} \, c^{\dagger}_{\boldsymbol{k}\sigma} c^{\dagger}_{\boldsymbol{k}'\sigma'} \, |0\rangle \, . \tag{4.5.2}$$

Here, $|0\rangle$ is the vacuum state, and the eigenfunction $f_{\boldsymbol{k}\sigma,\boldsymbol{k}'\sigma'}$ satisfies the antisymmetric relation

$$f_{\boldsymbol{k}'\sigma',\boldsymbol{k}\sigma} = -f_{\boldsymbol{k}\sigma,\boldsymbol{k}'\sigma'}. \tag{4.5.3}$$

The Schrödinger equation $H\,|\psi\rangle = E\,|\psi\rangle$, where E is the eigenenergy, leads to the following equation:

$$\begin{aligned} \sum_{\boldsymbol{k},\boldsymbol{k}'} \sum_{\sigma,\sigma'} (\epsilon_{\boldsymbol{k}} + \epsilon_{\boldsymbol{k}'}) f_{\boldsymbol{k}\sigma,\boldsymbol{k}'\sigma'} \, c^{\dagger}_{\boldsymbol{k}\sigma} c^{\dagger}_{\boldsymbol{k}'\sigma'} \, |0\rangle - \frac{2U}{M} \sum_{\boldsymbol{k},\boldsymbol{k}',\boldsymbol{k}''} f_{\boldsymbol{k}''+\boldsymbol{k}+\boldsymbol{k}'\uparrow,-\boldsymbol{k}''\downarrow} \, c^{\dagger}_{\boldsymbol{k}\uparrow} c^{\dagger}_{\boldsymbol{k}'\downarrow} \, |0\rangle \\ = E \sum_{\boldsymbol{k},\boldsymbol{k}'} \sum_{\sigma,\sigma'} f_{\boldsymbol{k}\sigma,\boldsymbol{k}'\sigma'} \, c^{\dagger}_{\boldsymbol{k}\sigma} c^{\dagger}_{\boldsymbol{k}'\sigma'} \, |0\rangle \, . \end{aligned} \tag{4.5.4}$$

Here, $\epsilon_{\boldsymbol{k}} = -2t_{\parallel}(\cos k_x + \cos k_y) - 2t_{\perp} \cos k_z$ is the free-particle energy dispersion.

For convenience, we split $f_{\boldsymbol{k}\uparrow,\boldsymbol{k}'\downarrow}$ into the symmetric part $f^{\mathrm{s}}_{\boldsymbol{k},\boldsymbol{k}'}$ and the antisymmetric part $f^{\mathrm{a}}_{\boldsymbol{k},\boldsymbol{k}'}$ as

$$\begin{aligned} f_{\boldsymbol{k}\uparrow,\boldsymbol{k}'\downarrow} = f^{\mathrm{s}}_{\boldsymbol{k},\boldsymbol{k}'} + f^{\mathrm{a}}_{\boldsymbol{k},\boldsymbol{k}'} &= \frac{f_{\boldsymbol{k}\uparrow,\boldsymbol{k}'\downarrow} + f_{\boldsymbol{k}'\uparrow,\boldsymbol{k}\downarrow}}{2} + \frac{f_{\boldsymbol{k}\uparrow,\boldsymbol{k}'\downarrow} - f_{\boldsymbol{k}'\uparrow,\boldsymbol{k}\downarrow}}{2} \\ &= \frac{f_{\boldsymbol{k}\uparrow,\boldsymbol{k}'\downarrow} - f_{\boldsymbol{k}\downarrow,\boldsymbol{k}'\uparrow}}{2} + \frac{f_{\boldsymbol{k}\uparrow,\boldsymbol{k}'\downarrow} + f_{\boldsymbol{k}\downarrow,\boldsymbol{k}'\uparrow}}{2}. \end{aligned} \tag{4.5.5}$$

In the last equality, Eq. (4.5.3) is used. Comparing the coefficients of $c^{\dagger}_{\boldsymbol{k}\sigma} c^{\dagger}_{\boldsymbol{k}'\sigma} \, |0\rangle$ ($\sigma = \uparrow, \downarrow$) in Eq. (4.5.4) with one another, we obtain

$$(\epsilon_{\boldsymbol{k}} + \epsilon_{\boldsymbol{k}'}) f_{\boldsymbol{k}\sigma,\boldsymbol{k}'\sigma} = E f_{\boldsymbol{k}\sigma,\boldsymbol{k}'\sigma} \quad (\sigma = \uparrow, \downarrow). \tag{4.5.6}$$

On the other hand, comparing the coefficients of $c^\dagger_{\boldsymbol{k}\uparrow}c^\dagger_{\boldsymbol{k}'\downarrow}|0\rangle$ in Eq. (4.5.4) with one another, we obtain

$$(\epsilon_{\boldsymbol{k}}+\epsilon_{\boldsymbol{k}'})f^{\rm a}_{\boldsymbol{k},\boldsymbol{k}'}=Ef^{\rm a}_{\boldsymbol{k},\boldsymbol{k}'} \tag{4.5.7}$$

and

$$(\epsilon_{\boldsymbol{k}}+\epsilon_{\boldsymbol{k}'})f^{\rm s}_{\boldsymbol{k},\boldsymbol{k}'}-\frac{U}{M}\sum_{\boldsymbol{k}''}f^{\rm s}_{\boldsymbol{k}''+\boldsymbol{k}+\boldsymbol{k}',-\boldsymbol{k}''}=Ef^{\rm s}_{\boldsymbol{k},\boldsymbol{k}'}. \tag{4.5.8}$$

First, we focus on $f_{\boldsymbol{k}\sigma,\boldsymbol{k}'\sigma}$ ($\sigma=\uparrow,\downarrow$) and $f^{\rm a}_{\boldsymbol{k},\boldsymbol{k}'}$. Since they represent the eigenfunctions of the spin-triplet two-particle states, the singlet-channel attractive interaction U does not work as seen in eq4S. (4.5.6) and (4.5.7), so that there are no bound states. Second, we focus on $f^{\rm s}_{\boldsymbol{k},\boldsymbol{k}'}$. This eigenfunction corresponds to the spin-singlet two-particle state and is affected by the attractive interaction U as seen in Eq. (4.5.8), and thus a bound state may appear in $f^{\rm s}_{\boldsymbol{k},\boldsymbol{k}'}$. Therefore, we discuss Eq. (4.5.8) in the following.

Let us assume that a bound state exists, so that the eigenenergy E is below the free-particle ground-state energy $-W$, where $W=8t_\parallel+4t_\perp$ is the free-particle band width. The binding energy $E_{\rm b}(>0)$ is defined as $E=-W-E_{\rm b}$. Defining $A_{\boldsymbol{q}}=M^{-1}\sum_{\boldsymbol{k}}f^{\rm s}_{\boldsymbol{k}+\boldsymbol{q},-\boldsymbol{k}}$, we obtain from Eq. (4.5.8)

$$f^{\rm s}_{\boldsymbol{k}+\boldsymbol{q},-\boldsymbol{k}}=\frac{UA_{\boldsymbol{q}}}{\epsilon_{\boldsymbol{k}+\boldsymbol{q}}+\epsilon_{-\boldsymbol{k}}+W+E_{\rm b}}. \tag{4.5.9}$$

Summation over $\boldsymbol{k}$ in both sides of this equation leads to

$$\frac{U}{M}\sum_{\boldsymbol{k}}\frac{1}{\epsilon_{\boldsymbol{k}+\boldsymbol{q}}+\epsilon_{-\boldsymbol{k}}+W+E_{\rm b}}=1. \tag{4.5.10}$$

Since we are interested in the bound state with zero total momentum, we set $\boldsymbol{q}=\boldsymbol{0}$ and obtain the final expression for the binding energy $E_{\rm b}$ [Eq. (2) in the main text]:

$$\frac{U}{M}\sum_{\boldsymbol{k}}\frac{1}{2\epsilon_{\boldsymbol{k}}+W+E_{\rm b}}=1. \tag{4.5.11}$$

4.5.2 T-matrix approximation

For the sake of completeness, we explain the T-matrix approximation used to calculate the pair-condensation temperature $T_{\rm c}$. We introduce the free-particle Green's function

$$G^{(0)}_{\boldsymbol{k}}({\rm i}\varepsilon_n)=\frac{1}{{\rm i}\varepsilon_n-\epsilon_{\boldsymbol{k}}+\mu}, \tag{4.5.12}$$

where $\varepsilon_n=2\pi(n+1/2)T$ is the Fermion Matsubara frequency with temperature T, and μ is the chemical potential. The interacting-particle Green's function satisfies the following Dyson's equation:

$$G_{\boldsymbol{k}}({\rm i}\varepsilon_n)^{-1}=G^{(0)}_{\boldsymbol{k}}({\rm i}\varepsilon_n)^{-1}-\Sigma_{\boldsymbol{k}}({\rm i}\varepsilon_n), \tag{4.5.13}$$

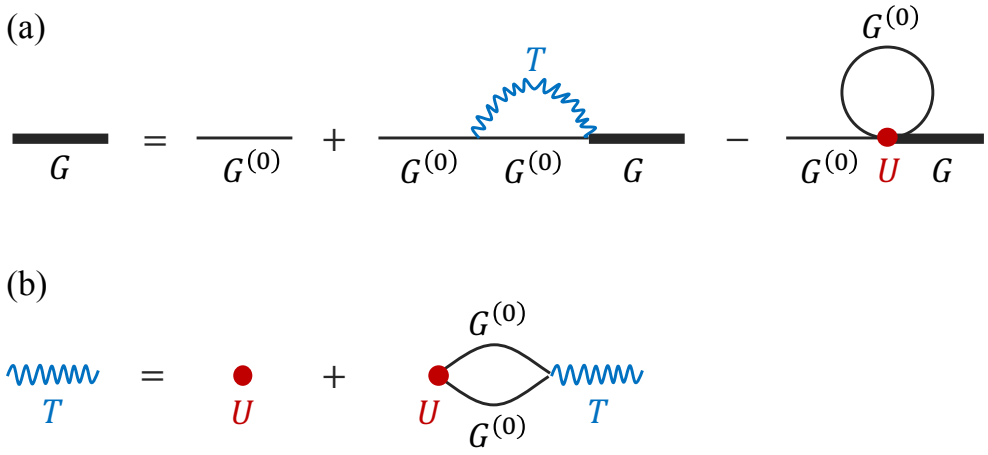

Figure 4.5: The diagrammatic representation of Eqs. (4.5.13), (4.5.15), and (4.5.17). (a) The upper diagram shows the Dyson's equation, which gives the relation among the interacting-particle Green's function $G_{\boldsymbol{k}}(\mathrm{i}\varepsilon_n)$ (black bold line), the free-particle Green's function $G^{(0)}_{\boldsymbol{k}}(\mathrm{i}\varepsilon_n)$ (black thin line), the T matrix $T_{\boldsymbol{q}}(\mathrm{i}\omega_m)$ (blue wavy line), and the bare attractive interaction U (red point). (b) The lower diagram expresses the recursive definition of the T matrix $T_{\boldsymbol{q}}(\mathrm{i}\omega_m)$.

where $\Sigma_{\boldsymbol{k}}(\mathrm{i}\varepsilon_n)$ is the self energy, which is estimated within the T-matrix approximation as explained in the following.

We define $\chi^{(0)}_{\boldsymbol{q}}(\mathrm{i}\omega_m)$ as

$$\chi^{(0)}_{\boldsymbol{q}}(\mathrm{i}\omega_m) = \frac{T}{M}\sum_{\boldsymbol{k},n} G^{(0)}_{\boldsymbol{k}+\boldsymbol{q}}(\mathrm{i}\varepsilon_n + \mathrm{i}\omega_m)G^{(0)}_{-\boldsymbol{k}}(-\mathrm{i}\varepsilon_n), \tag{4.5.14}$$

where $\omega_m = 2\pi mT$ is the Boson Matsubara frequency. We also define the T matrix $T_{\boldsymbol{q}}(\mathrm{i}\omega_m)$ as

$$T_{\boldsymbol{q}}(\mathrm{i}\omega_m) = \frac{U}{1 - U\chi^{(0)}_{\boldsymbol{q}}(\mathrm{i}\omega_m)}. \tag{4.5.15}$$

Before discussing the T-matrix approximation, we consider the Hartree term:

$$\Sigma^{(\mathrm{H})} = -U\frac{T}{M}\sum_{\boldsymbol{k},n} G_{\boldsymbol{k}}(\mathrm{i}\varepsilon_n)\mathrm{e}^{+\mathrm{i}\varepsilon_n 0} = -\frac{Un}{2}, \tag{4.5.16}$$

where n is the particle density. The contribution of this term to the self energy is constant if U and n are fixed. Thus, we take into account the Hartree term by properly choosing the origin of energy; in other words, we do not explicitly treat $\Sigma^{(\mathrm{H})}$ in the expression of the self energy.

Within the T-matrix approximation, the self energy is expressed as

$$\Sigma_{\boldsymbol{k}}(\mathrm{i}\varepsilon_n) = -\frac{T}{M}\sum_{\boldsymbol{q},m} G^{(0)}_{\boldsymbol{q}-\boldsymbol{k}}(\mathrm{i}\omega_m - \mathrm{i}\varepsilon_n) T_{\boldsymbol{q}}(\mathrm{i}\omega_m)\mathrm{e}^{+\mathrm{i}(\omega_m-\varepsilon_n)0} - \Sigma^{(1)}, \tag{4.5.17}$$

where $\Sigma^{(1)} = -U(T/M)\sum_{\boldsymbol{k},n} G^{(0)}_{\boldsymbol{k}}(\mathrm{i}\varepsilon_n)\mathrm{e}^{+\mathrm{i}\varepsilon_n 0}$ is the first-order perturbation term, which is implicitly taken into account in the Hartree term. Putting together the two terms in the right-hand side of Eq. (4.5.17), we obtain the explicit representation of the self energy [Eq. (6) in the main text]:

$$\Sigma_{\boldsymbol{k}}(\mathrm{i}\varepsilon_n) = -\frac{T}{M}\sum_{\boldsymbol{q},m} G^{(0)}_{\boldsymbol{q}-\boldsymbol{k}}(\mathrm{i}\omega_m - \mathrm{i}\varepsilon_n)\frac{U^2\chi^{(0)}_{\boldsymbol{q}}(\mathrm{i}\omega_m)}{1 - U\chi^{(0)}_{\boldsymbol{q}}(\mathrm{i}\omega_m)}\mathrm{e}^{+\mathrm{i}(\omega_m-\varepsilon_n)0}. \tag{4.5.18}$$

Equations (4.5.13), (4.5.15), and (4.5.17) are illustrated in Fig. 4.5 with the diagrammatic representation.

To consider the pair-condensation temperature T_{c} within the T-matrix approximation, we define the uniform superconducting susceptibility χ_{SC} as

$$\chi_{\mathrm{SC}} = \frac{\chi^{(0)}_{\boldsymbol{0}}(0)}{1 - U\chi^{(0)}_{\boldsymbol{0}}(0)}. \tag{4.5.19}$$

T_{c} is determined based on the divergence of χ_{SC}; in other words, we calculate T_{c} by solving the following equation:

$$U\chi^{(0)}_{\boldsymbol{0}}(0) = 1. \tag{4.5.20}$$

From Eq. (4.5.20), we can obtain T_{c} as a function of the chemical potential μ. Since we fix not the chemical potential μ but the number density n, we have to solve the following number equation [Eq. (4) in the main text] together with Eq. (4.5.20) to determine the value of μ:

$$n = \frac{T}{M}\sum_{\boldsymbol{k},\sigma,n} G_{\boldsymbol{k}}(\mathrm{i}\varepsilon_n)\mathrm{e}^{+\mathrm{i}\varepsilon_n 0} = \frac{2T}{M}\sum_{\boldsymbol{k},n} G_{\boldsymbol{k}}(\mathrm{i}\varepsilon_n)\mathrm{e}^{+\mathrm{i}\varepsilon_n 0}. \tag{4.5.21}$$

Chapter 5

Conclusion

In this thesis, we have investigated physical properties of superconductivity in the BCS-BEC crossover regime, focusing especially on fluctuation and dimensionality effects.

In Chapter 2, based on a simple model of a three-dimensional electron system, we consider superconducting fluctuation (SCF) effects on thermodynamic quantities such as the specific heat and magnetization [8]. Comparing the temperature and field dependences of thermodynamic quantities in the BCS-BEC crossover regime with those in the BCS regime, we find the following three features specific to the BCS-BEC crossover regime. First, due to the strong mode coupling between SCFs, the SCF-induced specific heat and diamagnetic susceptibility can seemingly exceed the corresponding values estimated within the Gaussian approximation. Second, the lowest-Landau-level (LLL) scaling can break down because of the important contribution of the higher-LL modes ($N \geq 1$) in addition to the LLL modes ($N = 0$). Third, both the LLL modes and the higher-LL modes can lead to the crossing behavior of magnetization curves in a broad range of magnetic fields. Our numerical results of diamagnetic susceptibility and magnetization curves are qualitatively consistent with the recent magnetic-torque and magnetization measurements in FeSe. To consider quantitative details of the diamagnetic response in FeSe and the qualitative difference in the zero-field specific-heat behavior between our numerical results and the experimental results in FeSe, we need to take into account the two-band nature of FeSe within a more sophisticated approximation.

In Chapter 3, starting from a simple attractive Hubbard model, we consider qualitative features of the field-temperature (H-T) phase diagram [9]. Applying the T-matrix theory combined with an analysis of the Ginzburg-Landau action, we estimate the three characteristic field strengths: the pair-formation field H^*, the vortex-liquid-formation field H_{c2}, and the vortex-lattice-formation field $H_{\rm melt}$. Interestingly, our numerical results suggest that the vortex-liquid and preformed-pair regions are broaden in the H-T plane in the BCS-BEC crossover regime compared with those in the BCS regime. This feature can be understood as caused by the enhanced SCF effects in the BCS-BEC crossover regime. We also point out

the importance of the particle density in determining the H-T phase diagram. The obtained features of the H-T phase diagram in the BCS-BEC crossover regime can be consistent with the experimentally suggested strong SCF effects and pseudogap formation in FeSe though they are inconsistent with the experimentally estimated narrow vortex-liquid region. To consider this inconsistency, we suggest a possibility that vortices in a stronger-coupling band in FeSe can be pinned by vortices in another weaker-coupling band.

In Chapter 4, we consider effects of the change in dimensionality by analyzing a simple anisotropic attractive Hubbard model within the T-matrix approximation. Our numerical calculations show that the separation between the pair-formation temperature T^* and the pair-condensation temperature T_c, in addition to the depletion of the low-energy density of states, becomes more prominent as the system becomes more two-dimensional like due to an increase in the anisotropy. Based on this result, we conclude that the change in dimensionality can induce the BCS-BEC crossover in layered superconductors. As possible ways to realize this dimensionality-induced BCS-BEC crossover in layered superconductors with strong attractive interaction such as FeSe, we propose inserting insulating layers between superconducting layers and applying uniaxial pressure or strain.

In this thesis, we concentrate on characteristic properties emerging in single-band systems with strong attractive interaction. As mentioned several times, however, the candidate material in the BCS-BEC crossover regime, FeSe, is actually a multiband system. Therefore, FeSe provides an opportunity to investigate intertwined effects between the multiband nature and the BCS-BEC crossover. In multiband systems, the character of each band and the interband interactions can have some impacts on the whole system's behavior, for instance, thermodynamic or transport properties. Theoretical consideration of systems with the multiband structure in addition to the strong attractive interaction will improve understanding of FeSe and potentially lead to finding new physical phenomena unique to such an unprecedented situation.

Bibliography

[1] Q. Chen, J. Stajic, S. Tan, and K. Levin, Phys. Rep. **412**, 1 (2005).

[2] W. Zwerger, ed., *The BCS-BEC Crossover and the Unitary Fermi Gas* (Springer-Verlag Berlin Heidelberg, 2012).

[3] M. Randeria and E. Taylor, Annu. Rev. Condens. Matter Phys. **5**, 209 (2014).

[4] C. Chin, R. Grimm, P. Julienne, and E. Tiesinga, Rev. Mod. Phys. **82**, 1225 (2010).

[5] S. Kasahara, T. Watashige, T. Hanaguri, Y. Kohsaka, T. Yamashita, Y. Shimoyama, Y. Mizukami, R. Endo, H. Ikeda, K. Aoyama, T. Terashima, S. Uji, T. Wolf, H. v. Löhneysen, T. Shibauchi, and Y. Matsuda, Proc. Nat. Acad. Sci. USA **111**, 16309 (2014).

[6] S. Kasahara, T. Yamashita, A. Shi, R. Kobayashi, Y. Shimoyama, T. Watashige, K. Ishida, T. Terashima, T. Wolf, F. Hardy, C. Meingast, H. v. Löhneysen, A. Levchenko, T. Shibauchi, and Y. Matsuda, Nat. Commun. **7**, 12843 (2016).

[7] S. Rinott, K. B. Chashka, A. Ribak, E. D. L. Rienks, A. Taleb-Ibrahimi, P. Le Fevre, F. Bertran, M. Randeria, and A. Kanigel, Sci. Adv. **3**, e1602372 (2017).

[8] K. Adachi and R. Ikeda, Phys. Rev. B **96**, 184507 (2017).

[9] K. Adachi and R. Ikeda, arXiv:1811.07295 (submitted to Phys. Rev. B).

[10] K. Adachi and R. Ikeda, Phys. Rev. B **98**, 184502 (2018).

[11] J. Bardeen, L. N. Cooper, and J. R. Schrieffer, Phys. Rev. **108**, 1175 (1957).

[12] M. Tinkham, *Introduction to Superconductivity: Second Edition* (McGraw-Hill, NewYork, 1996).

[13] I. Bloch, J. Dalibard, and W. Zwerger, Rev. Mod. Phys. **80**, 885 (2008).

[14] M. W. Zwierlein, J. R. Abo-Shaeer, A. Schirotzek, C. H. Schunck, and W. Ketterle, Nature **435**, 1047 (2005).

[15] N. Andrenacci, A. Perali, P. Pieri, and G. C. Strinati, Phys. Rev. B **60**, 12410 (1999).

[16] B. C. den Hertog, Phys. Rev. B **60**, 559 (1999).

[17] L. Wang, F. Hardy, T. Wolf, P. Adelmann, R. Fromknecht, P. Schweiss, and C. Meingast, Phys. Status Solidi B **254**, 1600153 (2017).

[18] L. Jiao, C.-L. Huang, S. Rößler, C. Koz, U. K. Rößler, U. Schwarz, and S. Wirth, Sci. Rep. **7**, 44024 (2017).

[19] A. Muratov, A. Sadakov, S. Gavrilkin, A. Prishchepa, G. Epifanova, D. Chareev, and V. Pudalov, Physica B **536**, 785 (2018).

[20] Y. Sato, S. Kasahara, T. Taniguchi, X. Xing, Y. Kasahara, Y. Tokiwa, Y. Yamakawa, H. Kontani, T. Shibauchi, and Y. Matsuda, Proc. Nat. Acad. Sci. USA **115**, 1227 (2018).

[21] R. Micnas, J. Ranninger, and S. Robaszkiewicz, Rev. Mod. Phys. **62**, 113 (1990).

[22] A. J. Leggett, in *Modern Trends in the Theory of Condensed Matter*, edited by A. Pekalski and J. Przystawa (Springer-Verlag Berlin Heidelberg, 1980) p. 13.

[23] P. Nozières and S. Schmitt-Rink, J. Low Temp. Phys. **59**, 195 (1985).

[24] R. B. Diener, R. Sensarma, and M. Randeria, Phys. Rev. A **77**, 023626 (2008).

[25] L. He, H. Lü, G. Cao, H. Hu, and X.-J. Liu, Phys. Rev. A **92**, 023620 (2015).

[26] C. A. R. Sá de Melo, M. Randeria, and J. R. Engelbrecht, Phys. Rev. Lett. **71**, 3202 (1993).

[27] D. J. Thouless, Ann. Phys. **10**, 553 (1960).

[28] S. Tsuchiya, R. Watanabe, and Y. Ohashi, Phys. Rev. A **80**, 033613 (2009).

[29] J. Maly, B. Jankó, and K. Levin, Physica C **321**, 113 (1999).

[30] Y. Yanase and K. Yamada, J. Phys. Soc. Jpn. **68**, 2999 (1999).

[31] R. Haussmann, Phys. Rev. B **49**, 12975 (1994).

[32] R. Haussmann, W. Rantner, S. Cerrito, and W. Zwerger, Phys. Rev. A **75**, 023610 (2007).

[33] J. Maly, B. Jankó, and K. Levin, Phys. Rev. B **59**, 1354 (1999).

[34] Q. Chen, I. Kosztin, B. Jankó, and K. Levin, Phys. Rev. Lett. **81**, 4708 (1998).

[35] Q. Chen, I. Kosztin, B. Jankó, and K. Levin, Phys. Rev. B **59**, 7083 (1999).

[36] T. Kashimura, R. Watanabe, and Y. Ohashi, Phys. Rev. A **86**, 043622 (2012).

[37] H. Tajima, T. Kashimura, R. Hanai, R. Watanabe, and Y. Ohashi, Phys. Rev. A **89**, 033617 (2014).

[38] E. Burovski, N. Prokof'ev, B. Svistunov, and M. Troyer, Phys. Rev. Lett. **96**, 160402 (2006).

[39] E. Burovski, E. Kozik, N. Prokof'ev, B. Svistunov, and M. Troyer, Phys. Rev. Lett. **101**, 090402 (2008).

[40] O. Goulko and M. Wingate, Phys. Rev. A **82**, 053621 (2010).

[41] D. Liu, W. Zhang, D. Mou, J. He, Y.-B. Ou, Q.-Y. Wang, Z. Li, L. Wang, L. Zhao, S. He, Y. Peng, X. Liu, C. Chen, L. Yu, G. Liu, X. Dong, J. Zhang, C. Chen, Z. Xu, J. Hu, X. Chen, X. Ma, Q. Xue, and X. J. Zhou, Nat. Commun. **3**, 931 (2012).

[42] J. J. Lee, F. T. Schmitt, R. G. Moore, S. Johnston, Y.-T. Cui, W. Li, M. Yi, Z. K. Liu, M. Hashimoto, Y. Zhang, D. H. Lu, T. P. Devereaux, D.-H. Lee, and Z.-X. Shen, Nature **515**, 245 (2014).

[43] X. Liu, D. Liu, W. Zhang, J. He, L. Zhao, S. He, D. Mou, F. Li, C. Tang, Z. Li, L. Wang, Y. Peng, Y. Liu, C. Chen, L. Yu, G. Liu, X. Dong, J. Zhang, C. Chen, Z. Xu, X. Chen, X. Ma, Q. Xue, and X. J. Zhou, Nat. Commun. **5**, 5047 (2014).

[44] R. Peng, X. P. Shen, X. Xie, H. C. Xu, S. Y. Tan, M. Xia, T. Zhang, H. Y. Cao, X. G. Gong, J. P. Hu, B. P. Xie, and D. L. Feng, Phys. Rev. Lett. **112**, 107001 (2014).

[45] R. Peng, H. C. Xu, S. Y. Tan, H. Y. Cao, M. Xia, X. P. Shen, Z. C. Huang, C. H. P. Wen, Q. Song, T. Zhang, B. P. Xie, X. G. Gong, and D. L. Feng, Nat. Commun. **5**, 5044 (2014).

[46] Y. Miyata, K. Nakayama, K. Sugawara, T. Sato, and T. Takahashi, Nat. Mater. **14**, 775 (2015).

[47] J. Shiogai, Y. Ito, T. Mitsuhashi, T. Nojima, and A. Tsukazaki, Nat. Phys. **12**, 42 (2015).

[48] X. Shi, Z.-Q. Han, X.-L. Peng, P. Richard, T. Qian, X.-X. Wu, M.-W. Qiu, S. C. Wang, J. P. Hu, Y.-J. Sun, and H. Ding, Nat. Commun. **8**, 14988 (2017).

[49] S. Tan, Y. Zhang, M. Xia, Z. Ye, F. Chen, X. Xie, R. Peng, D. Xu, Q. Fan, H. Xu, J. Jiang, T. Zhang, X. Lai, T. Xiang, J. Hu, B. Xie, and D. Feng, Nat. Mater. **12**, 634 (2013).

[50] W. Li, Y. Zhang, P. Deng, Z. Xu, S.-K. Mo, M. Yi, H. Ding, M. Hashimoto, R. G. Moore, D.-H. Lu, X. Chen, Z.-X. Shen, and Q.-K. Xue, Nat. Phys. **13**, 957 (2017).

[51] F.-C. Hsu, J.-Y. Luo, K.-W. Yeh, T.-K. Chen, T.-W. Huang, P. M. Wu, Y.-C. Lee, Y.-L. Huang, Y.-Y. Chu, D.-C. Yan, and M.-K. Wu, Proc. Nat. Acad. Sci. USA **105**, 14262 (2008).

[52] T. Terashima, N. Kikugawa, A. Kiswandhi, E.-S. Choi, J. S. Brooks, S. Kasahara, T. Watashige, H. Ikeda, T. Shibauchi, Y. Matsuda, T. Wolf, A. E. Böhmer, F. Hardy, C. Meingast, H. v. Löhneysen, M.-T. Suzuki, R. Arita, and S. Uji, Phys. Rev. B **90**, 144517 (2014).

[53] C. Koz, M. Schmidt, H. Borrmann, U. Burkhardt, S. Rößler, W. Carrillo-Cabrera, W. Schnelle, U. Schwarz, and Y. Grin, Z. Anorg. Allg. Chem. **640**, 1600 (2014).

[54] K. Nakayama, Y. Miyata, G. N. Phan, T. Sato, Y. Tanabe, T. Urata, K. Tanigaki, and T. Takahashi, Phys. Rev. Lett. **113**, 237001 (2014).

[55] T. Shimojima, Y. Suzuki, T. Sonobe, A. Nakamura, M. Sakano, J. Omachi, K. Yoshioka, M. Kuwata-Gonokami, K. Ono, H. Kumigashira, A. E. Böhmer, F. Hardy, T. Wolf, C. Meingast, H. v. Löhneysen, H. Ikeda, and K. Ishizaka, Phys. Rev. B **90**, 121111 (2014).

[56] M. D. Watson, T. K. Kim, A. A. Haghighirad, N. R. Davies, A. McCollam, A. Narayanan, S. F. Blake, Y. L. Chen, S. Ghannadzadeh, A. J. Schofield, M. Hoesch, C. Meingast, T. Wolf, and A. I. Coldea, Phys. Rev. B **91**, 155106 (2015).

[57] P. Zhang, T. Qian, P. Richard, X. P. Wang, H. Miao, B. Q. Lv, B. B. Fu, T. Wolf, C. Meingast, X. X. Wu, Z. Q. Wang, J. P. Hu, and H. Ding, Phys. Rev. B **91**, 214503 (2015).

[58] Y. Yamakawa, S. Onari, and H. Kontani, Phys. Rev. X **6**, 021032 (2016).

[59] A. V. Chubukov, M. Khodas, and R. M. Fernandes, Phys. Rev. X **6**, 041045 (2016).

[60] R. M. Fernandes and A. V. Chubukov, Rep. Prog. Phys. **80**, 014503 (2017).

[61] R. M. Fernandes, A. V. Chubukov, and J. Schmalian, Nat. Phys. **10**, 97 (2014).

[62] H. Kontani and Y. Yamakawa, Phys. Rev. Lett. **113**, 047001 (2014).

[63] Y. Yamakawa and H. Kontani, Phys. Rev. B **96**, 144509 (2017).

[64] A. Shi, T. Arai, S. Kitagawa, T. Yamanaka, K. Ishida, A. E. Böhmer, C. Meingast, T. Wolf, M. Hirata, and T. Sasaki, J. Phys. Soc. Jpn. **87**, 013704 (2017).

[65] A. Schmid, Phys. Rev. **180**, 527 (1969).

[66] T. Debelhoir and N. Dupuis, Phys. Rev. A **93**, 023642 (2016).

[67] H. Takahashi, F. Nabeshima, R. Ogawa, E. Ohmichi, H. Ohta, and A. Maeda, arXiv:1811.12778.

[68] Q. Li, M. Suenaga, T. Hikata, and K. Sato, Phys. Rev. B **46**, 5857(R) (1992).

[69] Z. Tešanović and L. Xing, Phys. Rev. Lett. **67**, 2729 (1991).

[70] T. Shibauchi and Y. Mizukami, private communication.

[71] Z. Tešanović, L. Xing, L. Bulaevskii, Q. Li, and M. Suenaga, Phys. Rev. Lett. **69**, 3563 (1992).

[72] B. Liu, H. Zhai, and S. Zhang, Phys. Rev. A **90**, 051602 (2014).

[73] K. Adachi and R. Ikeda, Phys. Rev. B **93**, 134503 (2016).

[74] C. Carballeira, J. Mosqueira, A. Revcolevschi, and F. Vidal, Phys. Rev. Lett. **84**, 3157 (2000).

[75] X. Jiang, D. Li, and B. Rosenstein, Phys. Rev. B **89**, 064507 (2014).

[76] R. Ikeda, Phys. Rev. B **66**, 100511(R) (2002).

[77] A. Finkel'stein, Physica B **197**, 636 (1994).

[78] H. Ishida and R. Ikeda, J. Phys. Soc. Jpn. **67**, 983 (1998).

[79] I. S. Beloborodov, K. B. Efetov, A. V. Lopatin, and V. M. Vinokur, Phys. Rev. B **71**, 184501 (2005).

[80] R. E. Prange, Phys. Rev. B **1**, 2349 (1970).

[81] R. Ikeda, J. Phys. Soc. Jpn. **64**, 1683 (1995).

[82] J. Mosqueira, C. Carballeira, and F. Vidal, Phys. Rev. Lett. **87**, 167009 (2001).

[83] X. T. Wu and R. Ikeda, Phys. Rev. B **83**, 104517 (2011).

[84] R. Ikeda, T. Ohmi, and T. Tsuneto, J. Phys. Soc. Jpn. **58**, 1377 (1989).

[85] T. Nattermann and S. Scheidl, Adv. Phys. **49**, 607 (2000).

[86] G. J. Ruggeri and D. J. Thouless, J. Phys. F **6**, 2063 (1976).

[87] U. Welp, S. Fleshler, W. K. Kwok, R. A. Klemm, V. M. Vinokur, J. Downey, B. Veal, and G. W. Crabtree, Phys. Rev. Lett. **67**, 3180 (1991).

[88] A. E. Koshelev and A. A. Varlamov, Supercond. Sci. Technol. **27**, 124001 (2014).

[89] C. Chi, X. Jiang, J. Wang, D. Li, and B. Rosenstein, Phys. Rev. B **96**, 224509 (2017).

[90] M. Machida and T. Koyama, Phys. Rev. Lett. **94**, 140401 (2005).

[91] R. Sensarma, M. Randeria, and T.-L. Ho, Phys. Rev. Lett. **96**, 090403 (2006).

[92] H. J. Warringa and A. Sedrakian, Phys. Rev. A **84**, 023609 (2011).

[93] D. S. Fisher, M. P. A. Fisher, and D. A. Huse, Phys. Rev. B **43**, 130 (1991).

[94] G. Blatter and V. B. Geshkenbein, in *Superconductivity*, edited by K.-H. Bennemann and J. B. Ketterson (Springer-Verlag Berlin Heidelberg, 2008) p. 496.

[95] R. Ikeda, T. Ohmi, and T. Tsuneto, J. Phys. Soc. Jpn. **59**, 1397 (1990).

[96] E. Brézin, D. R. Nelson, and A. Thiaville, Phys. Rev. B **31**, 7124 (1985).

[97] M. A. Moore, Phys. Rev. B **39**, 136 (1989).

[98] M. Iskin and C. A. R. Sá de Melo, Phys. Rev. Lett. **103**, 165301 (2009).

[99] E. Z. Kuchinskii, N. A. Kuleeva, and M. V. Sadovskii, J. Exp. Theor. Phys. **125**, 1127 (2017).

[100] R. Ikeda, T. Ohmi, and T. Tsuneto, J. Phys. Soc. Jpn. **59**, 1740 (1990).

[101] R. Ikeda, T. Ohmi, and T. Tsuneto, J. Phys. Soc. Jpn. **61**, 254 (1992).

[102] G. Eilenberger, Phys. Rev. **164**, 628 (1967).

[103] Z. Tešanović, Phys. Rev. B **44**, 12635 (1991).

[104] Z. Tešanović, Phys. Rev. B **59**, 6449 (1999).

[105] H. Fukuyama, H. Ebisawa, and T. Tsuzuki, Prog. Theor. Phys. **46**, 1028 (1971).

[106] A. G. Aronov, S. Hikami, and A. I. Larkin, Phys. Rev. B **51**, 3880 (1995).

[107] P. O. Sprau, A. Kostin, A. Kreisel, A. E. Böhmer, V. Taufour, P. C. Canfield, S. Mukherjee, P. J. Hirschfeld, B. M. Andersen, and J. C. S. Davis, Science **357**, 75 (2017).

[108] D. R. Nelson and V. M. Vinokur, Phys. Rev. B **48**, 13060 (1993).

[109] R. Ikeda, J. Phys. Soc. Jpn. **69**, 559 (2000).

[110] R. Ikeda, J. Phys. Soc. Jpn. **72**, 2930 (2003).

[111] V. M. Loktev, R. M. Quick, and S. G. Sharapov, Phys. Rep. **349**, 1 (2001).

[112] A. V. Chubukov, I. Eremin, and D. V. Efremov, Phys. Rev. B **93**, 174516 (2016).

[113] G. Bighin and L. Salasnich, Phys. Rev. B **93**, 014519 (2016).

[114] G. Bighin and L. Salasnich, Sci. Rep. **7**, 45702 (2017).

[115] B. C. Mulkerin, L. He, P. Dyke, C. J. Vale, X.-J. Liu, and H. Hu, Phys. Rev. A **96**, 053608 (2017).

[116] M. Matsumoto, R. Hanai, D. Inotani, and Y. Ohashi, J. Phys. Soc. Jpn. **87**, 014301 (2018).

[117] P. E. Kornilovitch and J. P. Hague, J. Phys. Condens. Matter **27**, 075602 (2015).

[118] U. Toniolo, B. C. Mulkerin, C. J. Vale, X.-J. Liu, and H. Hu, Phys. Rev. A **96**, 041604(R) (2017).

[119] U. Toniolo, B. C. Mulkerin, X.-J. Liu, and H. Hu, Phys. Rev. A **97**, 063622 (2018).

[120] E. J. Mueller, Rep. Prog. Phys. **80**, 104401 (2017).

[121] S. Jensen, C. N. Gilbreth, and Y. Alhassid, arXiv:1807.03913.

[122] S. Schmitt-Rink, C. M. Varma, and A. E. Ruckenstein, Phys. Rev. Lett. **63**, 445 (1989).

[123] L. Zheng, Y. Sakai, X. Miao, S. Nishiyama, T. Terao, R. Eguchi, H. Goto, and Y. Kubozono, Phys. Rev. B **94**, 174505 (2016).

[124] X. Miao, T. Terao, X. Yang, S. Nishiyama, T. Miyazaki, H. Goto, Y. Iwasa, and Y. Kubozono, Phys. Rev. B **96**, 014502 (2017).

Acknowledgment

I would like to thank Prof. Ryusuke Ikeda for his support during my master's and doctoral programs. I am deeply grateful to him for providing me many opportunities to discuss condensed matter physics and giving me many pieces of helpful advice in carrying out studies. Without his guidance, I could not have done this work.

I would like to thank Prof. Norio Kawakami, Prof. Youichi Yanase, Prof. Robert Peters, and Prof. Masaki Tezuka in Condensed Matter Theory Group for their support as well as fruitful discussions. I am grateful to Prof. Yuji Matsuda, Prof. Kenji Ishida, Prof. Takasada Shibauchi, Prof. Shik Shin, Prof. Kozo Okazaki, Prof. Shigeru Kasahara, and Prof. Yuta Mizukami for stimulating discussions on experimental aspects of condensed matter physics. I also have greatly benefited from my colleagues in Condensed Matter Theory Group for everyday discussions on physics and other topics.